



# **Dipole Photonic Resonators and Analogues of Matter**

**Abiola Oluponmile Oladipo**

**Supervised by : Professor Rebecca Seviour**

Thesis submitted in fulfilment of the requirements for the degree  
of Doctor of Philosophy

Physics Department, Lancaster University

January 2012

# Abstract

High power RF deflecting cavities have found a wide range of applications which include particle separation, emittance exchange, X-ray pulse compression, temporal beam diagnostics, and crab crossing in colliders. However, conventional deflecting cavities suffer from beam degrading parasitic modes that are also confined within these cavities. Several mode damping/coupling schemes have been developed to solve this problem but they add to the cost, size, and complexity of the resonant cavities. Photonic Crystal (PC) accelerators and klystrons have benefited from the high mode selectivity of PCs where a specific EM state are confined to a defect in the PC while all other states are forced to propagate away. This work presents a systematic approach to designing a PC that confines only the  $TM_{110}$ -like dipole Bloch state and forces the propagation of all other EM states. This dipole PC resonator was tuned and optimized for crabbing application at 11.9942 GHz (operational frequency of the crab cavity at CLIC).

Also in this thesis, a carefully designed experimental measurement of the transmission spectrum of microwaves in a photonic crystal was used to demonstrate a well pronounced exhibition of the Dirac point in photonic analogues of graphene. This work adds to previous literature by studying the sensitivity of the Dirac point to the incident and receiving angles of waves propagating away from the  $\Gamma - K$  direction at the input and output boundaries of the PC respectively. In addition, the challenges associated with the experimental retrieval of the dispersion plot of a photonic crystal were pointed out.

# Acknowledgment

I am heartily grateful to my supervisor, Professor Rebecca Seviour, for her insightful comments, excellent support and hard work on supervising my research in the past four years.

For intellectual discussions and support, my heartfelt thanks to Yiming Xu, Dr Yap soon Tan, Dr Graeme Burt, Dr Chris Lingwood and the entire staff of the workshop in the Physics Department of Lancaster University.

I acknowledge with gratitude the financial support from the EPSRC and the Cockcroft Institute.

Many thanks to my friends Jing Wen, Bayo Ojo, and Babatunde Kassim for their care and support.

I am deeply indebted to my parents, without whom this would not have been possible.

Above all, I thank God for his steadfast love, kindness and mercy towards me.

# Declaration

The work presented in this thesis is to the best of my knowledge and belief original, except as acknowledged in the text.

The thesis has not been submitted for the award of a higher degree elsewhere.

Signed by:

Abiola Oluponmile Oladipo

20 January 2012

# Contents

<b>1</b>	<b>Introduction</b>	<b>1</b>
1.1	Motivation for this work . . . . .	2
1.2	Resonant cavities in Accelerator and Wakefields . . .	8
1.3	Advances in high power dipole resonating cavities . .	10
1.4	Photonic band gap structures . . . . .	12
1.5	Advances in photonic band gap research . . . . .	15
1.6	Graphene . . . . .	20
1.7	Outline of this thesis . . . . .	22
<b>2</b>	<b>Theory</b>	<b>24</b>
2.1	Introduction . . . . .	24
2.2	An eigenvalue problem . . . . .	24
2.3	Properties of PBG structures . . . . .	28
2.4	Dispersion calculations in PBG structures . . . . .	32
2.4.1	The 2D Plane Wave Expansion (PWE) method	34
2.4.2	Finite Difference Time Domain (FDTD) method	35
2.4.3	Finite Element Method (FEM) . . . . .	39

2.4.4	Particle-In-Cell (PIC) Method . . . . .	43
2.5	The origin of the band gaps . . . . .	45
<b>3</b>	<b>Wave dispersion and dipole Bloch state confinement in photonic crystals</b>	<b>49</b>
3.1	Introduction . . . . .	49
3.2	Dynamic of the global band gap with varying permit- tivity and filling factor . . . . .	52
3.3	Dynamic of confined EM states in single and double point defects . . . . .	53
3.4	Dynamic of confined EM states with variation in the radius of innermost rods closest to the double defect .	66
3.5	Quality factor improvement for confined Bloch states	68
<b>4</b>	<b>Dipole PC Crab Cavity</b>	<b>72</b>
4.1	Introduction . . . . .	72
4.2	A PBG crab cavity . . . . .	76
4.2.1	Frequency scaling of the 2D lattice design . .	77
4.2.2	Finite height scaling of the lattice design . . .	78
4.2.3	Suppression of long range Wakefields by PBG crab cavity . . . . .	80
4.2.4	Analytical calculation of short range Wakefield in PBG crab cavity . . . . .	83
4.2.5	Convergence analysis of the HFSS simulation of a PBG crab cavity . . . . .	87
4.2.6	Optimization of the PBG crab cavity . . . . .	88

4.2.7	Final single-cell Design Parameters . . . . .	96
4.3	Coupling of EM power into a PC crab cavity . . . . .	98
4.3.1	Coupling of EM power from a coaxial wire . . . . .	99
4.3.2	Coupling of EM power from a waveguide . . . . .	101
4.4	High Power application of Final Design Parameters . . . . .	107
4.4.1	A single-cell PBG crab cavity for CLIC . . . . .	107
4.4.2	A multi-cell PBG crab cavity for CLIC . . . . .	111
4.4.3	Power requirement for the PBG crab cavity design . . . . .	118
4.4.4	Damping the power of the parasitic modes . . . . .	121
4.5	A cooling system for the PBG crab cavity . . . . .	123
4.6	A fabrication approach for the PBG crab cavity . . . . .	128
4.6.1	The dielectric rods . . . . .	129
4.6.2	The metallic plates . . . . .	130
4.6.3	The assemblage of the PBG crab cavity . . . . .	131
<b>5</b>	<b>Dirac Point in Photonic Analogues of Graphene</b>	<b>135</b>
5.1	Introduction . . . . .	135
5.2	Theoretical background of Dirac point in Photonic crystals . . . . .	137
5.3	The Experimental Setup . . . . .	142
5.4	Experimental results for a hexagonal lattice of cylin- drical rods . . . . .	144
5.5	Experimental results for a hexagonal lattice of spheres	150
<b>6</b>	<b>Conclusion and looking forward</b>	<b>155</b>

<b>A</b>	<b>Hermitian operators and their properties</b>	<b>163</b>
<b>B</b>	<b>Wakefields and the Panofsky-Wenzel theorem</b>	<b>166</b>
B.1	Introduction . . . . .	166
B.2	Longitudinal wake function and loss factor . . . . .	167
B.3	Transverse wake function and loss factor . . . . .	170
B.4	The Panofsky-Wenzel theorem . . . . .	172
<b>C</b>	<b>Experimental measurement of the dispersion of a PC lattice</b>	<b>173</b>
C.1	Theoretical retrieval of the propagation constant . . .	174
C.2	The calibration result . . . . .	177
<b>D</b>	<b>The calibration procedure</b>	<b>181</b>

# Abbreviations

- PC:- Photonic Crystal
- PBG:- Photonic Band Gap
- EM:- Electromagnetic
- TM:- Transverse Magnetic
- TE:- Transverse Electric
- RF:- Radio Frequency
- DOS:- Density Of State
- LDOS:- Local Density Of State
- LED:- Light Emmiting Diode
- LOM:- Lower Order Mode
- SOM:- Same Order Mode
- HOM:- Higher Order Mode
- FEL:- Free Electron Laser

- CLIC:- Compact Linear Collider
- SLAC:- Stanford Linear Collider
- ILC:- International Linear Collider
- LHC:- Large Hadron Collider
- PWE:- Plane Wave Expansion
- FDTD:- Finite Difference Time Domain
- FEM:- Finite Element Method
- SiC:- Silicon Carbide
- SiO:- Silicon Oxide
- Q:- Quality factor
- CAD:- Computer Aided Drawing
- CNC:- Computer Numeric Control
- MOST:- Multi-variable optimizer and Scanning Tool
- FDM:- Finite Difference Method
- MEEP:- MIT Electromagnetic Equation Propagation
- PML:- Perfectly Matched Layer
- FFT:- Fast Fourier Transform
- PDE:- Partial Differential Equation
- PIC:- Particle In Cell

- FSP:- Finite Size Particle
- NGP:- Nearest Grid Point
- IP:- Interaction Point
- HFSS:- High Frequency Structure Simulator
- DC:- Direct Current
- OFHC:- Oxygen Free High Conductivity
- VNA:- Vector Network Analyzer

# Chapter 1

## Introduction

The quest for technological advancement has led to a remarkable mastery of material science and engineering. Naturally occurring materials have been modified to develop artificial materials (like metamaterials) with desirable properties. A great deal of success has been achieved in understanding the mechanical, electrical and optical properties of materials. This is evident from the tremendous progress made in metallurgy, ceramics, plastics, superconductors, semiconductors and fiber optics just to mention a few. The ability of artificial photonic crystal materials to control Electromagnetic (EM) waves has been likened to the way semiconductors control the flow of electrons. Therefore, a huge fraction of research into controlling the flow of EM waves has been channeled toward developing photonic circuits which might one day replace our state of the art electronic circuits. The telecommunication industry is already benefiting from fiber optics technology, which act as an optical transmission line and offers higher bandwidth to distance ratio than traditional wired

lines. Other area like antenna design, laser technology, high-speed computing, and spectroscopy among others are waiting in line to benefit from similar optical technology.

## 1.1 Motivation for this work

The usefulness of cavity resonators has been recognized for a long time [1, 2]. They have been employed in both low and high power applications. In [3, 4], low power cavities have been used to make photo transceivers, LEDs, and laser detectors. High power resonating cavities are used for particle acceleration, RF generation and amplification [5, 6, 7]. Particle accelerators are, and will be important for their application in, but not limited to the following fields [8, 9]:

- Medicine, for the diagnosis and treatment of cancer [10, 11].
- As an intense source of X-rays for the sterilization of medical equipment and food products [12].
- For mineral and oil prospecting [13].
- As a source of particle beams for material sciences analysis [14].
- For radioisotope production [15].
- Cargo screening [16].
- Defense applications [17, 18].
- Accelerator driven sub-critical reactors [19, 20].

- For processing of semiconductor chips, ceramics, insulators, metals and plastics [21, 22].
- For radiocarbon dating [23].
- For probing the ultimate constituents of matter and the origin of the universe [24, 25].

Cavity resonators are used in particle accelerators to give longitudinal and transverse kicks to particle bunches. In this thesis, Transverse Magnetic (TM) modes have their electric field parallel to the axis of the particle bunch while the electric field of the Transverse Electric (TE) modes are perpendicular to the particle bunch axis. Most cavities used in particle accelerators are designed to utilize the  $TM_{010}$  monopole mode (shown in figure 1.1) with radially symmetrical, nodeless electric field distribution. According to the Lorentz force equation [26], particles travelling through the resonator will experience a longitudinal force in the direction of the electric field which causes the velocity and energy of the particles to increase. On the other hand, many particle accelerators involve the collision of two particle bunches. This type of accelerators are called colliders. During the collision of the particles, head-on collisions are ideally preferred. However, due to the finite crossing angle (introduced to simplify the dumping of spent particle bunches) in circular colliders, the collisions are not head-on and luminosity is reduced. The *luminosity* of a collider can be defined as the ratio of the event (collisions) rate  $R$  to the interaction cross-sectional area  $\sigma_{int}$  [27]. For a head-on

collision of two particle bunches with  $n_1$  and  $n_2$  particles and each with repetition frequency  $f$ , the luminosity  $L$  measured in  $\text{cm}^{-2}\text{s}^{-1}$  is given as:

$$L = \frac{R}{\sigma_{int}} = f \frac{n_1 n_2}{4\pi\sigma_x\sigma_y} \quad (1.1)$$

Where the  $\sigma_x$  and  $\sigma_y$  are the beam length in the x and y direction respectively. Luminosity is a key figure of merit that indicates how well particle bunches collide in the collider facilities. The effect of the finite crossing angle  $\theta_c$  on the luminosity of a circular collider is expressed by a luminosity reduction factor  $S$  which is given as [28]:

$$S = \frac{1}{\sqrt{1 + \left(\frac{\sigma_z\theta_c}{2\sigma_x}\right)^2}} \quad (1.2)$$

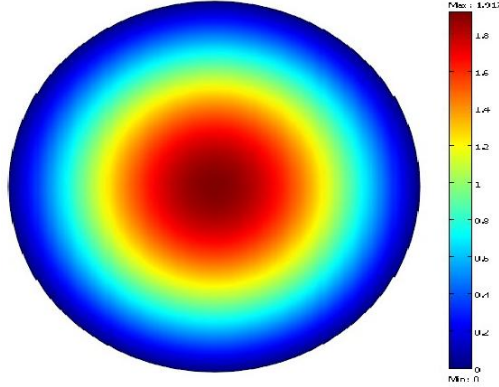


Figure 1.1: The electric field distribution of a monopole mode of a pillbox resonator with radius  $r = 0.015\text{m}$  and frequency  $f = 7.65\text{ GHz}$ .

As suggested in [29] and illustrated in figure 1.2, a rotation of a particle bunch before impact will cause a near-head-on collision which improves the luminosity of the collider [30, 31]. Most conventional resonating cavities used for rotating particle bunches employ

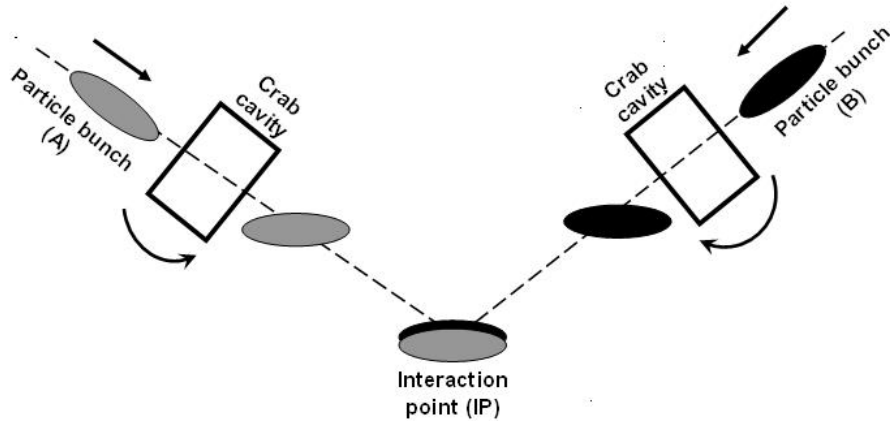


Figure 1.2: An illustration of a crab crossing scheme showing the rotation of bunches before collision at the interaction point.

a time-varying  $TM_{110}$  dipole mode [32]. The head and the bottom of the particle bunch receive kicks in opposite directions causing the bunch to rotate by an angle proportional to the mean transverse voltage. While conventional cavity resonators (pillboxes) are able to confine the dipole mode of interest, they also sustain parasitic Lower Order Modes (LOM), Same Order Modes (SOM), and Higher Order Modes (HOM) within the cavity [33]. These parasitic modes are capable of knocking particle bunches off axis and cause the bunches to break up. In order to reduce this bunch degrading effect in conventional deflecting cavities, specialized mode damping schemes are employed [34, 35]. Damping schemes increase the cost, size and complexity of the cavity resonator.

On the other hand, Photonic Crystals (PC) have the ability to forbid the propagation of waves with certain wavelengths while allowing other wavelengths to propagate. When a defect is introduced into the crystal, electromagnetic waves of specific frequencies can be con-

fined within the defect region. This selective mode confining ability of PCs has found application in PC accelerators [36, 37, 38, 39, 40] and klystrons [41, 42] where mode damping schemes are not required. The parasitic modes in this case propagate away from the defect and through the crystal lattice to the surrounding of the PC. So far, beam deflecting and bunch rotating (crabbing) cavities have never been designed using PCs. After a discussion of relevant theories in chapter 2, chapter 3 discusses the design of a photonic lattice that confines only the  $TM_{110}$ -like dipole EM state while forcing all other EM states to propagate away. In chapter 4, this lattice has been used to design an 11.9942 GHz crabbing resonator that can be used in the Compact Linear Collider (CLIC) facility.

The dispersion properties of photonic crystals have been likened to those of semiconductors [43]. Periodic potentials within the structures of semiconductors are capable of preventing the directional transport of electrons with certain energies [44] due to the presence of energy gaps in its electronic dispersion relation. Electrons with energies outside the gap are allowed to travel through the semiconductor material. Photonic crystals are optical analogues of naturally occurring crystals and have been shown to exhibit similar behaviours [45]. One naturally occurring crystal lattice that has recently caught the attention of a lot of researchers is graphene. Graphene is a single layer two dimensional (2D) honeycomb lattice of carbon atoms. One of the sources of interest in graphene is its linear electronic dispersion

that exhibits a conical singularity usually called the Dirac point at the corners (K-point) of the first order Brillouin zone. As the Dirac point is approached, the electronic Density of State (DOS) drops linearly [46]. This linear dispersion is expected to allow for better control of electronic transport in graphene. However, due to the atomic length scale of graphene, experimental observation of theoretically predicted effects and industrial applicability becomes a challenge as current engineering technologies are unable to sculpt material at such small length scales. On the other hand, the dispersion of EM waves in 2D photonic crystals have been shown theoretically [47] and experimentally [48, 49] to exhibit similar conically singularity to those found in graphene. Unlike graphene, photonic crystals can be fabricated at macroscopic (millimeters) length scale using modern fabrication techniques. This allow for macroscopic scale investigation of many quantum mechanical phenomenon in artificial photonic crystals. In chapter 5, an improved experimental approach (than those presented in the two previously published papers [48, 49]) for the investigation of the Dirac point in photonic crystals is presented, and the dependency of the Dirac point on variations in the Bloch wave vectors are also shown.

## 1.2 Resonant cavities in Accelerator and Wake-fields

Standing wave resonant cavities are important parts of modern particle accelerators for their role in beam-wave energy transfer. A standing (stationary) wave can result from the interference of two waves with the same frequency and amplitude but traveling in opposite direction. A standing wave resonant cavity can be created by causing EM waves to travel in between two reflectors, where the waves are reflected back and forth and thereby creating an interference pattern. Waves with wavelengths that are multiple of the distance between the reflectors will experience constructive interference and form a standing wave with reinforced amplitudes. These waves are resonant modes of the cavity created by the reflecting walls. Microwave resonators are hollow metallic structures that are able to confine stationary waves in the microwave region of the EM spectrum. A good example is the pillbox cavity shown in figure 1.3.

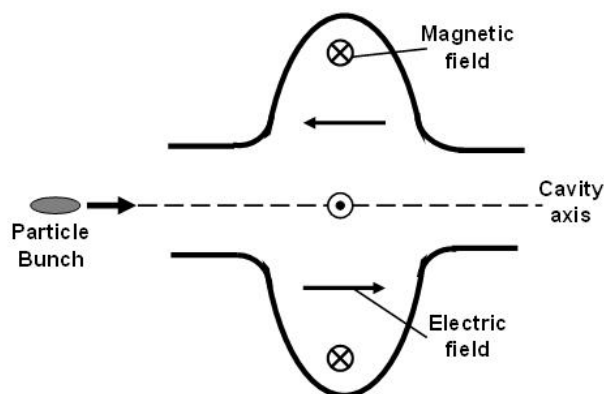


Figure 1.3: An illustration of a pillbox cavity showing a confined dipole mode.

The interaction of particle bunches with confined EM waves in a resonant cavity is governed by the Newton-Lorentz force where for a particle with charge ( $q$ ) travelling with velocity ( $v$ ) in electric ( $E$ ) and magnetic ( $B$ ) fields will experience a force ( $F$ ) expressed in equation 1.3.

$$\vec{F} = q(\vec{E} + \vec{v} \times \vec{B}) \quad (1.3)$$

Resonant cavities can be used to either give a longitudinal kick and/or a transverse kick to particle bunches. In order to give longitudinal kick to the particle bunch, the  $TM_{010}$  monopole mode can be used, where the peak electric field coincides with the axis and points in the longitudinal direction of the particle bunch. When the electric field of a monopole mode is at maximum amplitude, the magnetic field goes to zero and only the first term of the right hand side (RHS) of equation 1.3 is useful for longitudinal kick.

$$\vec{F}_z = q\vec{E}_z \quad (1.4)$$

On the other hand, when a transverse kick is required, a  $TM_{110}$  dipole mode can be used, where the peak magnetic field coincides with the particle bunch trajectory but points in a direction perpendicular to the velocity of the particle bunch. In this case, the electric field at the node point of the dipole mode is ideally equal to zero and only the second term of the RHS of the Lorentz force equation 1.3 is used for transverse kick. The transverse force experienced by

the particle bunch points in a direction perpendicular to both the longitudinal trajectory of the particle bunch and the direction of the magnetic field.

$$\vec{F}_y = q(\vec{v}_z \times \vec{B}_x) \quad (1.5)$$

When an ultra-relativistic particle bunch travels through a symmetric cavity, electric current is induced to flow on the walls of the cavity. This current in turn induces secondary electromagnetic fields into the cavity. These secondary EM fields are called Wakefields (further detail in Appendix B). Wakefields can couple to the allowed resonant modes of the cavity and extract energy from trailing particles travelling at a distance behind the first particle bunch. Wakefields are capable of knocking the particle bunch off axis and can cause the bunch to break up [50, 51].

### **1.3 Advances in high power dipole resonating cavities**

Some of the earliest uses of transverse deflecting cavities were in particle separators [52, 53, 54]. They can be used to sort a particle bunch into its constituent species (such as protons and kaons) based on their different masses. Also particle separators are used to split a bunch into smaller parts and redirect the bunch parts to different experiment.

In [52, 53], normal conducting dipole deflecting cavities were used for particle separation at the Stanford Linear Accelerator (SLAC) in the 1960's. Emittance exchange is another application of deflecting cavities where the longitudinal emittance of a particle bunch can be converted to a transverse emittance and vice versa [55, 56]. Emittance exchange is done by using the time varying dipole mode to accelerate or decelerate the constituent particles of a bunch based on their transverse position away from the axis.

In [57, 58, 59], emittance exchange has been shown to improve the performance of Free Electron Lasers (FEL). A considerable amount of advanced scientific research now requires X-ray sources with pulses shorter than 1 ps, which cannot be provided by conventional X-ray sources that provide pulses up to 100 ps [60]. A pulse compression scheme was proposed in [55], and have been studied in [61] where two standing wave deflecting cavities are used to give a longitudinally dependent transverse kick to particle bunches. The resulting vertical motion of the constituent particles of the bunch causes the bunch to be *chirped* and allows for the spatial separation of radiation from different parts of the bunch. The radiation from the particle bunch can be either sliced or combined with time-compressing X-ray optics to obtain a beam with 1 ps pulse duration. Furthermore, the temporal structure of beams with ever shorter pulse duration requires a beam diagnostic that employs a dipole deflecting cavity [62, 63]. The bunch duration is calculated from the transverse offset of the

particle bunch due to the rotation caused by the deflecting cavity. The resolution of the bunch structure is dependent on its width and the transverse voltage [64]. A beam diagnostics scheme with temporal resolution in the femtoseconds range has been designed for the UCLA Neptune Beam Line [65].

Crab crossing of particle bunches have been used in the electron-positron collider (KEK-B) [30, 31], the International Linear Collider (ILC) design [66], the Large Hadron Collider (LHC) design [67], and the Compact Linear Collider (CLIC) design [68, 69] to improve luminosity. Both normal and superconducting dipole deflecting cavities have been used to rotate (crabbing) the particle bunch in order to obtain a near-head-on collision of the bunches. A record luminosity (a measure of the collision dose administered) of  $4.49 \times 10^{33} \text{ cm}^{-2}\text{s}^{-1}$  was achieved by the superconducting crabbing scheme of KEK-B.

Although more work is still in progress to improve the performance of conventional deflecting cavities, the complexity introduced by parasitic mode damping remains a major issue.

## 1.4 Photonic band gap structures

Photonic band gap (PBG) structures can be described as a periodic array of varying permittivity  $\varepsilon$  that is capable of controlling the propagation of EM waves. PBG structures can be made from metals, dielectric or both as a 1, 2 or 3 dimensional structure as shown in figure 1.4. The propagation of EM waves in PBG structures is

governed by the Bloch-Floquet theorem [70, 71]. This is discussed in detail in chapter 2.

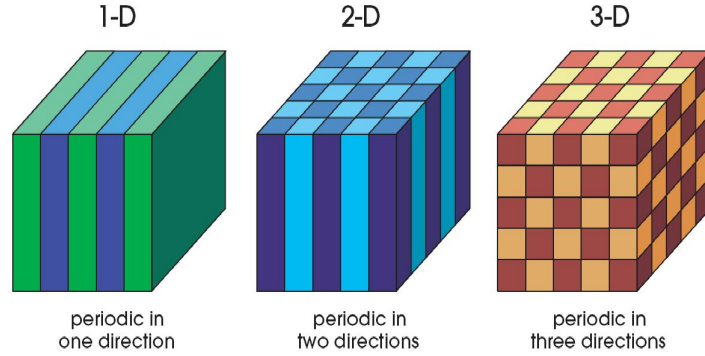


Figure 1.4: Structural periodicity can be in 1, 2, or 3 dimensions. Picture was taken from Ref [43].

PBG structures have the ability to forbid the propagation of waves with certain range of frequencies while allowing the propagation of waves with other frequencies. These forbidden wavelengths are called *band gaps* while the allowed wavelengths form the propagation bands. A PBG structure can offer a band gap for certain wave vectors  $k$  while allowing the propagation of waves with other  $k$ -vectors. When a band gap exists for all possible  $k$ -vectors in the plane of periodicity, then the PBG structure is said to possess a global photonic band gap. PBG structure can easily be created by arranging the scatterers into a square or a triangular lattice as shown in figure 1.5.

Other photonic lattice designs include the honeycomb lattice, and the kagome lattice. In the honeycomb lattice the hexagons formed by the positioning of the scatterers are connected along the edges

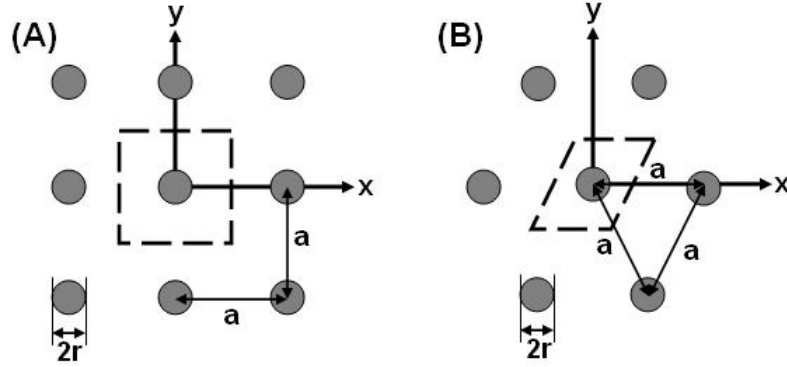


Figure 1.5: The unit cell of a 2D (a) square lattice and (b) triangular lattice is the area within the dashed lines.  $a$  and  $r$  are the lattice constant and the radius of the scatterers respectively. Picture was taken from Ref [72].

while the hexagons in the kagome lattice are connected at the corners thus creating a triangle at the centre of three hexagons. Due to the periodic nature of the lattices and the Bloch-Floquet condition [70, 71], the properties of the entire lattice can be investigated by analyzing a unit cell of the lattice [43]. The unit cell of the square and triangular lattice is shown in figure 1.5. When a defect is introduced into the periodic lattice by removing a single scatterer at the centre (shown in figure 1.6), EM states with specific frequency within the band gap can be confined to the defect region of the lattice [73].

The frequency of the trapped Bloch state in figure 1.6 is determined by the lattice constant  $a$ , the radius of the scatterers  $r$  and the permittivity  $\varepsilon$  of the materials that make up the PBG structure. These parameters can be tuned to control the propagation of EM waves in PBG structures.

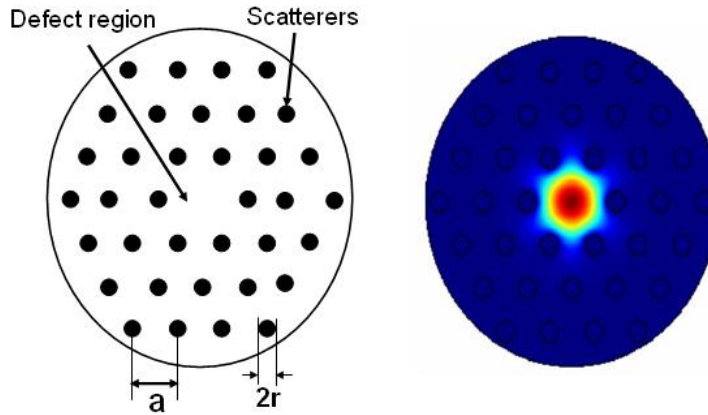


Figure 1.6: Schematic diagram of a photonic band gap structure with triangular lattice. The centre scatterer is removed to create a defect and the eigenmode is shown on the right.

## 1.5 Advances in photonic band gap research

Lord Rayleigh studied for the first time in 1892 the propagation of electromagnetic wave into a 1D periodic structure [74] and for more than 70 years, quarter-wavelength plates or multiple layered dielectric mirrors such as those used for high-Q-value laser cavities have been use in optics. However, concerning the control of electromagnetic waves (light), the above examples are 1D photonic crystals and are only useful for restricted applications. In contrast, two 2D- and three 3D- dimensional photonic crystals are better suitable for the control of electromagnetic waves. This was first pointed out in two separate papers published about the same time in 1987 by Yablonovitch [75] and John [76].

Yablonovitch showed by simulation the existence of a PBG, where all modes were missing in all directions and consequently, the spontaneous emission corresponding to the gap energy is inhibited inside a 3D photonic crystal [77]. The most common lattice designs are the

square and the triangular lattices. Photonic band gap made of dielectric [43, 78], metals [36, 72, 79] and both [80] have been studied in the past. In [81], interesting properties of metallic PBG structures for microwave applications was shown both numerically and experimentally by demonstrating the mode confining ability of PBG structure. At the beginning, most of the metallic PBG structures investigated were designed with square lattices [82]. The disadvantages of using square lattices were pointed out in [72]. Square lattices have quadruple symmetry which is less than the sextuple symmetry offered by triangular lattice. Also, with the analysis presented in [43], it can be seen that a complete photonic band gap cannot be obtained from PBG structure possessing a square lattice of isolated scatterers.

In [72], a comparison between the global band gap structure for square and triangular metallic lattice was made for both TE and TM modes. In the TM mode, both square and triangular global band gap structures show that the width of the band gap increases with the ratio  $r/a$  where  $r$  is the rod radius and  $a$  is the lattice constant. Both lattice type also exhibit a zeroth-order band gap which is similar to the cut-off band of a conventional waveguide. The threshold for the first-order band gaps in metallic PBG structures with square and triangular lattices are 0.1 and 0.2 respectively [72]. When the problem of Higher Order Mode (HOM) confinement is considered for metallic PBG structures, a metallic square lattice will require rods

with very small diameters in order to avoid there HOMs. Beyond the thresholds  $r/a = 0.1$ , a square lattice will begin to confine not just the fundamental modes but also the HOMs. A triangular lattice offers less constraints with regards to fabrication because it has a larger threshold of  $r/a = 0.2$  beyond which it will confine HOMs.

A good example of the application of a triangular lattice PBG structure is the design of a 17.14 GHz linear accelerator in [73]. Although a  $TM_{010}$ -like fundamental mode required for acceleration was obtained from this travelling wave PBG structure, the band gap is not a complete photonic band gap, because it is polarization dependent. In [43], a study showed that a PBG structure with isolated scatterers favours a band gap for TM modes while PBG structures with connected stripe scatterers favours a band gap for TE mode. In order to obtain a complete band gap, a structure that exhibits the properties of connected and isolated scatterers is required. A PBG structure with air holes in a dielectric slab was use to obtain the first ever 2D complete photonic band gap [43]. However, such a structure is not suitable for an accelerating cavity as particle bunches will collide with the background dielectric material.

A new hybrid PBG structure lattice design was presented in [80]. This hybrid structure used a hexagonal lattice of rods connected by slim rectangular stripes to form a periodic 2D structure. In [82], the effect of metallic inputs to a dielectric PBG structure was studied. The width of the complete band gap can be varied by changing the

diameter of the metallic rod input. The location of the metallic input was also shown to determine whether the complete band gap closes or opens up as the diameter of the metallic rod is increased.

In [83], a wide range of parameters affecting the width of photonic band gaps was investigated. The authors of [83] showed that the uncertainty in the numerical simulation of photonic crystals reduces as the number of reciprocal vector is increased. This means that an 11x11 lattice is better than a 7x7 lattice. PBG structures with generic unit cells were also shown to yield desirable properties. In fact, cavities with smaller inclination angles between these primitive vectors in reciprocal space will yield wider band gaps which are suitable for application that require spectral purity. Wider band gaps can also be obtained from PBG structures with larger refractive index ( $n$ ) contrast. When designing high power PBG structures with an array of metallic scatterers in air (refractive index  $n = 1$ ), the choice of a suitable material with high electrical conductivity as well as high refractive index contrast is important. Copper ( $n = 2.43$ ) seems to be the best metal when compared to other conductive metals like silver ( $n = 1.35$ ), aluminium ( $n = 1.39$ ) and gold ( $n = 0.47$ ). This agrees with the findings in [84] where the effect of ellipticity in the rod scatterers and refractive index contrast within the lattice was studied. As the filling factor which is a function of  $r/a$  increases, the width of the band gap increases. The filling factor is the fraction of the lattice volume occupied by the scatterers. The results in [83]

agrees with the analysis of the global band gap structures in [72]. However, it must be mentioned that there is an optimum value of filling factor for every case of refractive index contrast and inclination angle.

In [85], it was shown that metallic PBG structures can be about seven times smaller and lighter than a dielectric PBG structure. This characteristic of metallic PBG structure is favourable for reducing the size of particle accelerators. An interesting concept worth mentioning is the controllable photonic band gap structure [86]. In this case, active components (diodes) were used to control the capacitance and the inductance between the scattering elements thus controlling the band gap of the periodic structures.

There are several numerical methods for analysing PBG structures. These methods include the Plane Wave Expansion (PWE) method [87, 88], Finite Difference Time Domain (FDTD) method [89, 90], Finite Element Method (FEM) [91] amongst others. This numerical methods are discussed in chapter 2. The choice of numerical methods depends on the parameters of interest as well as the geometry of the PBG structures involved. When the parameter of interest is the dispersion plot of frequency against the k-vector, the PWE and FDTD are the most popular numerical methods used.

## 1.6 Graphene

Graphene is a single layer of carbon atoms arranged in a 2D honeycomb lattice. Graphene can be viewed as a sheet of benzene ring without the hydrogen atoms. Graphene has been studied since the middle of the 20th century [92, 93, 94, 95, 96], starting with the work of P.R. Wallace in 1947. Most of the early studies on graphene were used as a starting point for the study of graphite or purely for scientific interest because researchers did not believe graphene could exist in a free and stable state [97]. Long range order was shown to be broken due to thermal instabilities in 2D crystals [100, 101, 102, 103, 104, 105, 106]. In 2004, the ground breaking and successful fabrication of graphene on a Silicon Oxide (SiO) substrate by a group in Manchester University settled the controversy over the existence of graphene [98]. Furthermore, they fabricated suspended graphene where the SiO substrate was etched away leaving behind a stable 2D sheet of graphene with highly mobile charge carriers [99]. Suspended graphene was found not to be flat but had ripples with wavelength much larger than the distance between the carbon atoms. The lattice structure of graphene is a honeycomb lattice with two atoms in the unit cell and two non-equivalent K-points in its Brillouin zone as shown in figure 1.7. The atoms in the unit cell of graphene belong to separate sub-lattices A and B that are not related by the lattice vectors.

The energy dispersion of graphene exhibits a conical singularity

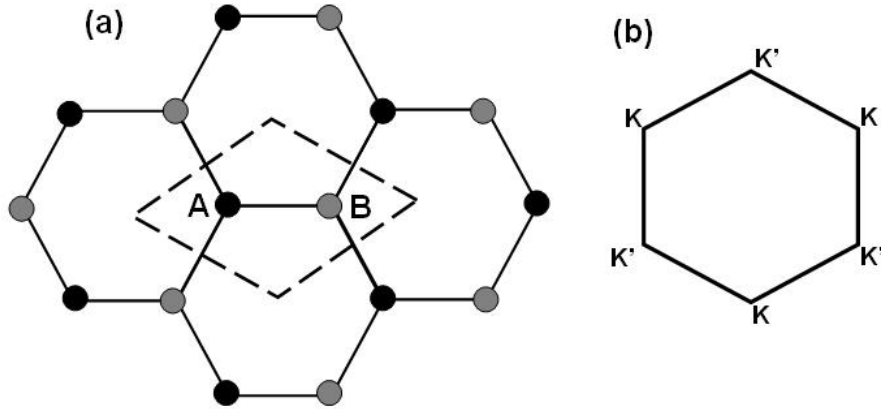


Figure 1.7: Schematic diagram of: (a) honeycomb lattice showing the two sublattices A and B with the unit cell marked by the dashed line. (b) The first Brillouin zone of a honeycomb lattice showing the two sets of non-equivalent K-points.

called the Dirac point at the corners of the first Brillouin zone. As the Dirac point is approached the energy of electrons depends linearly on the momentum vector. This peculiar energy dispersion has attracted a lot of interest in graphene since it was first fabricated [98]. Graphene exhibits several unusual properties such as mimicking the quantum electrodynamics of massless Dirac fermions [94, 96] and the anomalous integer quantum hall effect [107, 108, 109, 110]. Graphene also exhibits a minimal conductivity [111, 112, 113, 114, 115], the absence of Anderson localization [116, 117] and Klein tunnelling [118]. Furthermore, quantum gravity [119] and edge effects [114, 120] have been studied in graphene. Possible applications of graphene include the detection of single molecules [121], the measurement of the fine structure constant of materials [122], the storage of hydrogen [123] and the production of field effect devices [124, 125, 126]. It is widely accepted that the understanding of the properties of graphene can

open doors to a new frontier of science and technology.

## 1.7 Outline of this thesis

This thesis aims to design a dipole photonic resonator for high power application as well as to investigate the Dirac point in a photonic analogue of graphene. Following this introductory chapter, a preview of the remaining chapters is as follows:

- In chapter 2, a review of the background theories that governs the behaviour of electromagnetic waves in a photonic crystal lattice is presented. The numerical methods used for dispersion calculations in photonic crystal are also presented.
- In chapter 3, numerical results are discussed where the dynamics of the band gap with varying permittivity and filling factors was studied for a PC made of dielectric rods in air. Furthermore, the dynamics of the Bloch states confined in single and double point defects is presented. Also the effect of variation in the radius of the innermost rods around the double point defect on the confined states was studied. The effect of the number of rings of scatterers around the defect region on the quality factor (Q) of confined states is also presented.
- In chapter 4, results are presented using the lattice design in chapter 3 to design a dipole photonic resonator that is targeted for particle bunch crabbing application. The design frequency

is optimized to match the CLIC crab cavity that operates at 11.9942 GHz. An analytical calculation of parameters of merit of the dipole PBG cavity is also presented.

- In chapter 5, a review of theoretical studies on the Dirac point in photonic crystal is presented. Also presented is a discussion of the results of a experimental study of the Dirac point in photonic crystals. The sensitivity of the Dirac point to variations in the wave vector away from the K-point of symmetry in the Brillouin zone was investigated.
- In the final chapter, the contributions of this work to the knowledge base are pointed out and useful recommendations for future works are also made.

# Chapter 2

## Theory

### 2.1 Introduction

This chapter focuses on the unique properties of PBG structures that enhance their ability to generate band gaps. Starting with Maxwell's equations, an eigenvalue problem is formulated. Then, the geometry of PBG structures is described in terms of their symmetries. Furthermore, this chapter discusses the process of generating the dispersion band plot for PBG structures and explains the origin of the band gaps in the plot.

### 2.2 An eigenvalue problem

Named after James Clark Maxwell, a set of partial differential equations remain the bedrock for the macroscopic analysis of Electromagnetic (EM) wave propagation through any media. The set of equations relates the electric and magnetic fields to one another and to any source within the medium through which the EM wave

propagates. For the analysis presented here, the differential form of Maxwell's equation can be expressed as follows:

$$\nabla \cdot \vec{D} = \rho \quad (2.1)$$

$$\nabla \cdot \vec{B} = 0 \quad (2.2)$$

$$\nabla \times \vec{E} = -\frac{\partial \vec{B}}{\partial t} \quad (2.3)$$

$$\nabla \times \vec{H} = \vec{J} + \frac{\partial \vec{D}}{\partial t} \quad (2.4)$$

The vector fields  $\vec{E}$ ,  $\vec{H}$ ,  $\vec{D}$  and  $\vec{B}$  are the electric field and the magnetic field, the electric displacement and the magnetic flux density respectively.  $\vec{J}$  is the current density while  $\rho$  is the charge density. The relative permeability of non-magnetic materials have  $\mu_r \approx 1$  and in a source-free region  $\vec{J} = 0$  and  $\rho = 0$ . Also, the relationships  $\vec{B} = \mu\vec{H}$ ,  $\vec{D} = \varepsilon\vec{E}$ ,  $\mu = \mu_0\mu_r$  and  $\varepsilon = \varepsilon_0\varepsilon_r$  are important for this analysis where  $\mu_0$ ,  $\varepsilon_0$ , and  $\varepsilon_r$  are the free space permeability, the free space permittivity, and the relative permittivity respectively. The fields described by Maxwell's equation are harmonic functions of time and space. They can be expressed as follows:

$$\vec{E}(\vec{x}, t) = \vec{E}(\vec{x})e^{-i\omega t} \quad (2.5)$$

$$\vec{H}(\vec{x}, t) = \vec{H}(\vec{x})e^{-i\omega t} \quad (2.6)$$

Where  $\vec{E}(\vec{x})$  and  $\vec{H}(\vec{x})$  are the spatial distributions of the fields.  $\omega$  is the angular frequency and  $t$  is the time. The spatial distribution of the fields in the case of a plane wave can be expressed as follows:

$$\vec{E}(\vec{x}) = E_0 e^{\vec{k}\cdot\vec{x}} \quad (2.7)$$

$$\vec{H}(\vec{x}) = H_0 e^{\vec{k}\cdot\vec{x}} \quad (2.8)$$

where  $\vec{x} = x\hat{u}_x + y\hat{u}_y + z\hat{u}_z$  and  $k$  is the wave vector indicating the direction of the field.  $\hat{u}_x$ ,  $\hat{u}_y$ , and  $\hat{u}_z$  are the unit vectors along the x, y and z axes respectively. Using Maxwell's two divergence equations given in (2.1) and (2.2), the electric and magnetic fields can be shown to be transverse to each other and to the direction of propagation. This kind of EM wave is called a plane wave and the transverse nature of the fields is expressed in the equation 2.9 below.

$$H_0 \cdot \vec{k} = E_0 \cdot \vec{k} = 0 \quad (2.9)$$

Also, the two curl equations show the interdependency between the electric and the magnetic fields as follows:

$$\vec{E}(\vec{x}, t) = \frac{i}{\omega\epsilon} \nabla \times \vec{H}(\vec{x}, t) \quad (2.10)$$

$$\vec{H}(\vec{x}, t) = -\frac{i}{\omega\mu} \nabla \times \vec{E}(\vec{x}, t) \quad (2.11)$$

The relationship between the fields can be used to decouple Maxwell's equation into independent equations consisting of only one kind of vector field. This decoupled equations are usually referred to as the wave equation. For example, writing the wave equation in terms of the electric field is done by taking the curl of equation (2.3) and then substituting the curl of  $\vec{H}$  from equation (2.4) while using  $\vec{B} = \mu\vec{H}$ ,  $\vec{D} = \varepsilon\vec{E}$  and assuming free space conditions gives.

$$\nabla \times \frac{1}{\mu} \nabla \times \vec{E}(\vec{x}, t) = \omega^2 \varepsilon \vec{E}(\vec{x}, t) \quad (2.12)$$

Following the same procedure, by taking the curl of equation (2.4) and then substituting the curl of  $\vec{E}$  from equation (2.3) while assuming free space conditions, a purely magnetic field wave equation can be expressed as follows:

$$\nabla \times \frac{1}{\varepsilon} \nabla \times \vec{H}(\vec{x}, t) = \omega^2 \mu \vec{H}(\vec{x}, t) \quad (2.13)$$

When an operator  $\Psi$  acts on a vector field, say  $\vec{E}$  and the result is that same vector field multiplied by a constant, this equation can be described as an eigenvalue problem. A critical look at equations (2.12) and (2.13) shows that they are eigenvalue problems with the eigenoperators  $\nabla \times \frac{1}{\mu} \nabla \times$  and  $\nabla \times \frac{1}{\varepsilon} \nabla \times$  acting on eigenvectors  $\vec{E}(x, t)$  and  $\vec{H}(x, t)$  resulting in the same eigenvectors multiplied by

the eigenvalues  $\omega^2\varepsilon$  and  $\omega^2\mu$  respectively.

### 2.3 Properties of PBG structures

Photonic band gap structures are periodic structures that are generally made of either dielectrics or metal or both in 1, 2, or 3 dimensions. Their ability to create band gaps (a forbidden band of frequency where EM waves are not allowed to propagate) relates to their periodicity. This analysis is limited to the 2 dimensional (2D) type of PBG structure. The square and triangular lattices are the most widely used 2D lattice designs. 2D lattices usually have continuous translational symmetry along one axis (say in the direction of  $\vec{k}_z$ ) and discrete translational symmetry in the plane of periodicity ( $\vec{k}_\perp = \vec{k}_x + \vec{k}_y$ ). Along the axis with continuous translational symmetry, the properties of the PBG structure are invariant to any translation along that axis. Consider a small translation of distance  $d$  along the  $z$ -axis. The continuous translation can be described as:

$$\Xi_{d,z}\varepsilon(z) = \varepsilon(z - d) = \varepsilon(z) \quad (2.14)$$

$$\Xi_{d,z} \vec{E}_z e^{i\vec{k}_z \cdot z} = \vec{E}_z e^{-i\vec{k} \cdot (z-d)} = e^{i\vec{k} \cdot d} \vec{E}_z e^{i\vec{k}_z \cdot z} \quad (2.15)$$

The effect of the continuous translational operation result is the same vector field multiplied by an eigenvalue. On the other hand, the in-plane translation is discrete. In this case, the properties of the

PBG structure are invariant only at distances that are multiple of a fixed lattice constant  $a$ . The discrete translation of the dielectric constant in the periodic plane can be expressed as:

$$\varepsilon(\vec{x}_\perp + \vec{\tau}_{pq}) = \varepsilon(\vec{x}_\perp) \quad (2.16)$$

Where the periodic vector  $\tau_{pq}$  is dependent on the lattice type used.

$$\vec{\tau}_{pq} = \begin{cases} pa\hat{u}_x + qa\hat{u}_y, \text{ square lattice} \\ (p + \frac{q}{2})a\hat{u}_x + \frac{\sqrt{3}}{2}qa\hat{u}_y, \text{ triangular lattice} \end{cases} \quad (2.17)$$

$\vec{x}_\perp = x\hat{u}_x + y\hat{u}_y$  is the transverse coordinate,  $a$  is the lattice spacing,  $p$  and  $q$  are integers. A discrete translational operator  $D_{\vec{x}_\perp \vec{\tau}_{pq}}$  acting upon a vector field  $\vec{E}_\perp e^{i\vec{k}_\perp \cdot \vec{x}_\perp}$  in the plane of periodicity can be expressed as:

$$D_{\vec{x}_\perp \vec{\tau}_{pq}} \vec{E}_\perp e^{i\vec{k}_\perp \cdot \vec{x}_\perp} = \vec{E}_\perp e^{i\vec{k}_\perp \cdot (\vec{x}_\perp - \vec{\tau}_{pq})} = e^{-i\vec{k}_\perp \cdot \vec{\tau}_{pq}} \vec{E}_\perp e^{i\vec{k}_\perp \cdot \vec{x}_\perp} \quad (2.18)$$

The expression in equation (2.18) shows that the propagation of the vector field is invariant as it moves periodically within the transverse plane of the PBG structure. This is the Bloch-Floquet theorem [70, 71] which is valid for infinitely periodic lattices and a good approximation for finite physical lattices. As a result of the in-plane

discrete symmetry, the calculation of the field potential only needs to be performed within a single unit cell that is repeated throughout the lattice. The unit cell for the square and triangular lattice are defined as follows:

$$|x| \leq \frac{a}{2} \quad , \quad |y| \leq \frac{a}{2} \quad (\text{square lattice})$$

$$\left|x - \frac{y}{\sqrt{3}}\right| \leq \frac{a}{2} \quad , \quad |y| \leq \frac{\sqrt{3}a}{2} \quad (\text{triangular lattice})$$

In order to satisfy the discrete translational symmetry, the EM fields must have a phase shift  $\vec{k}_\perp \cdot \vec{\tau}_{pq} = 2\pi$  as it propagates between two lattice points separated by the periodic vector  $\vec{\tau}_{pq}$ . The set of vector  $\vec{k}$  that satisfy the condition  $e^{-i\vec{k}_\perp \cdot \vec{\tau}_{pq}}$  are referred to as the reciprocal vectors  $\vec{b} = \frac{2\pi}{a}$ . These vectors form a lattice of their own which is referred to as the reciprocal lattice. The primitive cell of the reciprocal lattice is called the Brillouin zone. This is a region in K-space that can be reached from the origin without crossing any Bragg planes. The Brillouin zone shown in figure 2.1 can be reduced by several symmetries that make up the point group of the reciprocal lattice. The symmetries include rotational symmetry, reflection symmetry and inversion symmetry. The reduced Brillouin zone is called the irreducible Brillouin zone.

As a result of all the symmetries within the lattice of the PBG structure, the in-plane wave vector  $\vec{k}_\perp$  can be limited to the irreducible Brillouin zone shown in figure 2.1. The three corners of the

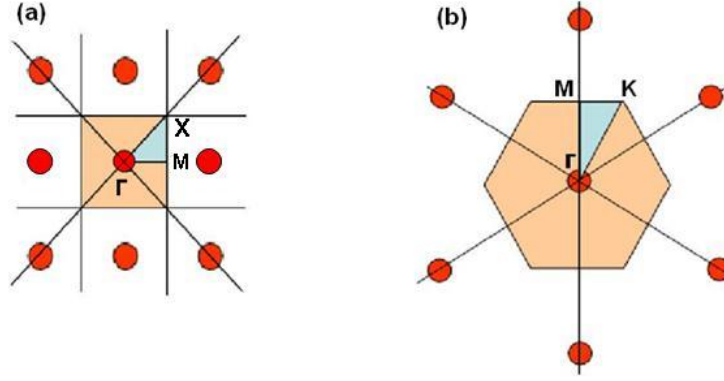


Figure 2.1: The reciprocal of (a) a square and (b) a triangular lattice showing the first Brillouin zone and the irreducible Brillouin zone.

irreducible Brillouin zone correspond to the values of the reciprocal wave vector  $\vec{k}_\perp$  from the origin as follows:

For square lattice:

$$\Gamma : \vec{k}_\perp = 0$$

$$M : \vec{k}_\perp = \left(\frac{\pi}{b}\right)\vec{e}_x$$

$$X : \vec{k}_\perp = \left(\frac{\pi}{b}\right)(\vec{e}_x + \vec{e}_y)$$

For triangular lattice:

$$\Gamma : \vec{k}_\perp = 0$$

$$M : \vec{k}_\perp = \left(\frac{2\pi}{\sqrt{3}b}\right)\vec{e}_y$$

$$K : \vec{k}_\perp = \left(\frac{2\pi}{3b}\right)(\vec{e}_x + \sqrt{3}\vec{e}_y)$$

The critical property of PBG structures which makes them attractive for many applications is the presence of the Band gap in their dispersion diagram (Band plot). This leads to three important

questions:

- How is the PBG dispersion diagram calculated and plotted?
- What is the origin of the band gap?
- What does the field distribution the Bloch states look like?

## 2.4 Dispersion calculations in PBG structures

In a 2D analysis of the PBG structure, the propagation of an EM wave can be separated into Transverse Electric (TE) modes and Transverse Magnetic (TM) modes. The definition of the TE and TM are sometimes used interchangeably depending on the perspective of the author. Here, the adopted definitions are as follows:

- Transverse Electric (TE):- Modes whose electric field is perpendicular to the scatterer axis of the PBG structure.
- Transverse Magnetic (TM):- Modes whose magnetic field is perpendicular to the scatterer axis of the PBG structure.

For metallic PBG structure, the above description of TE and TM imposes the following boundary condition on the surface of the conductors.

$$\vec{E}_s = 0 \quad (2.19)$$

$$\frac{\partial \vec{E}_s}{\partial n} = 0 \quad (2.20)$$

Where  $\frac{\partial}{\partial n}$  is the normal derivative at any point on the surface of the conductors.

Generally, the numerical methods used to obtain the dispersion characteristics of PBG structures can be divided into frequency domain methods and time domain methods. Although, both methods make use of EM sources within the domain to calculate the fields, the difference is in the parameter that is kept constant. In the frequency domain method, the numerical calculations proceed at a fixed frequency while in the time domain method, several modes with different frequencies can be calculated at any instance of time.

However, there is a numerical method that does not use the current source within the domain to calculate the fields. This method is called the frequency-domain eigenvalue method where the current function  $J(\vec{x}) = 0$ .

In this work, the three numerical techniques used are the Plane Wave Expansion (PWE) method [127] for dispersion calculations, the Finite Difference Time Domain (FDTD) method [128] for eigenfrequency analysis and the Finite Element Method (FEM) [129] to compute the field distribution with the photonic lattice. This numerical techniques are discussed in the following subsections.

### 2.4.1 The 2D Plane Wave Expansion (PWE) method

The decoupled Maxwell's equation is the starting point for the dispersion plot of PBG structures. In the PWE technique, Maxwell's equation is solved as an eigenvalue problem using equation 2.12 from section 2.2. Both the permittivity  $\varepsilon_r$  and the field function  $\vec{U}_{\vec{k}_\perp}$  are periodic, they can be Fourier expanded into an infinite number of simple sine and cosine functions.

$$\frac{1}{\varepsilon_r} = \sum_p \sum_q C_{p,q}^{\varepsilon_r} e^{-i\vec{G}_{p,q} \cdot \vec{x}_\perp} \quad (2.21)$$

$$\vec{U}_{\vec{k}_\perp}(\vec{x}) = \sum_m \sum_n C_{m,n}^{\vec{U}_{\vec{k}_\perp}} e^{-i\vec{G}_{m,n} \cdot \vec{x}_\perp} \quad (2.22)$$

Where  $\vec{k}_\perp = k_x + k_y$  is the wave vector of the field and  $\vec{x}_\perp = x\hat{u}_x + y\hat{u}_y$  is the transverse vector.  $\vec{G}_{p,q}$  is the primitive vector of the reciprocal lattice.

$$\vec{G}_{p,q} = \begin{cases} \frac{2\pi}{a}p\hat{u}_x + \frac{2\pi}{a}q\hat{u}_y, & \text{square lattice} \\ (\frac{2\pi}{a}\hat{u}_x - \frac{2\pi}{\sqrt{3}a}\hat{u}_y)p + \frac{4\pi}{\sqrt{3}a}\hat{u}_yq, & \text{triangular lattice} \end{cases} \quad (2.23)$$

Equation 2.21 and 2.22 are substituted into equation 2.12 and integrated over the area  $A$  of the unit cell shown in figure 1.5, we obtain:

$$\sum_p \sum_q C_{m-p,n-q}^{\varepsilon_r} (\vec{k}_\perp + \vec{G}_{m,n})^2 C_{m,n}^{\vec{U}_{\vec{k}_\perp}} = \frac{\omega^2}{c^2} C_{m,n}^{\vec{U}_{\vec{k}_\perp}} \quad (2.24)$$

$$C_{p,q}^{\varepsilon_r} = \frac{1}{A} \int_A \frac{1}{\varepsilon_r} e^{i\vec{G}_{p,q} \cdot \vec{x}_\perp} \partial A \quad (2.25)$$

$$\overline{M} = \left[ \sum_p \sum_q C_{m-p,n-q}^{\varepsilon_r} (\vec{k}_\perp + \vec{G}_{m,n})^2 \right] \quad (2.26)$$

$$\overline{M} \begin{bmatrix} C_{m,n}^{\vec{U}_{\vec{k}_x}} \\ C_{m,n}^{\vec{U}_{\vec{k}_y}} \end{bmatrix} = \frac{\omega^2}{c^2} \begin{bmatrix} C_{m,n}^{\vec{U}_{\vec{k}_x}} \\ C_{m,n}^{\vec{U}_{\vec{k}_y}} \end{bmatrix} \quad (2.27)$$

This is a matrix eigenvalue equation and the matrix  $\overline{M}$  can be diagonalized using a matrix manipulation software like MATLAB [130] to calculate the eigenvectors  $C_{m,n}^{\vec{U}_{\vec{k}}}$  and the eigenvalues  $\omega$ . There is an infinite number of solutions to equation 2.27 due to the infinite number of terms in the Fourier series. However for computational implementation, the Fourier series has to be truncated at a reasonable resolution for a smooth representation of the periodic functions. This is the plane wave expansion numerical technique.

#### 2.4.2 Finite Difference Time Domain (FDTD) method

The Finite Difference Time Domain (FDTD) technique is a widely used numerical method where the Finite Difference Method (FDM) is solved in the time domain. In the FDM [133], differential equations are converted into difference equations that can be solved using

simple algebra. A detailed description of the FDTD method can be found in [128].

In the 2D FDTD numerical computation, the Maxwell's curl equation for TM modes can be written as :

$$\frac{\partial \vec{H}_x}{\partial t} = -\frac{1}{\mu_0} \frac{\partial \vec{E}_z}{\partial y} \quad (2.28)$$

$$\frac{\partial \vec{H}_y}{\partial t} = \frac{1}{\mu_0} \frac{\partial \vec{E}_z}{\partial x} \quad (2.29)$$

$$\varepsilon_r \varepsilon_0 \frac{\partial \vec{E}_z}{\partial t} = \frac{\partial \vec{H}_y}{\partial x} - \frac{\partial \vec{H}_x}{\partial y} - \vec{J}_z \quad (2.30)$$

Applying the FDM, the derivatives in the above equation can be approximated by the finite differences in the state of the EM fields with respect to space and time. In order to explain the FDM, consider the state of a system  $f(x)$  with respect to the position (x) of observation. For a small finite and constant change (p) in the position, the derivative  $f'(x)$  can be approximated from the Taylor's series using the central finite difference approximation.

$$D_0 f(x) = \frac{f(x+p) - f(x-p)}{2p} = f'(x) + \frac{p^2}{6} f'''(\xi) \quad (2.31)$$

The term of the far right-hand side of equations 2.31 is the leading order truncation errors from the Taylor's series. The error in the central finite difference approximation is proportional to the square

of the step (p) in space and this makes it a second order approximation. The central finite difference second-order approximation described above was employed in [134] for the discretization of the FDTD simulation domain using the Yee lattice (shown in figure 2.2 on page 37) and the Yee algorithm.

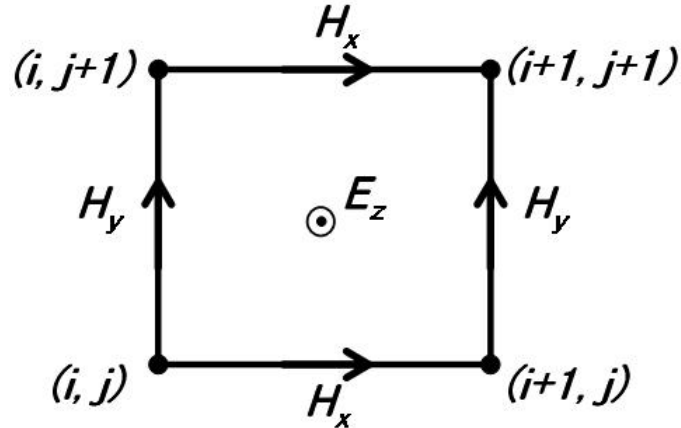


Figure 2.2: 2D Yee lattice used in the FDTD TM calculation.

Figure 2.2 shows a single grid block of a 2D Yee mesh where the distance  $\Delta x$  between the points  $(i, j)$  and  $(i + 1, j)$  is the grid size along the x-axis. Similarly, the distance  $\Delta y$  between the points  $(i, j)$  and  $(i, j + 1)$  is the grid size along the y-axis.  $i$  and  $j$  are integers indicating the number of grid blocks along the x and y axis respectively. According to the Yee algorithm the electric and magnetic fields component calculations are staggered in time and space. As shown in figure 2.2 (for the TM case), the electric field component is surrounded by four circulating magnetic fields while the magnetic field components are flanked by two electric field components. This means that the  $E_z$ ,  $H_x$  and  $H_y$  field components are calculated and stored at points  $((i + \frac{1}{2})\Delta x, (j + \frac{1}{2})\Delta y)$ ,  $((i + \frac{1}{2})\Delta x, j\Delta y)$  and  $(i\Delta x, (j + \frac{1}{2})\Delta y)$

respectively. A *leap-frog* time stepping approach was adopted in the Yee algorithm where for a time step  $\Delta t$  the magnetic field at time  $t$  is calculated from the stored value of the magnetic field at time  $(t - \Delta t)$  and the electric field at time  $(t - \frac{1}{2}\Delta t)$ . In a similar manner, the electric field at time  $(t + \frac{1}{2}\Delta t)$  is calculated from the stored value of the magnetic field at time  $t$  and the electric field at time  $(t - \frac{1}{2}\Delta t)$ .

The central difference second order approximation of equation 2.31 can be applied to the Maxwell's curl equations 2.28, 2.29, and 2.30 to obtain the finite difference approximation given in equations 2.32, 2.33 and 2.34 below. To do this, a field function  $\phi$  at a discrete point  $(i\Delta x, j\Delta y)$  in the Yee lattice and at a discrete time  $n\Delta t$  is represented as  $\phi(i\Delta x, j\Delta y, n\Delta t) = \phi|_{i,j}^n$  and  $\mu_0 = 1.256637 \times 10^{-6} \text{ Hm}^{-1}$  is the free space permeability.  $n$  is an integer indicating the number of time steps.

$$\frac{\vec{H}_x|_{i,j}^{n+1} - \vec{H}_x|_{i,j}^n}{\Delta t} = -\frac{1}{\mu_0} \frac{\vec{E}_z|_{i,j+\frac{1}{2}}^{n+\frac{1}{2}} - \vec{E}_z|_{i,j-\frac{1}{2}}^{n+\frac{1}{2}}}{\Delta y} \quad (2.32)$$

$$\frac{\vec{H}_y|_{i,j}^{n+1} - \vec{H}_y|_{i,j}^n}{\Delta t} = \frac{1}{\mu_0} \frac{\vec{E}_z|_{i+\frac{1}{2},j}^{n+\frac{1}{2}} - \vec{E}_z|_{i-\frac{1}{2},j}^{n+\frac{1}{2}}}{\Delta x} \quad (2.33)$$

$$\varepsilon_r \varepsilon_0 \frac{\vec{E}_z|_{i,j}^{n+\frac{1}{2}} - \vec{E}_z|_{i,j}^{n-\frac{1}{2}}}{\Delta t} = \frac{\vec{H}_y|_{i+\frac{1}{2},j}^n - \vec{H}_y|_{i-\frac{1}{2},j}^n}{\Delta x} - \frac{\vec{H}_x|_{i,j+\frac{1}{2}}^n - \vec{H}_x|_{i,j-\frac{1}{2}}^n}{\Delta y} - \vec{J}_z|_{i,j}^n \quad (2.34)$$

In equations 2.32 and 2.33, the magnetic field at time  $(n + 1)\Delta t$  is calculated from the magnetic field at time  $n\Delta t$  and the electric

field at time  $(n + \frac{1}{2})\Delta t$ . Also in equation 2.34 , the electric field at time  $(n + \frac{1}{2})\Delta t$  is calculated from the current source and magnetic fields at  $n\Delta t$  as well as the electric field at  $(n - \frac{1}{2})\Delta t$  . The Maxwell's divergence equations are implicitly enforced by the Yee discretization as shown in [90] where the wave propagation is dissipation free.

### 2.4.3 Finite Element Method (FEM)

The finite element method [141, 142] is a numerical approach where approximate solutions to a partial differential equation (PDE) that describes physical systems are found by discretizing the problem domain into a finite number of irregular elements (polygons). The PDE are solved individually in each element, the solutions are assembled together to form a global matrix equation which is solved to find the unknown parameters.

A *weak* form of the wave equation is obtained by multiplying both sides by a test function  $T_{\perp}$  and integrating over the domain of the problem subject to appropriate boundary condition.

$$\int_A [T_{\perp} \nabla^2 \vec{E}_{\perp}(x, t) - k_0^2 \epsilon_r(x) \vec{E}_{\perp}(x, t) T_{\perp}] \partial A = 0 \quad (2.35)$$

Following the FEM approach the simulation domain is discretized into large number of small elements that are connected to form a computational mesh. For a 2D simulation, the elements have a planar geometry with no variation along the z-axis. Since most polygons can be divided into a number of triangles, therefore, the simplest

element geometry is the first-order triangular finite element (first-order tetrahedral element in 3D case).

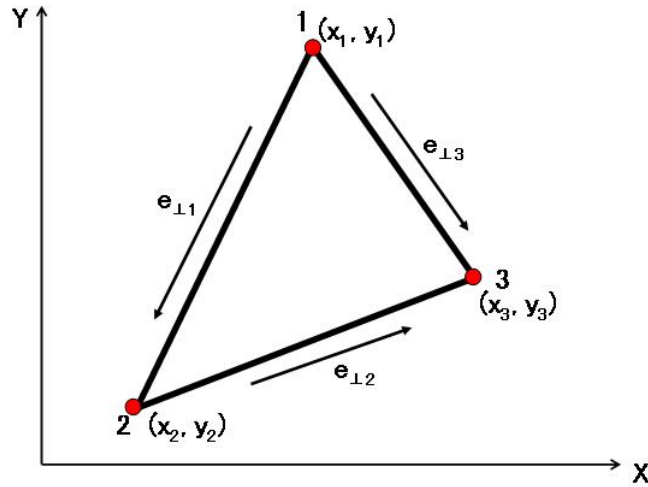


Figure 2.3: A first order triangular finite element.

The shapes of the triangular elements shown in figure 2.3, can be varied to conform to the boundary curvature. Also the size of the element are chosen so that the material (permittivity) and the electric fields within each element is uniform (not changing). A variable resolution mesh can be implemented so that greater number of smaller elements are used in regions of the problem domain where large variations in the fields are expected and fewer and bigger elements are used in regions with gradual changes in the fields. Once the domain has been discretized into a fine mesh, equation 2.35 has to be solved in each individual element. Depending on the type of problem to be solved, the elementary solutions are found by either the nodal-based Lagrangian interpolation approach [144] or the vector-based tangential edge elements approach [145, 146] or both.

The nodal-based finite element approach is not suitable for the ap-

proximation of the vector field in an electromagnetic simulation especially at the elementary boundary where only the tangential component of the vector field is allowed. The nodal-based FEM approach does not impose Maxwell's divergence equation which causes it to return spurious non-physical modes [148, 149]. On the other hand, a recently developed edge element FEM approach allows only the tangential component of the vector fields at the elementary boundary and enforces Maxwell's divergence equation. This allows physical constraints and natural boundary conditions to be properly implemented. In the edge element approach, the tangential component of the vector field along a single edge of the triangular element is kept constant while simultaneously the tangential field component on the other two edges are set to zero. Therefore, the electric field within each triangular element is determined by the three functions of the edge tangential field.

$$\vec{E}_\perp = \sum_{i=1}^3 e_{\perp m} W_{\perp m} \quad (2.36)$$

Where  $W_{\perp m} = L_{\perp m}(\alpha_i \nabla_\perp \alpha_i - \alpha_j \nabla_\perp \alpha_j)$ .  $m$  indicates the three edges of the triangular element,  $L_{\perp m}$  is the length of each edge  $m$  linking nodes  $i$  and  $j$ .  $\alpha_i$  and  $\alpha_j$  are the geometric function associated with the node points.  $e_{\perp m}$  are the coefficient of the edge basis function  $W_{\perp m}$ . In [149], it was shown that  $\nabla \cdot W_{\perp m} = 0$  hence the electric field does not diverge across the elementary edge boundaries ( $\nabla \cdot E = 0$ ). Here the test function is defined as  $T_\perp = W_{\perp n}$  and

$n = 1, 2, 3$ . Equation 2.36 is substituted into the electromagnetic variational equation given as:

$$\int_A \frac{1}{\mu_r} (\nabla_{\perp} \times \vec{T}_{\perp}) \cdot (\nabla_{\perp} \times \vec{E}_{\perp}) \partial A = k_0^2 \varepsilon_r \int_A \vec{T}_{\perp} \cdot \vec{E}_{\perp} \partial A \quad (2.37)$$

$$\frac{1}{\mu_r} \int_A \sum_{i=1}^3 (\nabla_{\perp} \times W_{\perp n}) \cdot (\nabla_{\perp} \times W_{\perp m}) e_{\perp m} \partial A = k_0^2 \varepsilon_r \int_A \sum_{i=1}^3 (W_{\perp n} \cdot W_{\perp m}) e_{\perp m} \partial A \quad (2.38)$$

Equation 2.38 can be written in the general FEM matrix eigen-equation form as:

$$[S_{el}][e_{\perp}] = k_0^2 [T_{el}][e_{\perp}] \quad (2.39)$$

$$[S_{el}] = \left[ \frac{1}{\mu_r} \int_A (\nabla_{\perp} \times W_{\perp n}) \cdot (\nabla_{\perp} \times W_{\perp m}) \partial A \right] \quad (2.40)$$

$$[T_{el}] = \left[ \varepsilon_r \int_A (W_{\perp n} \cdot W_{\perp m}) \partial A \right] \quad (2.41)$$

The element matrices are assembled to obtain a global eigen-matrix equation.

$$[S][e_{\perp}] = k_0^2 [T][e_{\perp}] \quad (2.42)$$

At the Perfectly Electric Conducting (PEC) boundaries, FEM simply set the field  $E = 0$  at the nodes and edges of element that

coincide with the boundary. FEM techniques have been shown in [143] to give results that compare excellently with analytical results. FEM are able to handle problems with complex geometry better than the FDTD techniques hence their wide use in engineering. On the down side, the results of the FEM technique is only an approximation of physical systems as the fields within each element are assumed to be polynomials which is not physically true.

#### **2.4.4 Particle-In-Cell (PIC) Method**

The Particle-In-Cell (PIC) method is a versatile numerical technique that solves a set of partial differential equations that describes the trajectory of individual particles within plasmas (ionized particles). The PIC method also calculates the field associated with the motion of individual particles as well as the collective effects of particle-particle interactions.

The PIC method is a well established technique that has started as far back as 1955 [151] before the computer age. Detailed description of the PIC method can be found in several books and publications [152, 153, 154]. The PIC method has found application in a wide range of scientific research areas which include space and weather science, accelerator science, RF generation, plasma physics, and research involving complex chemical reactions etc.

The approach used in the PIC method involves a continuous loop of updates that begins by tracking the position and the velocity of the particles based on the electric and magnetic fields they experi-

ence. Based on the new position and velocity of the particles, the electromagnetic fields generated by the particles are used to calculate the field seen by the particles in the next loop cycle. This looping approach is illustrated in figure 2.4. The implementation of the fundamental PIC approach varies from one author to another. In this subsection, the PIC implementation detailed (by J.M. Dawson) in [152] where the Fast Fourier Transform (FFT) was employed to calculate the field parameter in k-space is presented.

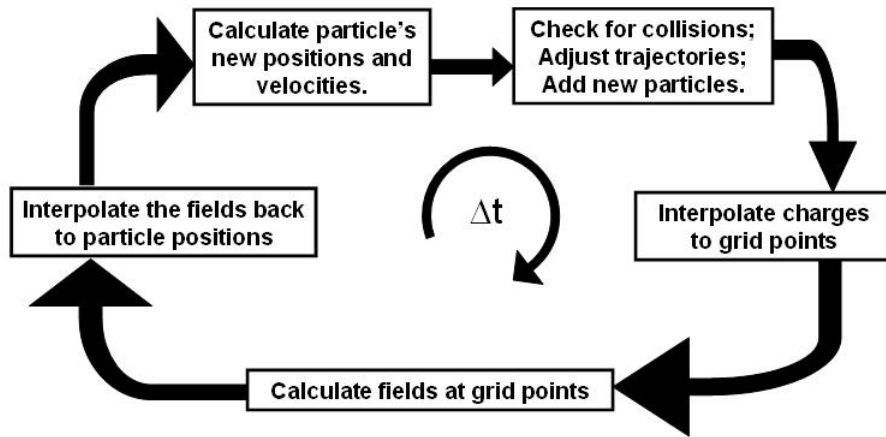


Figure 2.4: An illustration of the particle-in-cell approach.

The number of particle in a natural plasma are of the order of  $10^{12}$  particles / $\text{cm}^3$  [152]. Enormous computer resource will be required to track the position and velocity of individual particles since the number of arithmetic operation  $\eta$  is proportional to the square of the particle population  $N$ .

$$\eta = 10N^2 \tag{2.43}$$

In order to minimize the number of arithmetic operations, the

PIC method uses a single superparticle to represent a user defined number of natural plasma particles. This reduction in the number of particles to track in turn leads to a shorter runtime of the PIC code.

In this work, the Vorpahl PIC simulation code [155] is used to perform a Wakefield analysis of a PBG crab cavity, this is discussed in chapter 4. A Fast Fourier Transform (FFT) of the time signal of the EM field recorded by a monitor placed at a specific grid point in the simulation domain gives the frequency domain distribution of the power spectrum at that grid point.

## 2.5 The origin of the band gaps

In section 2.4.1, a discussion on how PBG structures are characterized using their dispersion diagram (band plots) was presented. The band plot shows the modes (indicated by their frequency) that are allowed to propagate in any particular direction (indicated by the wave vector  $k$ ) within the PBG structure. As we move along the points of symmetry of the irreducible Brillouin zone (for a square lattice;  $\Gamma \rightarrow M \rightarrow X \rightarrow \Gamma$ ), a set of allowed modes can occupy a frequency range referred to as a band. Most dispersion plots of PBG structure have several bands of allowed modes. On the other hand, for each direction of the wave vector  $k$ , it is possible to have a frequency range where no propagating mode is allowed. This frequency range is called a gap. When the lowest frequency of a upper band is higher than the highest frequency of a lower band, then we have a

global band gap. In a 2D analysis of PBG structures, the TM and TE dispersion characteristics can be completely different. When the band gap of both TM and TE states overlap, we have a complete global band gap that is independent of both the direction of propagation and the polarization of the incident EM wave.

The origin of the band gap stems from the different locations of EM energy storage within a photonic crystal [43]. EM states belonging to the same band tend to concentrate their energy in the same type of material (i.e the dielectric or the air regions). This can be explained by looking at the electromagnetic variational theorem that shows the effect of a small variation in a parameter on the solution of an electromagnetic problem [156]. This analysis starts with the decoupled Maxwell's equations (2.12) and (2.13). If we multiply equation (2.12) by  $\vec{E}$  and equation (2.13) by  $\vec{H}$  and then integrate over the volume  $V$  of the PBG structure, we obtain:

$$\int_V \vec{E} \cdot (\nabla \times \frac{1}{\mu} \nabla \times \vec{E}) dV = \int_V \omega^2 \epsilon \vec{E} \cdot \vec{E} dV \quad (2.44)$$

$$\int_V \vec{H} \cdot (\nabla \times \frac{1}{\epsilon} \nabla \times \vec{H}) dV = \int_V \omega^2 \mu \vec{H} \cdot \vec{H} dV \quad (2.45)$$

From the definition of the inner product, equation (2.44) and (2.45) can be expressed as follows:

$$[\vec{E}, \Xi \vec{E}] = \omega^2 \epsilon [\vec{E}, \vec{E}] \quad (2.46)$$

$$[\vec{H}, \Xi \vec{H}] = \omega^2 \mu [\vec{H}, \vec{H}] \quad (2.47)$$

Where the Hermitian operator  $\Xi$  is given as:

$$\Xi = \begin{cases} \nabla \times \frac{1}{\mu} \nabla \times, & \text{Electric field eigenoperator} \\ \nabla \times \frac{1}{\varepsilon} \nabla \times, & \text{Magnetic field eigenoperator} \end{cases}$$

$$\text{and } \omega^2 = \frac{[\vec{E}, \Xi \vec{E}]}{[\vec{E}, \varepsilon \vec{E}]} = R_E \quad (2.48)$$

$$\text{and } \omega^2 = \frac{[\vec{H}, \Xi \vec{H}]}{[\vec{H}, \mu \vec{H}]} = R_H \quad (2.49)$$

Where  $R_E$  and  $R_H$  are Rayleigh quotients. Rearranging equation (2.44), the Rayleigh quotient of the electric field equation can be expressed as :

$$R_E = \omega^2 = \frac{\int_V \vec{E} \cdot (\nabla \times \frac{1}{\mu} \nabla \times \vec{E}) dV}{\int_V \varepsilon \vec{E} \cdot \vec{E} dV} = \frac{\int_V \frac{1}{\mu} (\nabla \times \vec{E})^2 dV}{\int_V \varepsilon \vec{E}^2 dV} \quad (2.50)$$

The eigenmode with the lowest frequency  $\omega_0$  must minimize the Rayleigh quotient. This means that errors in the approximation of the eigenvector  $\vec{E}$  do not have a significant effect on the eigenvalue  $\omega^2$ . Therefore, we can say  $\frac{d\omega^2}{d\vec{E}} = 0$ .

Taking a critical look at equation (2.50), the square of the eigenvector  $\vec{E}^2$  is present in both the numerator and the denominator.

This means that the eigenvalue  $\omega^2$  is independent of the field potential. Also a larger dielectric constant and a lower spatial oscillation are both required to minimize the eigenvalue in equation (2.50). Therefore, we can say that the lowest frequency  $\omega_0$  mode concentrates its electric field energy in regions of high dielectric constant [43]. This means that the energy of the modes belonging to the lowest band of the dispersion plot are concentrated in the rods (for a lattice of rods in air). From the previous section, it was shown that any two harmonic modes with different frequencies must be orthogonal to each other. Therefore, the modes of the upper bands must be orthogonal to those of the lowest band. The second lowest band consists of the lowest frequency modes amongst the set of orthogonal modes to those of the lowest band. The orthogonality rule is more dominant than the storage of energy in regions of high dielectric constant. This means that higher order modes can store their energy in regions of low dielectric constant in order to maintain orthogonality with lower order modes. The variation in the storage location of the field energy, inherently leads to variation in the value of the dielectric constant  $\varepsilon$  in equation (2.50) and will result in eigenfrequency variations. The frequency variations or jumps create a frequency band where no harmonic mode can propagate. This is the origin of the band gap. Also, the higher the variation in the dielectric constant from the rod regions to the air regions, the higher the frequency jump from equation (2.50), which results in wider band gaps [43].

# Chapter 3

## Wave dispersion and dipole Bloch state confinement in photonic crystals

### 3.1 Introduction

Since the pioneering work of Yablonovich [75], and John [76] into the ability of photonic crystals to control the flow of light, a variety of passive and active devices have been constructed by introducing defects into photonic crystals. Utilizing the band-gap of the crystals these defects act as high Quality-factor, mode selective resonators, where only EM fields with specific frequencies are confined, predominately by Bragg and internal reflection [43]. This selective confinement of EM waves has found applications both in low and high power applications, and offers a number of advantages over conventional technologies [157, 158, 159, 160, 36, 41]. One such area of applications that is gaining increased interest, is the application of

photonic crystals to high power applications in particle accelerators [36, 37, 38, 39, 40] and EM wave generation [41, 42]. One key issue for conventional technology used in particle accelerators to confine EM waves are the parasitic mode effects which limit the performance of the technology.

A more specific accelerator application which suffers strongly from the effects of Higher Order Modes (HOM) confinement are Crab Cavities [161]. Conventional crabbing cavities employ the time-varying magnetic field of a dipole mode to give upward/downward kicks to the front/back of a particle bunch respectively, thereby causing the particle bunch to be rotated by an angle proportional to the maximum magnetic field in the resonator [29, 68, 162]. In addition to the dipole mode, conventional crabbing resonators also confine these parasitic modes which are capable of knocking particle bunches off axis and break them up [50, 51]. These parasitic modes are usually suppressed with specialized mode damping schemes which increase the size, cost and complexity of the resonator [34, 35], and fundamentally limit the operating range of the conventional approach. Photonic crystals with their high mode selectivity can confine a specific mode while allowing these other parasitic modes to propagate away through the lattice. In this chapter, the ability of a PC resonator to confine just the dipole mode, whilst forcing all other mode to propagate away through the lattice was explored and the lattice for a dipole photonic resonator was designed.

To date, research both experimental and theoretical, has mainly focused on monopole, quadrupole and sextupole photonic resonators [163, 164]. In contrast little research has considered the dipole mode, due in part to the comparatively low Quality factor of the dipole mode. Although the dipole mode does offers several advantages as pointed out in [165], such as smaller modal volume and novel field distribution [163]. This chapter focuses on dipole mode confinement in single and double point defect resonators, studying how varying the lattice parameters around the defect region defines the states confined in the defect region, and how the lattice parameters affect the Quality factor for a specific mode of the resonator. The geometry considered in this work is a 2-Dimensional (2D) triangular lattice of dielectric rods with permittivity  $\varepsilon$ , separation  $a$  and radius  $r$ , as shown in figure 3.1. In this work, lattice defects are used to form the resonators, this is achieved by modifying the radius, the permittivity and the removal of a scatterer.

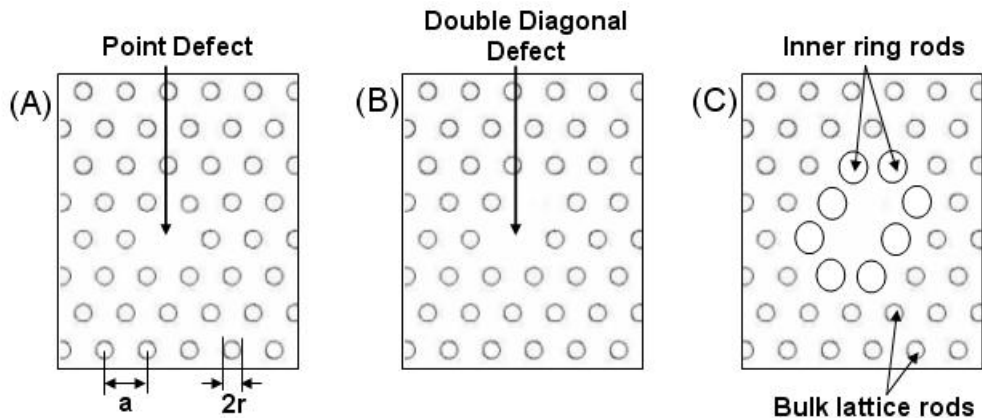


Figure 3.1: 2D triangular lattice of dielectric scatterers of radius  $r$  and separation  $a$ . Defect regions was created by the (A) removal of a single scatterer; (B) removal of the two scatterers; (C) removal of the two scatterers and varying the radius of scatterers around the double defect.

Due to the complexity of the structures studied we use a combination of numerical techniques to determine the band structure and the confined EM field distribution. Dispersion curves are determined using a Plane Wave Expansion (PWE) technique [127]. The confined states in the defect are determined using Finite Difference Time Domain (FDTD) [128] and the Finite Element Method (FEM) [129] numerical techniques.

### **3.2 Dynamic of the global band gap with varying permittivity and filling factor**

Previous research has focused on maximizing the global band gap in photonic crystals [83], where the effects of refractive index contrast, filling factor ( $r/a$ ) and different lattices on the size of the band gap were considered. The authors of [166] found that changes in the refractive index contrast and the filling factor of the structure could create/destroy band gaps. In this thesis, we extend the work of [83] and [166] by investigate the frequency dependent position of the global band gaps on the lattice parameters. To determine the position of the global band gaps, the PWE technique discussed in the chapter 2 was used to determine  $\vec{k}$  of all propagating states. A multi-parameter scan was performed by varying the relative permittivity ( $\epsilon_r = 3$  to 65) of the scatterers of the lattice, whilst sweeping the filling factor ( $r/a$ ) from 0.05 to 0.45 in steps of 0.01. Figures 3.2, 3.3, 3.4, 3.5, 3.6, 3.7, and 3.8 show the results of this parameter sweep for

both Transverse Magnetic (TM) and Transverse Electric (TE) fields. The shaded region in each graph show the frequency/permittivity where a band gap exists. For the work presented here, the magnetic field of the TM states and the electric field of the TE states are perpendicular to the translational invariant direction of the 2D PBG structure (i.e the scatterers). We see from figures 3.2, 3.3, 3.4, 3.5, 3.6, 3.7, and 3.8 that the size of any particular band gap increases with permittivity and decreases with increasing values of the ratio  $r/a$ . As  $r/a$  is increased, higher order band gaps are created, and for a specific  $r/a$  the number of band gaps increases with increasing permittivity.

### **3.3 Dynamic of confined EM states in single and double point defects**

The second part of the analysis determined the frequency and electric field distribution of states confined to the defect region using the FEM. Figures 3.9, 3.10, and 3.11 represent lattices with a single point defect, of the form shown in figure 3.1(A), for  $r/a = 0.1, 0.2$  and  $0.3$  respectively. Each figure shows the frequency position of the bandgap and the frequency of the modes confined. In figure 3.9, only monopole-like Bloch states are confined in the gap. The higher order band gaps are small, and extensive eigenfrequency analysis found no confined states present in these other band-gaps.

From figures 3.10 and 3.11 only monopole-like states are confined

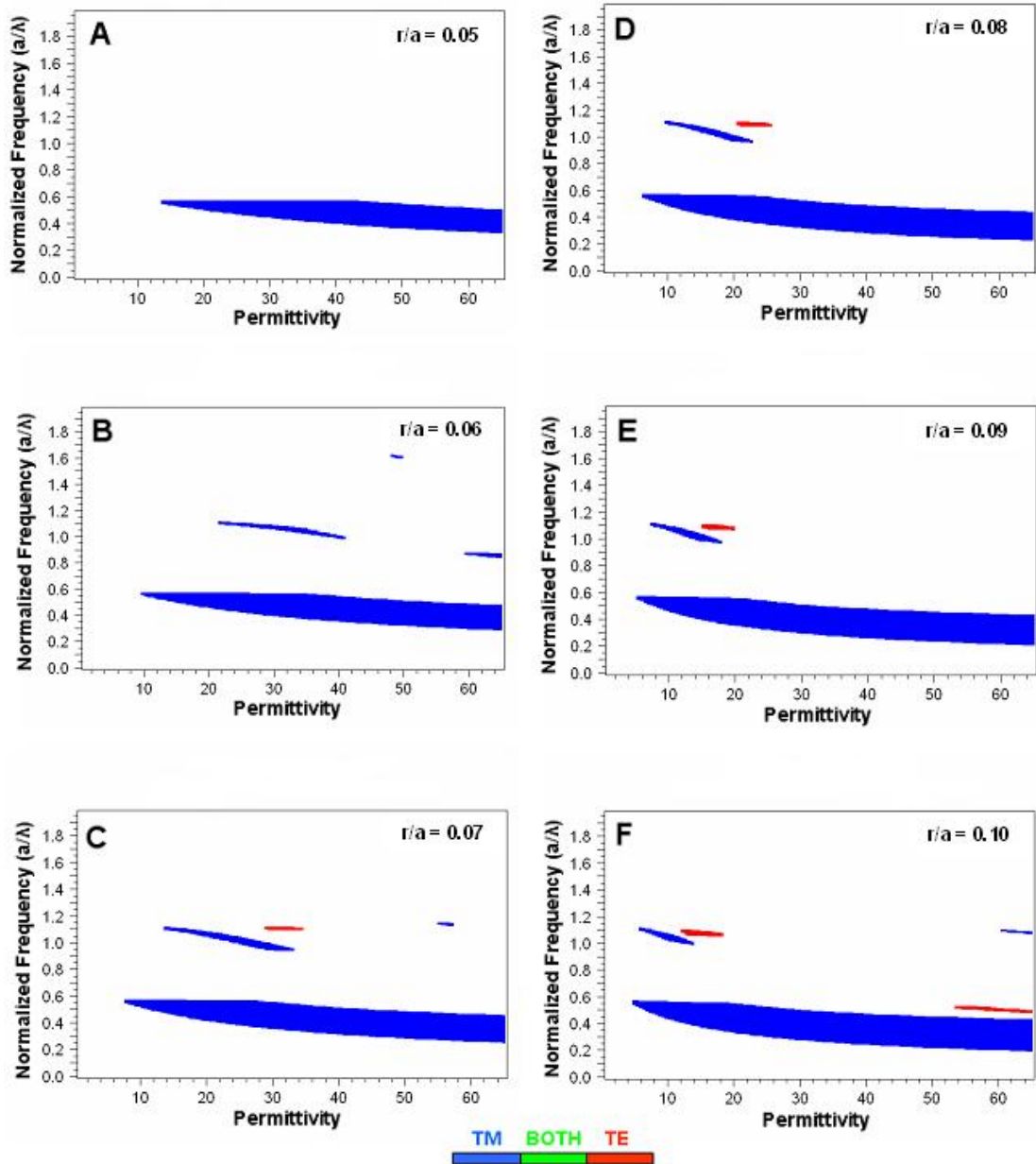


Figure 3.2: The dynamics of the photonic band gap with varying permittivity (3 to 65) and filling factors [(A)  $r/a=0.05$ , (B)  $r/a=0.06$ , (C)  $r/a=0.07$ , (D)  $r/a=0.08$ , (E)  $r/a=0.09$  and (F)  $r/a=0.10$ ]. Each plot has permittivity on the x-axis and normalized frequency on the y-axis. The shaded region indicate regions of global band gap where blue is for TM gaps, red is for TE gaps and green for both.

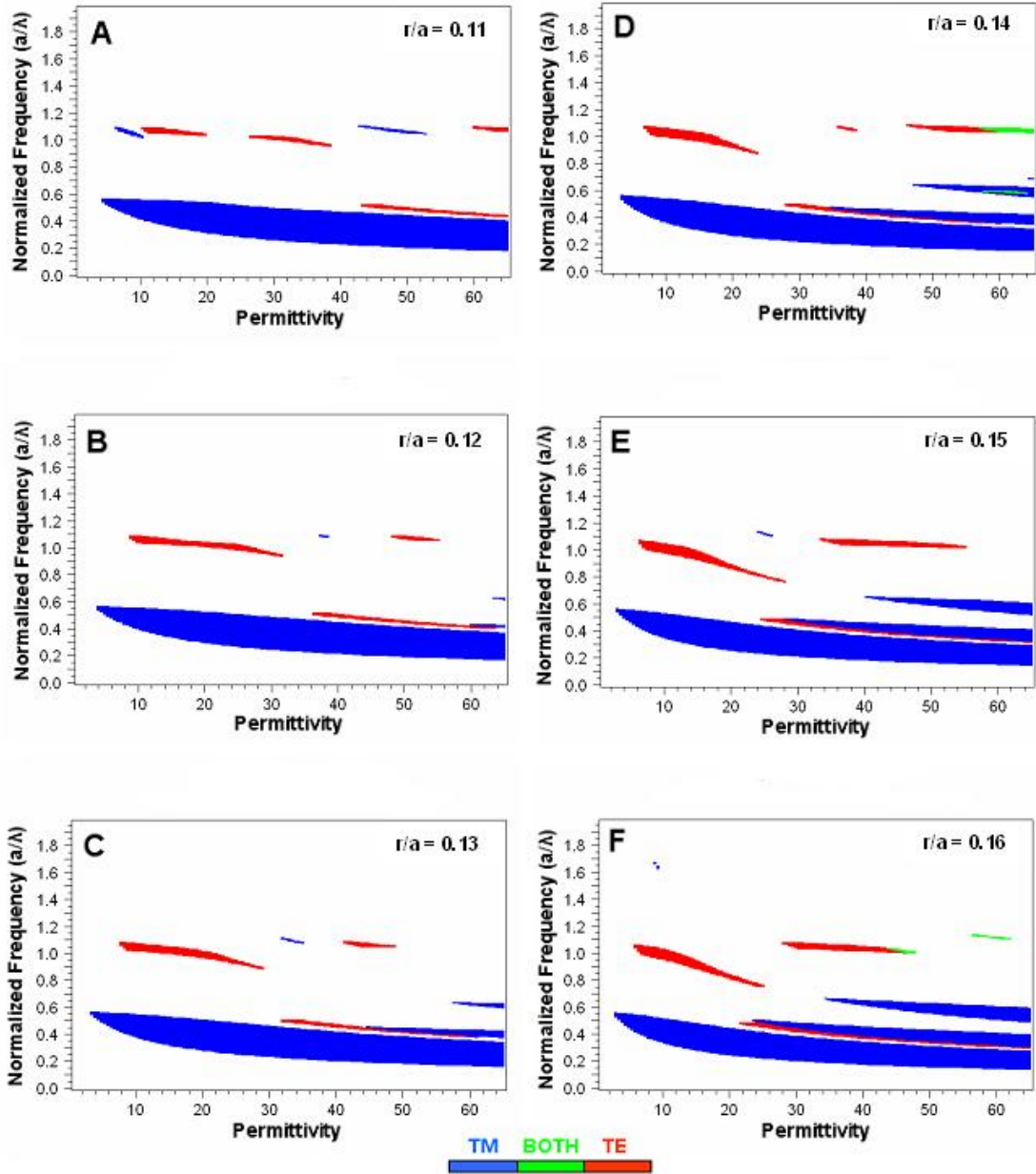


Figure 3.3: The dynamics of the photonic band gap with varying permittivity (3 to 65) and filling factors [(A)  $r/a=0.11$ , (B)  $r/a=0.12$ , (C)  $r/a=0.13$ , (D)  $r/a=0.14$ , (E)  $r/a=0.15$  and (F)  $r/a=0.16$ ]. Each plot has permittivity on the x-axis and normalized frequency on the y-axis. The shaded region indicate regions of global band gap where blue is for TM gaps, red is for TE gaps and green for both.

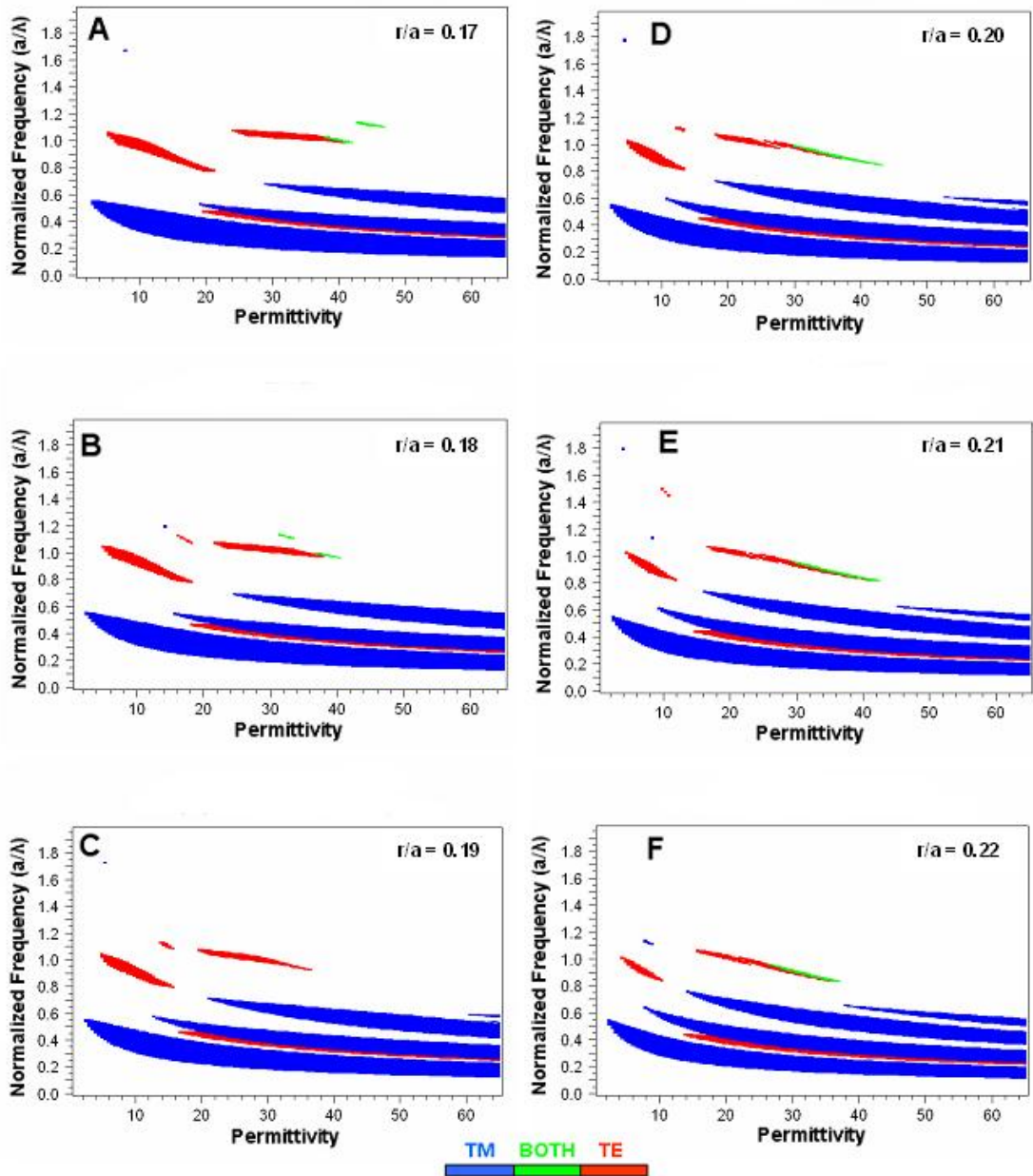


Figure 3.4: The dynamics of the photonic band gap with varying permittivity (3 to 65) and filling factors [(A)  $r/a=0.17$ , (B)  $r/a=0.18$ , (C)  $r/a=0.19$ , (D)  $r/a=0.20$ , (E)  $r/a=0.21$  and (F)  $r/a=0.22$ ]. Each plot has permittivity on the x-axis and normalized frequency on the y-axis. The shaded region indicate regions of global band gap where blue is for TM gaps, red is for TE gaps and green for both.

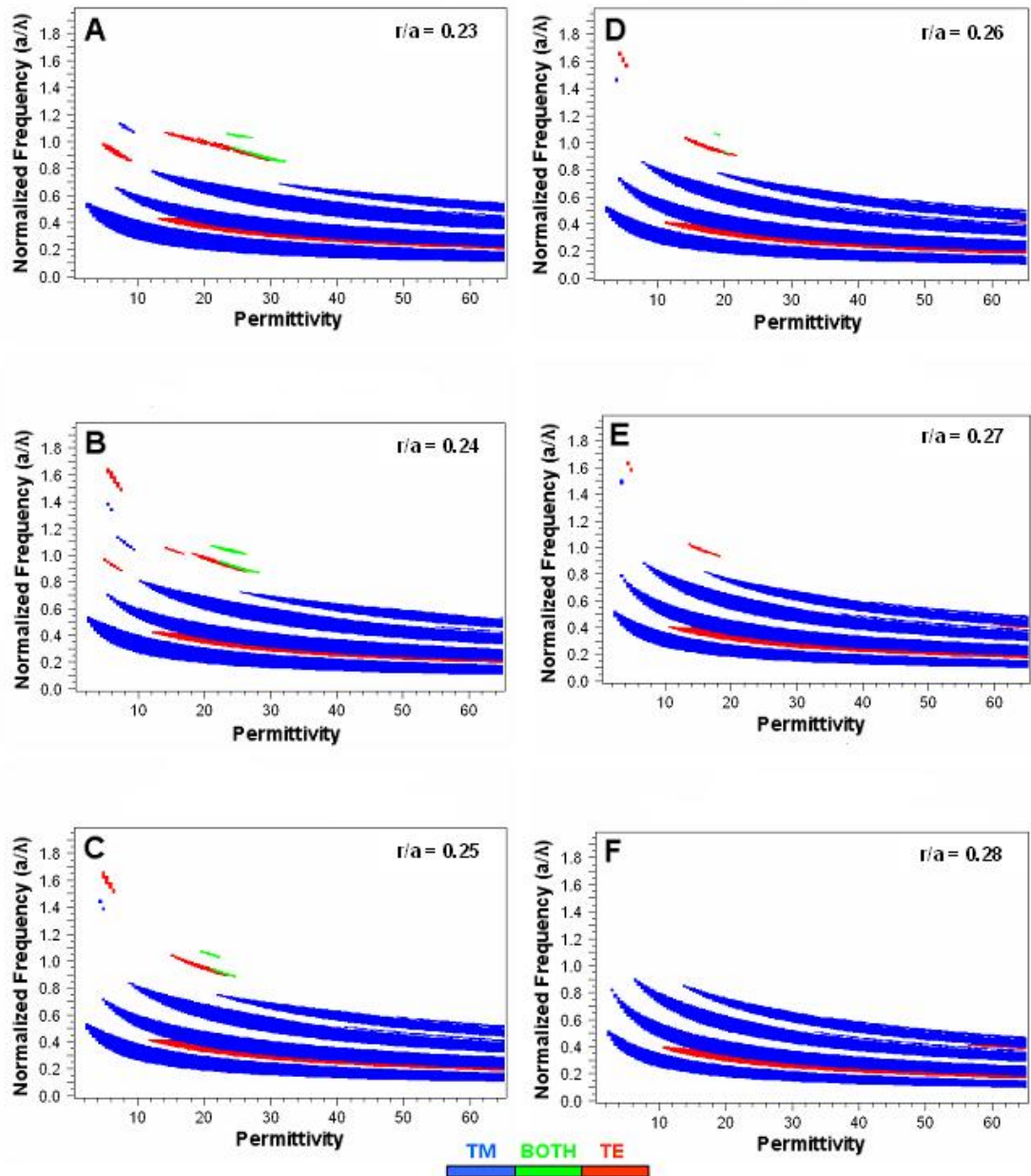


Figure 3.5: The dynamics of the photonic band gap with varying permittivity (3 to 65) and filling factors [(A)  $r/a=0.23$ , (B)  $r/a=0.24$ , (C)  $r/a=0.25$ , (D)  $r/a=0.26$ , (E)  $r/a=0.27$  and (F)  $r/a=0.28$ ]. Each plot has permittivity on the x-axis and normalized frequency on the y-axis. The shaded region indicate regions of global band gap where blue is for TM gaps, red is for TE gaps and green for both.

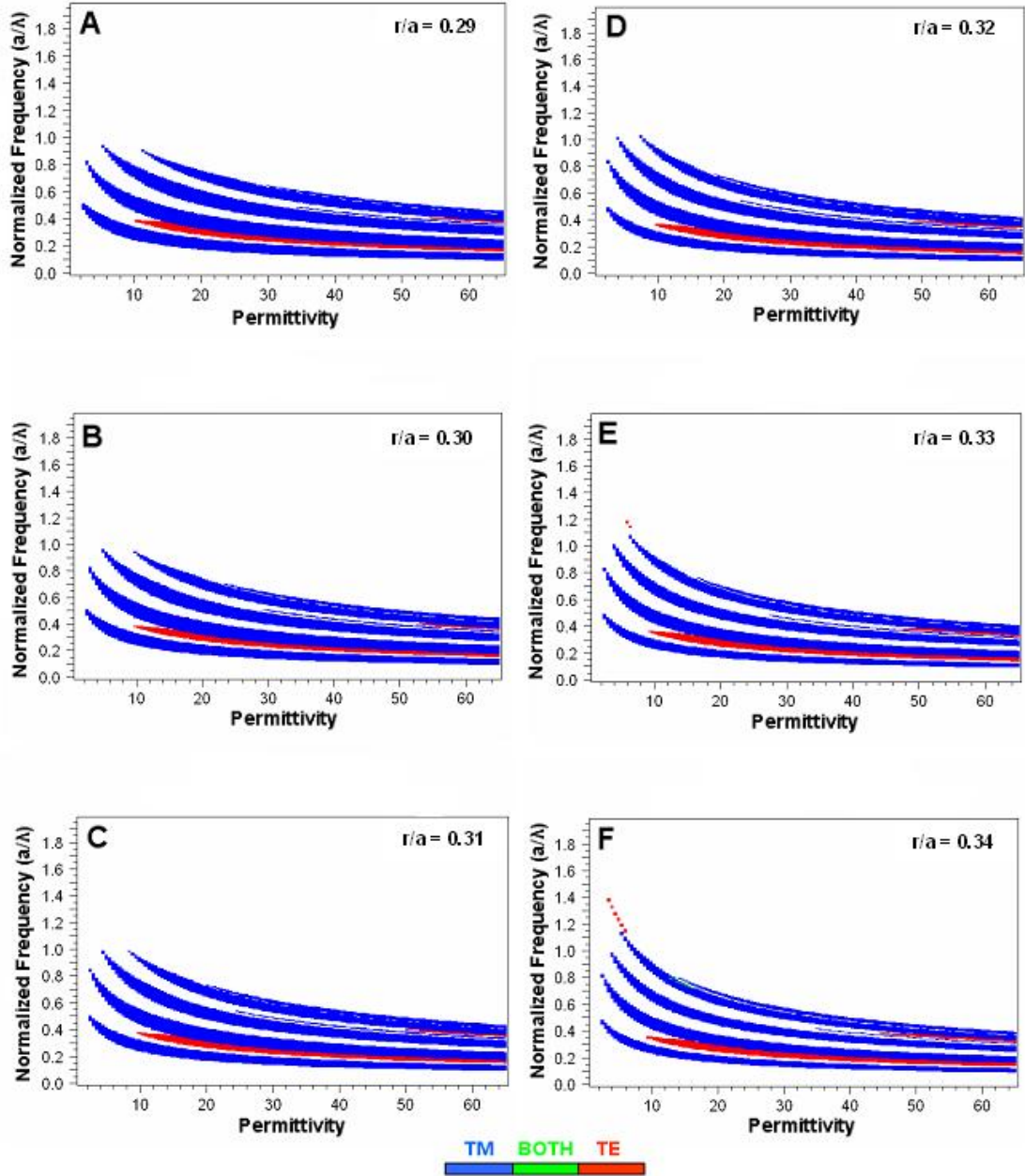


Figure 3.6: The dynamics of the photonic band gap with varying permittivity (3 to 65) and filling factors [(A)  $r/a=0.29$ , (B)  $r/a=0.30$ , (C)  $r/a=0.31$ , (D)  $r/a=0.32$ , (E)  $r/a=0.33$  and (F)  $r/a=0.34$ ]. Each plot has permittivity on the x-axis and normalized frequency on the y-axis. The shaded region indicate regions of global band gap where blue is for TM gaps, red is for TE gaps and green for both.

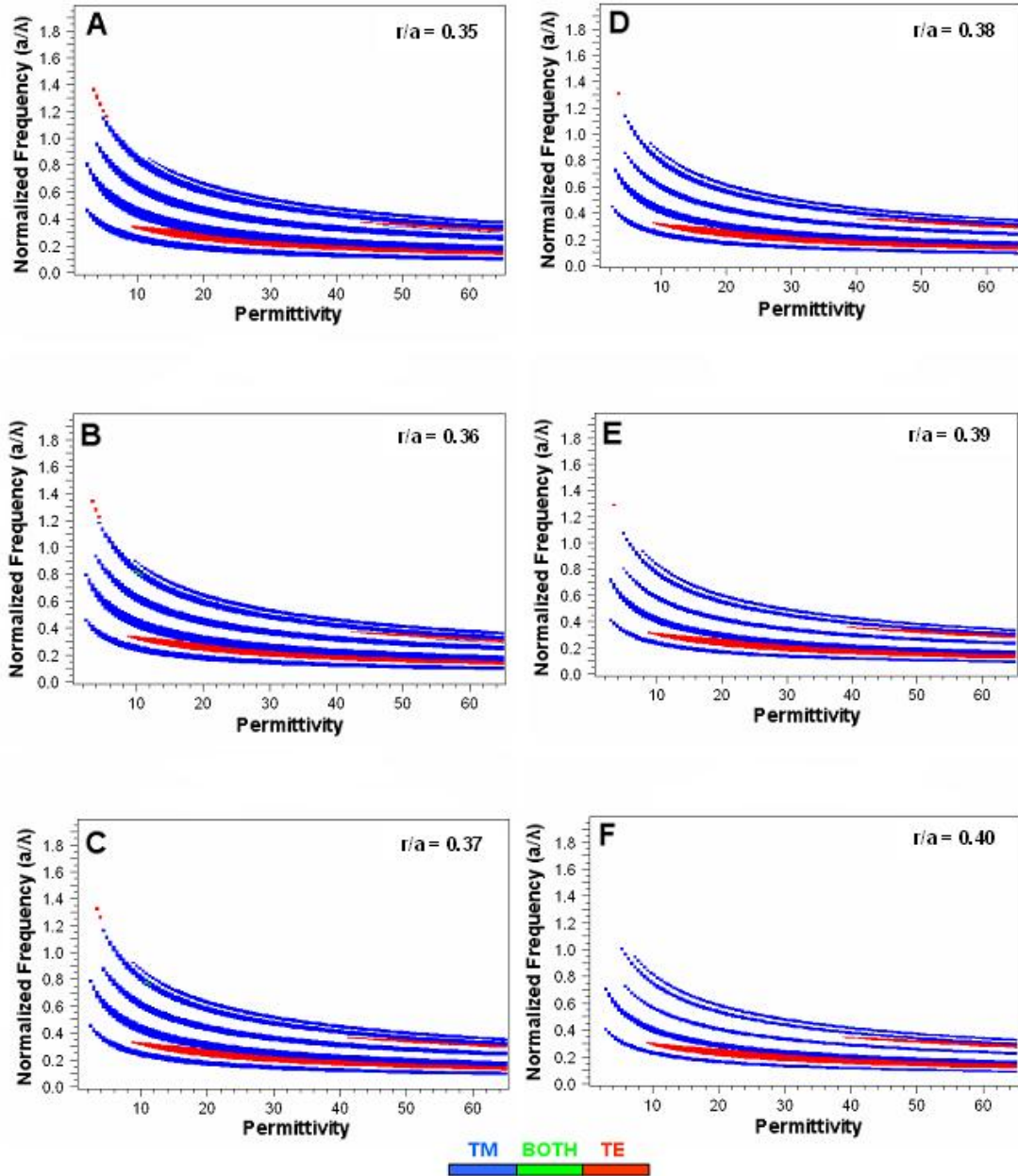


Figure 3.7: The dynamics of the photonic band gap with varying permittivity (3 to 65) and filling factors [(A)  $r/a=0.35$ , (B)  $r/a=0.36$ , (C)  $r/a=0.37$ , (D)  $r/a=0.38$ , (E)  $r/a=0.39$  and (F)  $r/a=0.40$ ]. Each plot has permittivity on the x-axis and normalized frequency on the y-axis. The shaded region indicate regions of global band gap where blue is for TM gaps, red is for TE gaps and green for both.

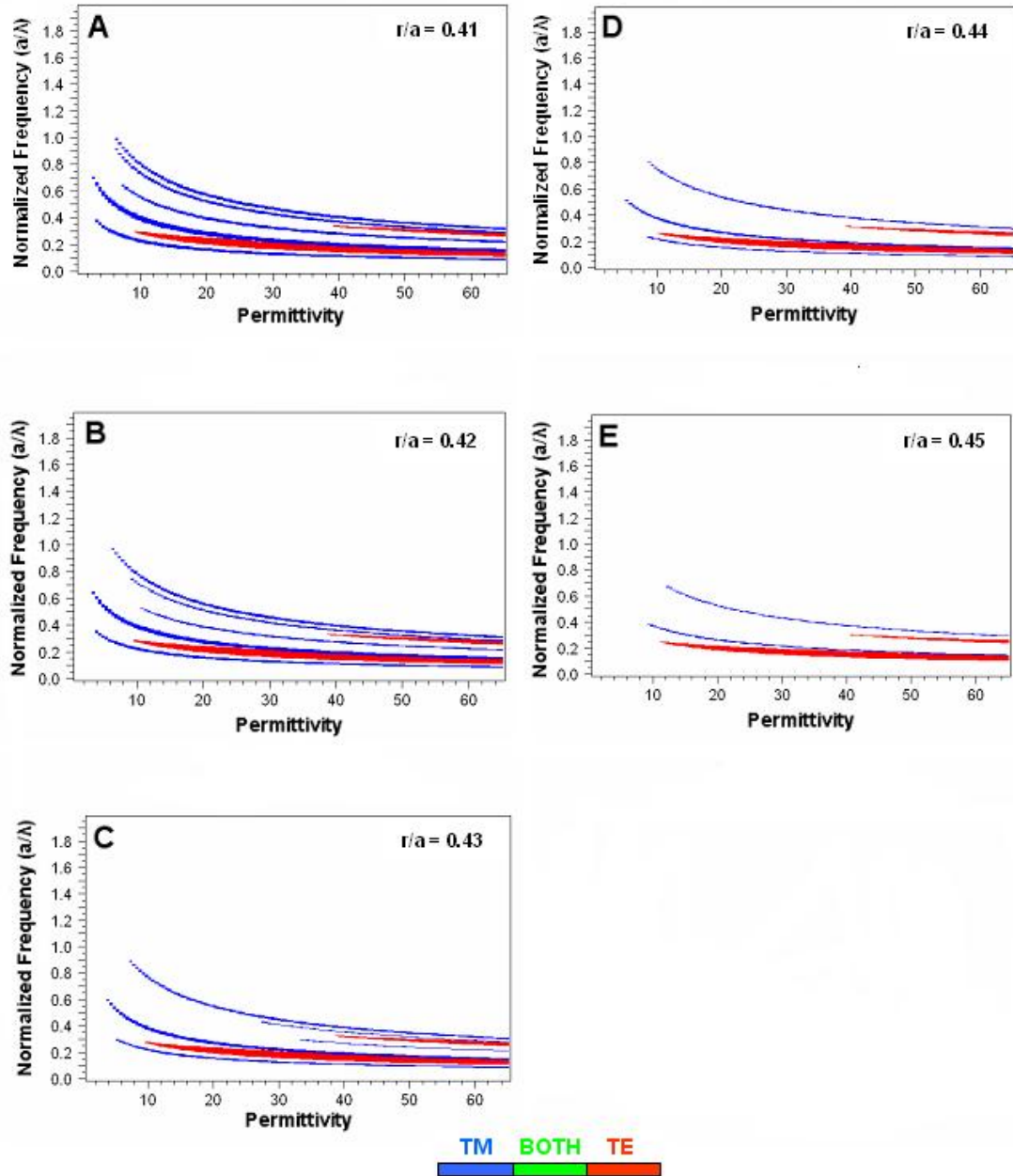


Figure 3.8: The dynamics of the photonic band gap with varying permittivity (3 to 65) and filling factors [(A)  $r/a=0.41$ , (B)  $r/a=0.42$ , (C)  $r/a=0.43$ , (D)  $r/a=0.44$ , and (E)  $r/a=0.45$  ]. Each plot has permittivity on the x-axis and normalized frequency on the y-axis. The shaded region indicate regions of global band gap where blue is for TM gaps, red is for TE gaps and green for both.

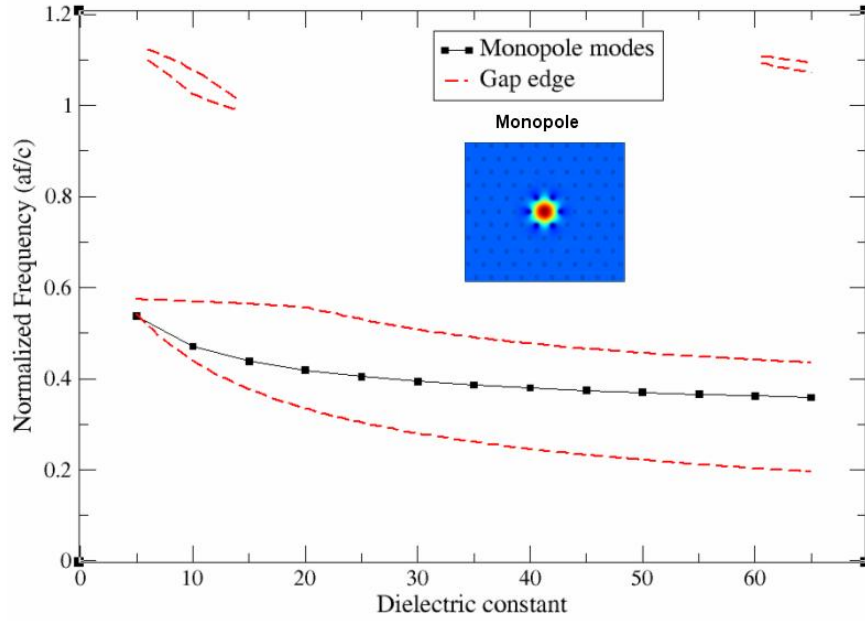


Figure 3.9: Dynamics of the confined Bloch states within the band gaps with varying permittivity. The Triangular lattice ( $r/a = 0.1$ ) was perturbed with a point defect as shown in figure 3.1-A. The normalization of the frequency was done by comparing the wavelength of Bloch states to the lattice constant  $a$ . The electric field profile of the monopole-like Bloch states is shown in the inset with the peak at the centre of the defect.

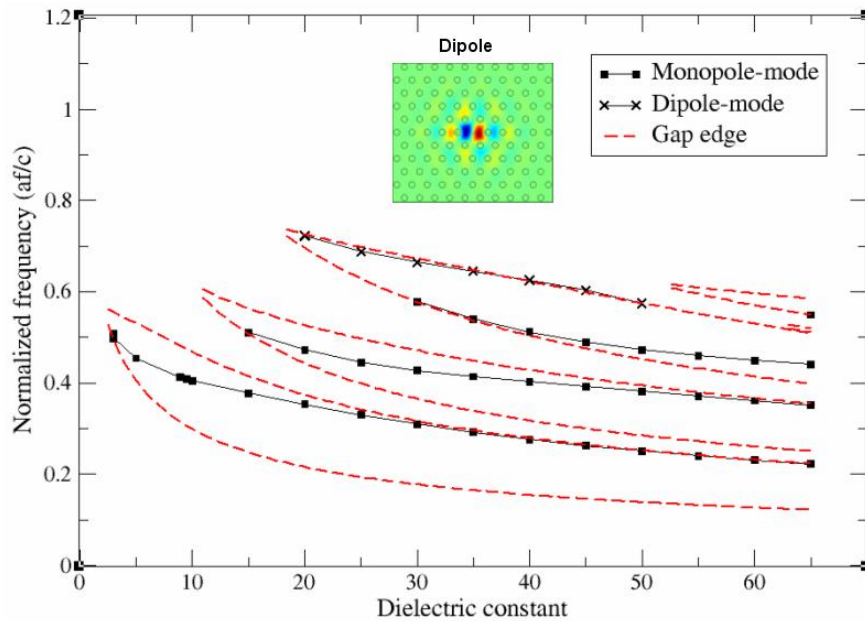


Figure 3.10: Dynamics of the confined Bloch states within the band gaps with varying permittivity. Triangular lattice ( $r/a = 0.2$ ) was perturbed with a point defect as shown in figure 3.1-A. The normalization of the frequency was done by comparing the wavelength of Bloch states to the lattice constant  $a$ . The electric field profile of the dipole-like Bloch states is shown in the inset with a node at the centre of the defect.

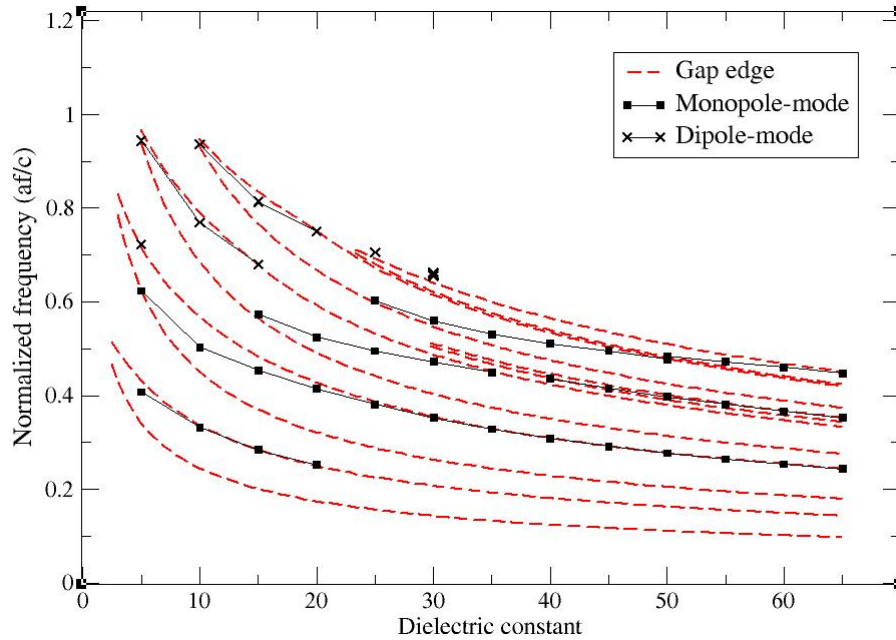


Figure 3.11: Dynamics of the confined Bloch states within the band gaps with varying permittivity. Triangular lattice ( $r/a = 0.3$ ) was perturbed with a point defect as shown in figure 3.1-A. The normalization of the frequency was done by comparing the wavelength of Bloch states to the lattice constant  $a$ .

in the first band gap, although higher order band gaps confine both monopole and dipole-like states. In figures 3.10 and 3.11 the frequencies of confined states move towards the upper edge of the gap with increasing permittivity. Furthermore only at lower values of  $r/a$  ( $\leq 0.1$ ) are single gap PC structures obtained. This is in contrast to the result of [165], where the point defect of a photonic crystal (PC) of air holes in a dielectric slab was shown to confine only dipole modes. In [165] the energy of the confined mode is concentrated in the dielectric slab where an air hole was removed. In contrast, this study finds that a point defect in a PC made from dielectric rods in air will only confine monopole states. Using FEM and PWE techniques, as in [43] we found that the states in the first band, concentrate their energy in the dielectric. In terms of the band diagram, bands where the energy

of the state is primarily stored in the dielectric (see figure 3.12-C) are referred to as the dielectric band. EM waves propagating in the top band (referred to as air band) store their energy primarily in the air-region of the lattice (see figure 3.12-B). From perturbation theory, decreasing/increasing the effective refractive index  $n$  in a local region of a photonic lattice result in defect states to be pulled-up/pushed-down from the dielectric/air band into the bandgap [167]. This is because for non-magnetic materials the refractive index is  $n = \sqrt{\epsilon_r}$  and the effective  $n$  in our structures is a function of the filling factor of the dielectric material in the local defect region [168]. The dependence of the EM field energy distribution on  $\epsilon_r$ , between dielectric and air regions explains the drop in the frequency of the band gap in figures 3.2, 3.3, 3.4, 3.5, 3.6, 3.7, and 3.8 with increase in  $\epsilon_r$ .

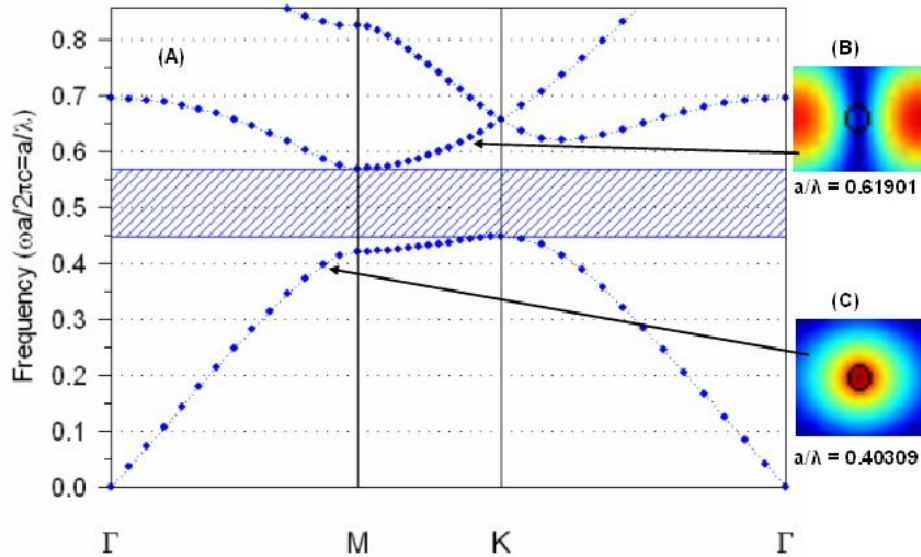


Figure 3.12: Dispersion diagram of triangular lattice ( $r/a = 0.1$ ) showing the propagation bands (A) from PWE. The shaded region is the bandgap. The electric field profile (from COMSOL) of the air band (B) with peak field in the air region around the scatterers and the dielectric band (C) with peak field in the dielectric scatterer (region inside the black ring) is shown in the inset. The blue/red (black/white) region of (B) and (C) are the low/high electric field regions. The permittivity of the scatterers is 9.5.

This work was then extended by increasing the defect volume, by the removal of a second scatterer as shown in figure 3.1(B). We focus on a lattice with  $r/a = 0.1$ , as from figure 3.9 we see this value yields a single band-gap. Compared to the single point defect case, in the double defect case, shown in figure 3.13, as the permittivity is increased the band gap appears and a dipole mode is confined. As the permittivity is increased further, a monopole mode enters into the band gap and becomes confined to the defect. The frequency of this confined monopole-like state is closer to the lower edge of the band gap compared to the single defect case, which is due to the increased volume of the defect. Note that the electric field profile (see figure 3.12-C) of the dielectric band EM states do not have nodes in the dielectric scatterers. When a radially symmetric point defect is created by removing a single dielectric scatterer, the symmetry of the dielectric band EM state is retained in the defect volume and a nodeless monopole-like defect state is confined to the defect region (see figure 3.9 inset). An elongated double defect region confines both a dipole-like defect state with a central node, and an elongated monopole-like state, as shown in figure 3.13 (inset). In the double defect case, the dipole-like mode was pulled into the band gap before the monopole-like defect state. The frequency of both the monopole and dipole confined states, and the frequency range of the band gap, decreases with increasing permittivity. This behaviour can be understood in terms of the Rayleigh quotient (Re) [131], where increasing

the permittivity decreases the angular frequency of the states in each band [43].

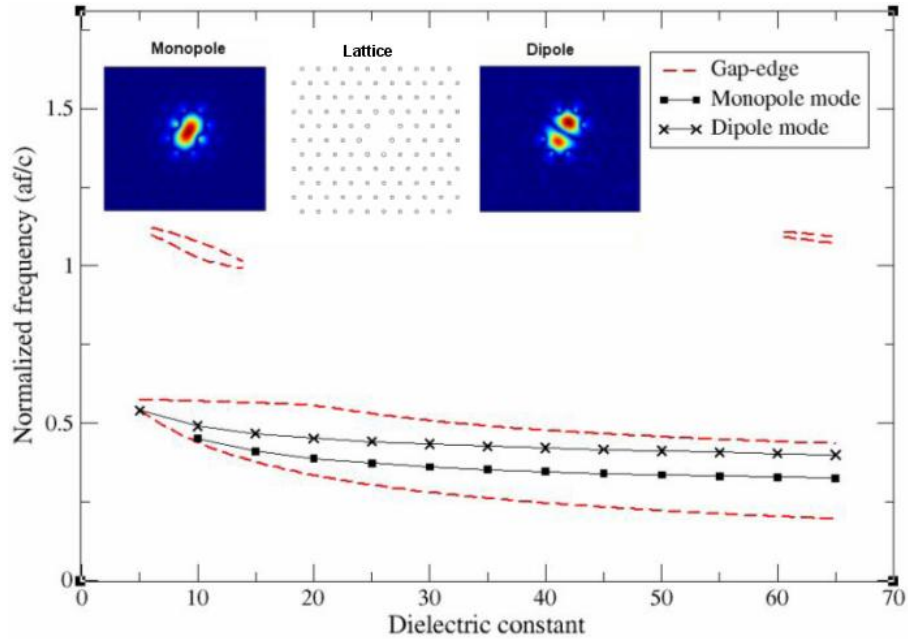


Figure 3.13: Dynamics of the confined Bloch states introduced into the band gaps by a double diagonal defect (two diagonal rods removed), at the centre of the triangular lattice as shown in figure 3.1-B with  $r/a = 0.1$ . The normalization of the frequency was done by comparing the wavelength of Bloch states to the lattice constant  $a$ . The electric field profile of the confined EM states and the lattice is shown in the inset.

In figures 3.9, 3.10, 3.11 and 3.13 we noticed that the band gap drops in frequency faster than the frequency of the confined EM states. This is due to the perturbation in the local region where the defect states are confined. From perturbation theory, a negative change  $-\Delta n$  (decrease) in the effective refractive index ( $n = \sqrt{\epsilon}$ ) in a local region will cause an increase in the frequency of the states confined in the defect region [43]. The frequency of the states in the propagation band are less affected by the defect as this perturbation is small compared to the bulk lattice. Similar to figure 3.9, the two higher order band gaps in figure 3.13 do not confine EM fields, and at

lower values of  $\varepsilon$  ( $\leq 10$ ) the confined monopole-like states are close to the lower edge of the first band gap.

### **3.4 Dynamic of confined EM states with variation in the radius of innermost rods closest to the double defect**

The authors of [157] and [165] have demonstrated that variations in the innermost scatterers surrounding a photonic resonator alters the frequency of EM states confined within the defect region. In this chapter, this effect was studied and used to *shift* the monopole mode of figure 3.13, which is confined within the defect region into the propagating dielectric band, to leave only the dipole state confined to the defect region. A triangular lattice with  $r/a = 0.1$  was chosen as it offers a single band gap. The permittivity of the scattering rods was chosen to be 9.5 as this corresponds with commercial available Dynalox100. The ratio  $R/a$  of the innermost rods was varied by altering the radius  $R$  of scatterers closest to the defect from 0.095 to 0.16 in steps of 0.05. The results of this variation are shown in figure 3.14, where we see that the frequencies of both monopole and dipole like Bloch states decrease with increased  $R/a$ . This can be explained by perturbation theory where an increase in the effective refractive index in a local defect region causes a decrease in the frequency of confined states[43, 167].

At  $R/a = 0.11$ , the monopole-like Bloch state slips below the

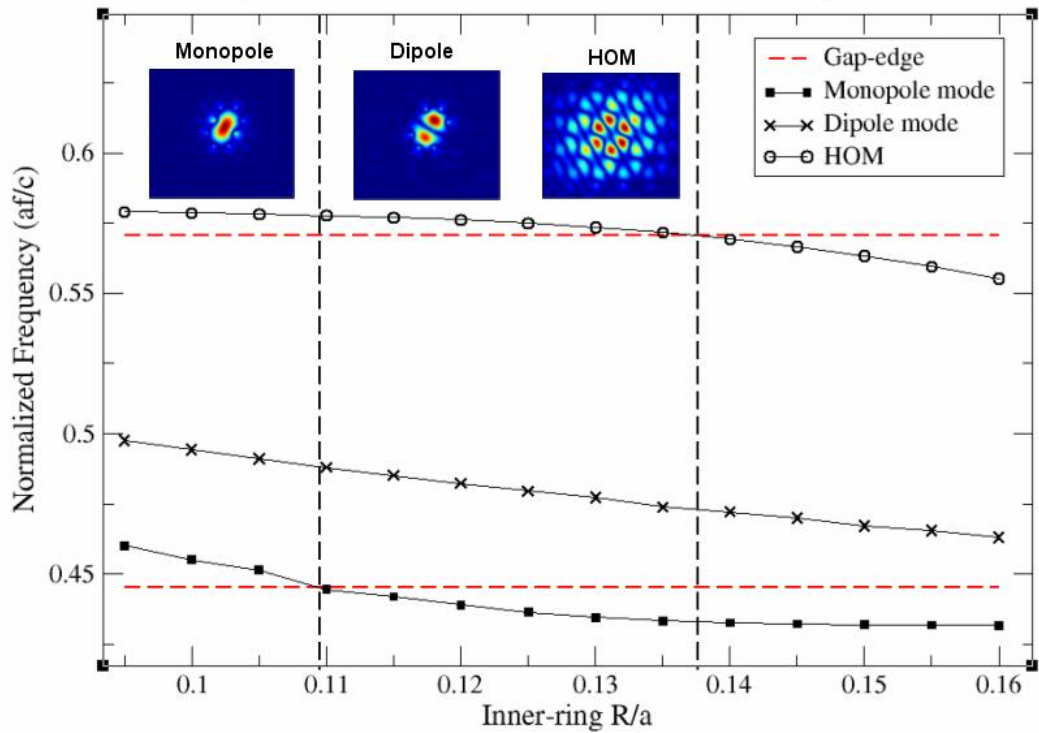


Figure 3.14: The effect of varying the radius  $R$  of the innermost rods around the double diagonal defect (two diagonal rods removed) as shown in figure 3.1-C, on the confined Bloch states. Triangular lattice with bulk ratio  $r/a = 0.1$  and permittivity  $= 9.5$ . The field profile of the modes is shown in the inset. The region between the vertical dashed lines can be used for the design of a dipole photonic resonator. The normalization of the frequency was done by comparing the wavelength of Bloch states to the lattice constant  $a$ .

lower edge of the band gap. As the frequency of the modes continue to drop, HOMs are introduced into the band gap at  $R/a = 0.14$ . The region between the two dashed lines in figure 3.14 is the operational region where only the dipole Bloch state is confined within the band gap and all other EM states are able to propagate away.

### 3.5 Quality factor improvement for confined Bloch states

In order to demonstrate the confinement of the dipole-like Bloch states and the extended state of the monopole mode, the radiative  $Q$  of each state was plotted against  $R/a$ . The quality factor of an EM state is the ratio of its energy stored within the defect region to the rate at which energy is lost to the bulk lattice. The results of the  $Q$  dependence are shown in figure 3.15, where we see that the radiative quality factor of the monopole EM state decreases as it leaves the band gap while the radiative quality factor of the dipole state increases until HOMs enters the band gap.

For application such as *crabbing* in particle accelerators, it is critical that a resonator can support only the dipole mode with a high  $Q$ , and that all other modes have a very lower  $Q$ . Although the  $Q$ -factor presented here is only the radiative  $Q$ , the point that the dipole  $Q$  is high with respect to the  $Q$  of all other modes remains true. In any real structure using the lattice outlined here, the  $Q$  would be limited by the ohmic losses in the metallic sides (this is shown in chapter

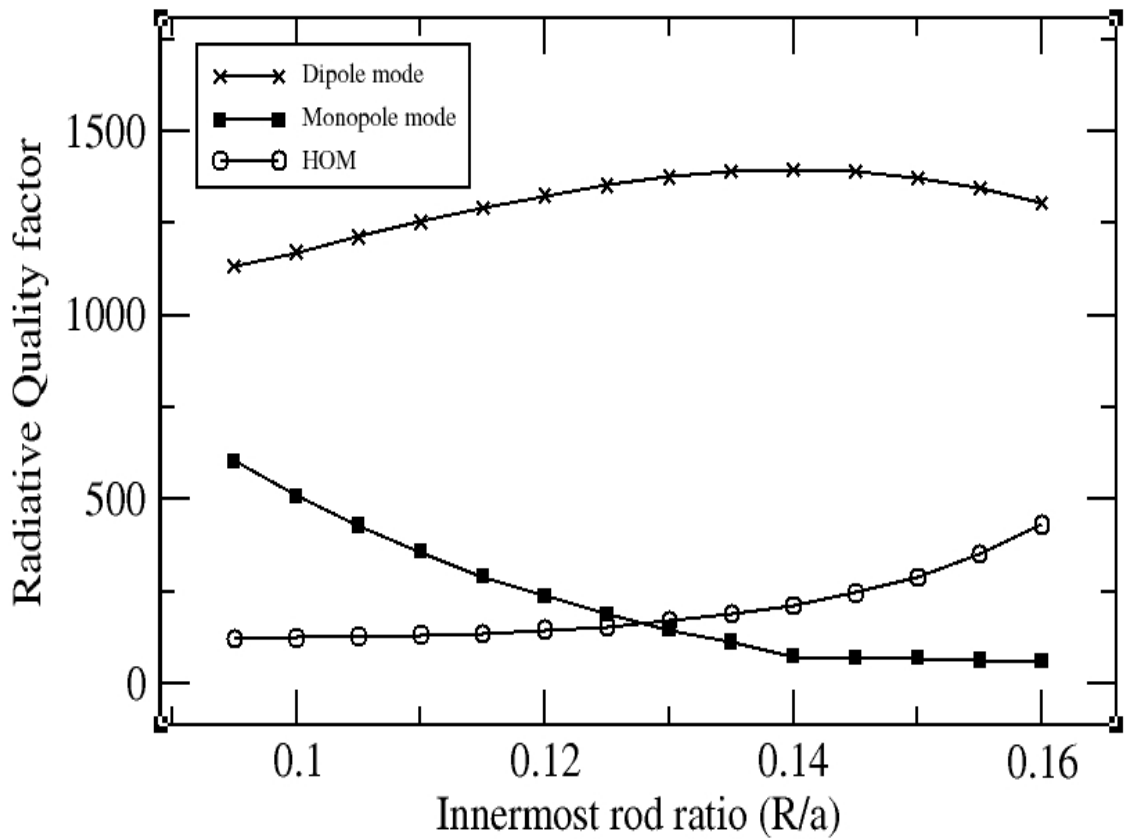


Figure 3.15: A plot of the radiative quality factor of both monopole and dipole modes with varying ratio  $R/a$  of the innermost rods around the double diagonal defect as shown in figure 3.1-C. Triangular lattice with bulk ratio  $r/a = 0.1$  and permittivity = 9.5.

4). We demonstrate in figure 3.16 that higher  $Q$  can be achieved by increasing the number of scatterers surrounding the defect region of the structure, a result that was first shown in [163, 169]. From figure 3.16 we see that increasing the number of scatterers on all sides of the defect from 4 to 10 rows, the radiative quality factor of the dipole EM state increased from  $1.38 \times 10^3$  to  $4.14 \times 10^6$ , whereas the quality factor of the monopole mode only increased from  $1.47 \times 10^2$  to  $1.00 \times 10^3$ .

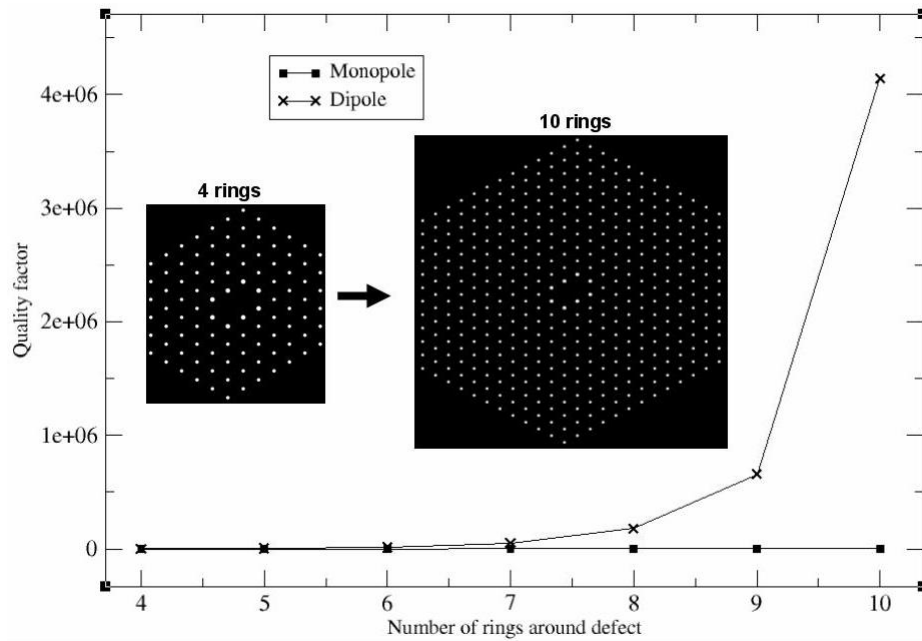


Figure 3.16: Quality factor improvement using larger PBG lattice dimensions. Triangular lattice with bulk ratio  $r/a = 0.1$ , permittivity = 9.5, a double diagonal defect, and innermost ring ratio  $R/a = 0.13$ .

In this chapter, we have systematically studied the dependence of EM modes confined in both single point and double point defects. We studied the frequency dependence of the confined EM states on the lattice parameter surrounding the defect region. We found that the frequency of the bandgaps drops faster than the confined modes

with increasing permittivity. In a lattice where only monopole-like states are confined by a point defect, we found that dipole-like states can be pulled into the bandgap with the creation of a double point defect. Finally we found that the frequencies of confined modes can be increased/decreased within the bandgap by varying the radius of scatterers close to the defect region. A PC lattice that confines only the dipole-like Bloch state while allowing all other EM states to propagate away has been demonstrated. A similar approach can be employed to design monomodal structures that confine only monopole, quadrupole or higher order modes. The confinement of a dipole state using the PC outlined above could offer advantages in applications in particle accelerators, such as crabbing. In the following chapter, the lattice design presented here is used to design a photonic band gap crab cavity.

# Chapter 4

## Dipole PC Crab Cavity

### 4.1 Introduction

In this chapter, a dipole PC crab cavity is implemented. The lattice design presented in chapter 3 was used to confine the dipole mode required for crabbing. The concept of crabbing has been introduced in chapter 1 along with advances in high power dipole resonating cavities in section 1.3 of chapter 1. As stated in chapter 1, crab cavities have never been designed to benefit from the mode selective capability of photonic crystals. Conventional deflecting cavities are usually characterized by figures of merit which include the transverse R/Q, peak surface fields and the group velocity [69]. R is the shunt impedance of the cavity while Q is the unloaded quality factor. In conventional deflecting cavities, the longitudinal voltage  $V_z(x, y)$  along the cavity length  $d$  is given by:-

$$V_z(x, y) = \int_0^d E_z(x, y, z) e^{\frac{i\omega z}{c}} dz \quad (4.1)$$

The longitudinal  $R/Q_{\parallel}$  of a mode with angular frequency  $\omega$  and stored energy  $U_{cav}$  is given by:-

$$\frac{R}{Q_{\parallel}}(x, y) = \frac{V_z^2(x, y)}{2\omega U_{cav}} \quad (4.2)$$

In an ideal deflecting pillbox cavity, the dipole  $TM_{110}$  mode has no electric field on axis ( $x = y = 0$ ) as seen by the particle bunch. The transverse deflecting momentum imparted to the particles is obtained only from the magnetic fields. However for practical reasons, it is necessary to open up irises which connect to the beam tube to allow the particle bunch access into the deflecting cavity. The new boundary condition of the beam tubes and the irises introduces a TE-like mode which mixes with the TM modes of the cavity and creates a hybrid of the  $TM_{110}$  and the  $TE_{111}$  modes. In this practical case where the transverse momentum is supplied by both the magnetic and the electric fields, the Panofsky-Wenzel theorem [170](discussed in Appendix B) offers a convenient approach to calculating the transverse  $R/Q$ . The Panofsky-Wenzel theorem assumes both that (1) the transverse electric field vanishes at the boundary of the cavity and (2) the particles are fast and rigid enough so their direction is essentially unchanged as they travel through the cavity. As pointed out in [171], Panofsky-Wenzel theorem is independent of the polarization of the excited modes within the deflecting cavity as long as the assumptions stated above are followed. The transverse voltage  $V_{\perp}(x, y)$  relates to the longitudinal voltage  $V_z(x, y)$  as follows:-

$$V_{\perp} = -ic\nabla V_z(x, y) \quad (4.3)$$

Since the magnitude of the electric field  $E_z$  of a  $TM_{110}$  mode is zero on the Z-axis (the node point), therefore  $V_z(x = y = 0) = 0$ .  $c$  is the speed of light in free space and  $x_0$  is the offset distance away from the beam axis. The  $-i$  term indicate that the transverse voltage  $V_{\perp}(x, y)$  like the magnetic field has a  $90^{\circ}$  phase advance relative to the longitudinal voltage  $V_z(x, y)$ . However, the transverse voltage can be calculated from the longitudinal voltage taken at an offset distance away from the Z-axis as follows:

$$V_{\perp} = \frac{-icV_z(x_0)}{\omega x_0} \quad (4.4)$$

Also the transverse R/Q is given as:

$$\frac{R}{Q_{\perp}} = \frac{V_{\perp}^2}{2\omega U_{cav}} \quad (4.5)$$

The transverse  $R/Q$  is an important figure of merit for the robustness of the cavity design as it relates the deflecting force received by the beam to the stored energy within the cavity. The peak surface fields of any deflecting cavity depend on the RF power source driving the cavity and the material used to build the cavity. It is therefore difficult to directly compare any two different cavity designs. However, since the transverse gradient  $E_{\perp} = \frac{V_{\perp}}{d}$  is proportional to the peak fields, the normalized peak electric  $\frac{E_{\perp}}{E_{peak}}$  and magnetic  $\frac{H_{peak}}{E_{\perp}}$

fields quantities can be calculated. These normalized quantities depend on the geometric design of the deflecting cavity and provides a means of comparing different cavity designs. In order to prevent surface melting and breakdown, the peak surface fields is generally desired to be lower for any desired transverse gradient [69]. This means that a higher  $\frac{E_{\perp}}{E_{peak}}$  and a lower  $\frac{H_{peak}}{E_{\perp}}$  is preferred. The authors of [69] also found that the peak magnetic field is concentrated around the iris of the cavity. This can cause heating of the iris, potentially damaging it. Therefore the geometric parameters of the iris have to be optimized to minimize  $\frac{H_{peak}}{E_{\perp}}$ . Since the crabbing scheme is only a part of a bigger collider facility, the beam parameters and the Interaction Point (IP) requirement are usually considered in the design of crab cavities. For a beam energy  $U_{beam}$ , a transfer matrix  $R_{12}$  of the focusing system (between the crab cavity and the IP) and a crossing angle  $\theta_c$  at the IP, the required transverse voltage is given by:-

$$V_{\perp} = \frac{\theta_c U_{beam} c}{2\omega R_{12}} \quad (4.6)$$

Equation 4.6 suggests that a crab cavity designed to operate at higher frequency will require lower transverse voltage  $V_{\perp}$  to achieve a given amount of deflection. The  $R_{12}$  of the final focusing scheme relates the angular deflection angle  $x'$  at the crab cavity to the vertical displacement  $x_{IP}$  at the IP as shown in equation 4.7 and illustrated in figure 4.1.

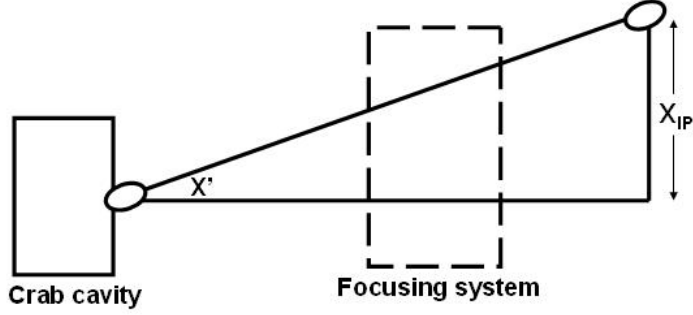


Figure 4.1: Schematic diagram showing the transverse displacement of the bunch off axis as it is rotated by the crab cavity.

$$x_{IP} = R_{12}x' = R_{12}\frac{V_{\perp}}{U_{beam}} \quad (4.7)$$

In [69] a study to optimize the compact linear collider (CLIC) crab cavity was done and a conclusion was made that a bigger coupling iris will lower the shunt impedance, increase the group velocity and lead to a reduced beam loading and an efficient RF control. In this chapter the effect of the iris parameters on  $R/Q$  and the surface fields is studied for a PC crab cavity. The PBG cavity is optimized for the CLIC operational frequency of 11.9942 GHz and a RF coupling scheme was designed. The result presented here for a single cell PBG structure compares well with those obtained for a conventional crab cavity [69] and with the added benefit of Wakefield suppression.

## 4.2 A PBG crab cavity

The EM state confined in the defect region of any PBG resonator is determined by the lattice parameter i.e. the radius of the rods  $r$ , the lattice constant  $a$ , and the material of the scatterers (permittivity).

The design of the PBG crab cavity presented here is based on the lattice design presented in chapter 3 where only a dipole mode is confined while all other modes propagate away from the defect region. The study in chapter 3 was done with a 2D numeric calculation and the results are presented in normalized units. The design process in this section begins with a direct scaling of the 2D result to useful units (GHz, meters). This is followed by a 3D HFSS simulation where the height of the cavity is introduced with realistic boundary condition. A Wakefield study was performed using Vorpil [155]. The eigenmode characteristic of the single cell PBG structure was optimized with respect to the beam tube and iris radius. A RF coupling scheme was designed for the PBG crab cavity and the final design parameters is presented. This section concludes with the investigation of dielectric breakdown in the PBG structure.

#### 4.2.1 Frequency scaling of the 2D lattice design

The result presented in figure 3.14 of chapter 3 is scaled from a normalized frequency unit to 11.9942 GHz and presented in figure 4.2. This was done by first selecting a central value of  $R/a = 0.12416$  from the operational range of 0.110 to 0.137 marked with the vertical dashed line in figure 3.14 of chapter 3. The triangular photonic lattice design from chapter 3 with bulk lattice ratio  $r/a=0.1$ , inner ring ratio  $R/a=0.12416$  and permittivity  $\varepsilon = 9.5$  will confine only the dipole  $TM_{110}$  mode at normalized frequency unit  $a/\lambda = 0.4798$ . The target frequency of 11.9942 GHz corresponds to a wavelength  $\lambda = 0.025\text{m}$

which is multiplied by  $a/\lambda = 0.4798$  to obtain the lattice constant  $a = 0.012\text{m}$ . This lattice constant was then used to calculate the values of the rod radius ( $r$ ) and the innermost rods radius ( $R$ ) to be  $0.0012\text{ m}$  and  $0.00149\text{ m}$  respectively. Also with a lattice constant  $a = 0.012\text{m}$ , the frequency of the monopole mode and the first HOM corresponds to  $10.92515\text{ GHz}$  and  $14.38361\text{ GHz}$  respectively. The band gap was calculated to be between  $11.1335\text{ GHz}$  to  $14.26175\text{ GHz}$ . The electric and magnetic field distributions of the dipole mode (shown in figure 4.3) were calculated with COMSOL [150]. A strong magnetic field was found to be concentrated around the innermost rods closest to the defect region. The effect of this field is discussed in section 4.4 of this chapter.

#### **4.2.2 Finite height scaling of the lattice design**

The lattice dimensions calculated in subsection 4.2.1 were used to implement a  $\pi$  phase advance PBG crab cavity in a 3D HFSS simulation with the top and bottom plates defined as a Perfect Electric Conductor (PEC). A  $\pi$  cavity has a height that is half the wavelength of the dipole mode and this corresponds to  $0.0125\text{ m}$  for a target frequency of  $11.9942\text{ GHz}$ . In the initial case with no iris and no beam tube, the change from an infinitely long lattice to one with a finite height results in a frequency shift of  $225\text{ MHz}$ . This shift in frequency was corrected by changing the lattice constant from  $0.012\text{ m}$  to  $0.01189\text{ m}$  which in turn yielded new values for  $r$  and  $R$  as  $0.001189\text{ m}$  and  $0.0014772\text{ m}$  respectively. Using these new dimen-

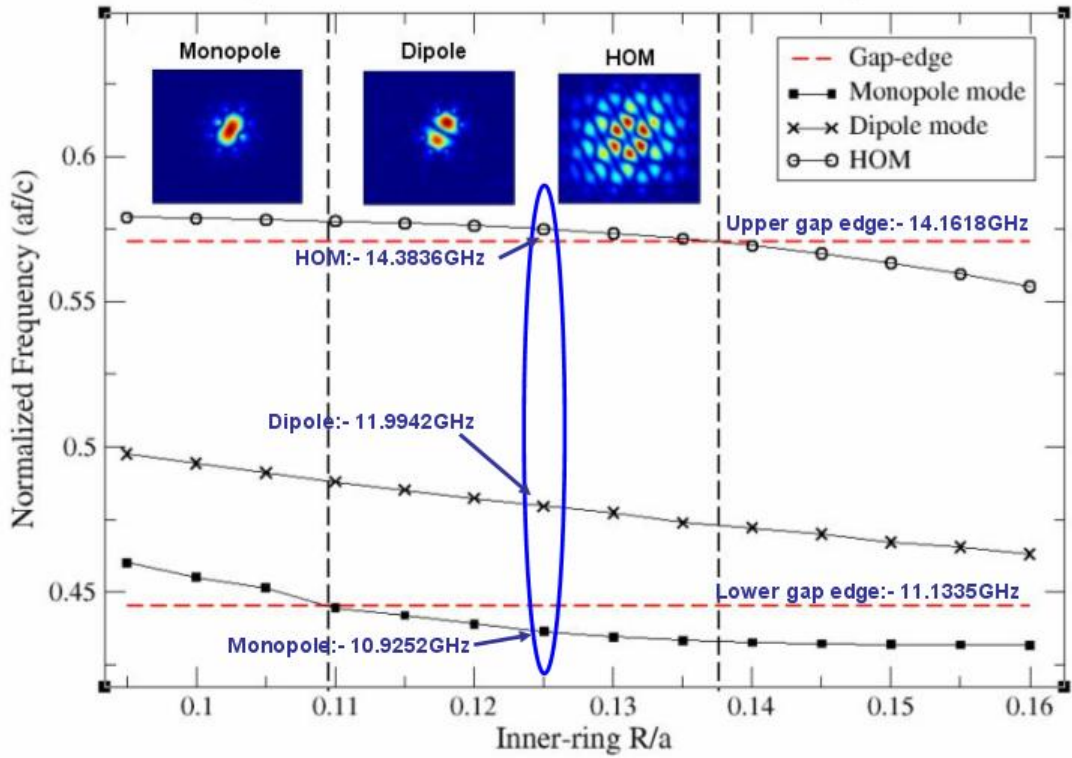


Figure 4.2: A triangular lattice with bulk ratio  $r/a = 0.1$ , dielectric constant  $\varepsilon = 9.5$ , a double diagonal defect, and innermost ring ratio  $R/a = 0.12416$  will confine only a dipole  $TM_{110}$ -like EM state at 11.9942 GHz. The EM states (monopole and HOM) below and above the band gap (marked by horizontal dashed lines) are allowed to propagate through the lattice.

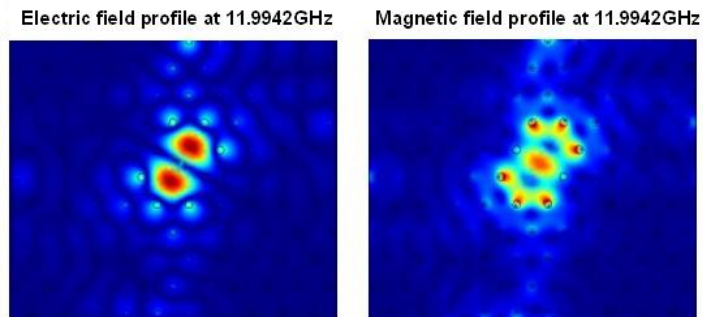


Figure 4.3: The field profile of a confined dipole  $TM_{110}$ -like EM state at 11.9942 GHz.

sions, a Wakefield study (similar to ref [39]) was performed to check if the finite height PBG structure will confine only the dipole mode as predicted by the results in chapter 3.

### 4.2.3 Suppression of long range Wakefields by PBG crab cavity

Wakefields created by the passage of a particle bunch through the PBG crab cavity can couple to the eigenmodes (LOM and HOMs) of the cavity. If these parasitic modes are not properly suppressed or dampened, they can linger long enough within the double point defect to adversely affect trailing bunches. In this subsection, the suppression of long range wakefields within the PC lattice is investigated by exciting the photonic resonator (shown in figure 4.4) with a Gaussian current bunch of length  $\sigma = 3$  mm.

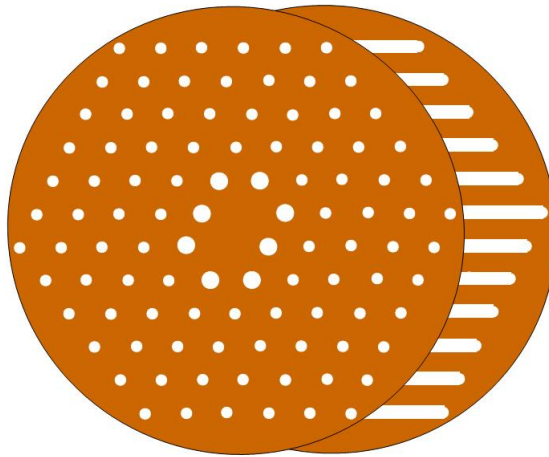


Figure 4.4: A PBG structure with triangular lattice of dielectric rods in air and metal ends. Two rods were removed to create a defect that is only able to confine a dipole mode. The particle bunch travels down the center of the cavity from one metal end to another.

Vorpal was set up to launch a ultra-relativistic ( $\beta = \frac{v}{c} = 0.999$ )

bunch from a particle source on the top plate to an aligned particle sink on the bottom plate. The time signal of the EM power spectrum was calculated and recorded by a monitor placed within the resonator created by the defect. The result of the fast Fourier transform of the time signal of the power spectrum for frequencies up to 30 GHz is shown in figure 4.5. A wide spectrum of electromagnetic waves (Wakefields) was induced as the current bunch travelled through the defect region of the photonic crystal lattice.

In figure 4.5, the strength of individual EM states contributing to the power spectrum of the Wakefield tend to decrease depending on the duration after excitation when the FFT of the time signal was performed. Figure 4.5 (a), (b), and (c) are the FFT of the time signal taken after 300, 1000, and 3000 periods of the dipole mode at 12 GHz. The contributions of the LOM (10.905 GHz) and HOMs (14.95 GHz) to the power spectrum of the Wakefield in the defect region can be seen to reduce quickly with time because these EM states are not confined to the defect region but are allowed to propagate through the lattice to the surrounding PML boundary. The power of the confined dipole-like EM state also reduces but at a slower rate than the other undesirable propagating EM states. Considering that the losses in the dielectric and the metals were neglected in this case, the reduction in the strength of the dipole-like EM state was due to leakages at the boundary between the defect and the bulk lattice and to the surrounding PML boundaries. The results of figure 4.5

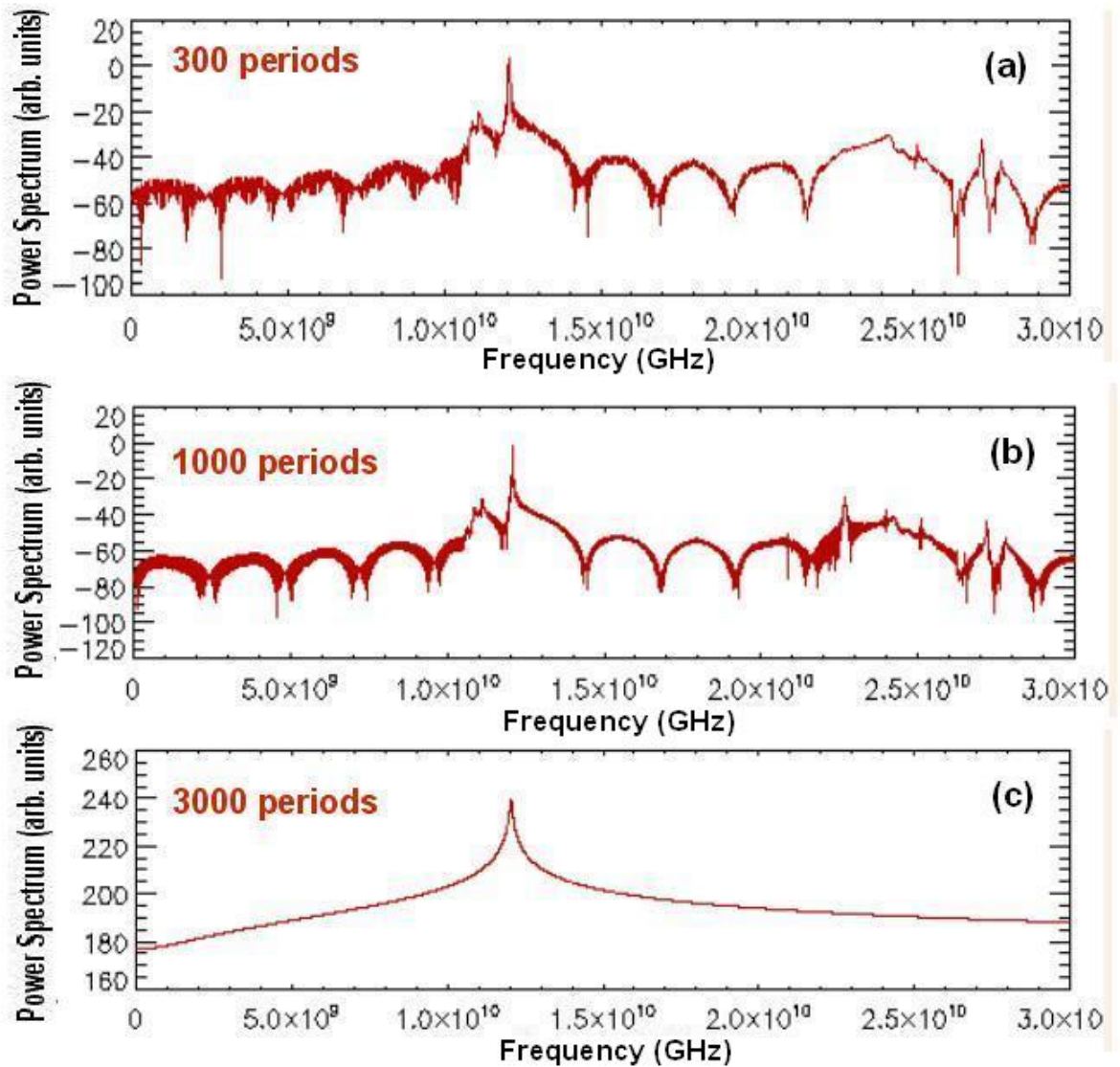


Figure 4.5: The Fast Fourier Transform of the time signal with (a) 300 periods, (b) 1000 periods and (c) 3000 periods of the field excited by a relativistic particle bunch travelling through the defect of the PBG structure in figure 4.4. The dipole mode at 12GHz is better confined than all other modes.

demonstrates that the lattice design of chapter 3 still can confine only the dipole-like EM state in a PBG crab cavity of finite height. In order to show that the lattice design is scalable and that the results of figure 4.5 are due to the lattice and are not artifacts of the software, a 9 GHz dipole cavity was modelled and presented in figure 4.6. The lattice parameters in this case are  $a=10.17$  mm,  $r=1.017$  mm,  $R=1.217$  mm and permittivity  $\varepsilon = 9.5$ .

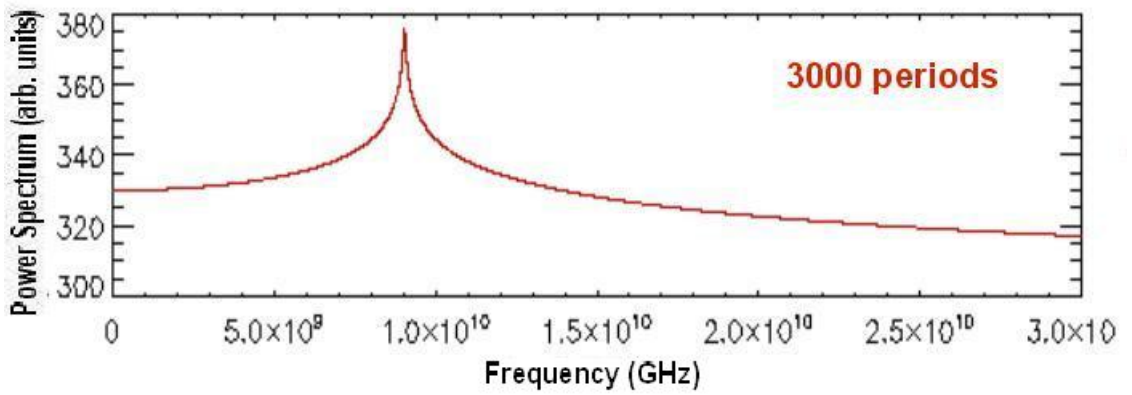


Figure 4.6: The Fast Fourier Transform of the time signal after 3000 periods of the field excited by a relativistic particle bunch travelling through the defect of the PBG structure in figure 4.4. The dipole mode at 9 GHz is better confined than all other modes.

#### 4.2.4 Analytical calculation of short range Wakefield in PBG crab cavity

PBG structures have been shown in section 4.2.3 to suppress long range Wakefield thereby minimizing particle bunch degrading effects on trailing bunches. However, when the bunch length is short and comparable to the wavelengths of the Wakefields, the effect of the Wakefields of an individual particle on another particle within the

same bunch but at a small distance  $s$  away becomes significant [172]. These type of Wakefields are called short range Wakefields and they are capable of increasing the energy spread and emittance of single bunch traveling through a RF cavity [173]. Although PBG structures do not offer any significant advantage towards limiting the effects of short range Wakefields, the dependence of short range Wakefields on the geometrical parameters of the cavity [173] suggest a parametric study of short range Wakes is useful for the design and optimization of the PBG crab cavity. Parametric studies have been performed for short range longitudinal [174, 175] and transverse [173, 176] Wakefields in conventional accelerating structures. The results of the analytical approach of calculating short range Wakefields presented in [173] for cylindrically symmetric structures was found to agree very well with numerical results for the parameter range  $0.35 \leq a_{bt}/L \leq 0.70$  where  $a_{bt}$  is the radius of the beam tube and  $L$  is the entire axial length of the single cell cavity. In this subsection, the analytical approach presented in [173] is adopted to parameterize the short range Wakefield in terms of the iris radius of the PBG structure. The analysis of the short range Wakefields of the PBG crab cavity is kept within the parameter range of validity stated in [173]. The expression of the high frequency longitudinal impedance of a perfectly conducting accelerating structure (in figure 4.7) is given in [173, 177, 178] as :-

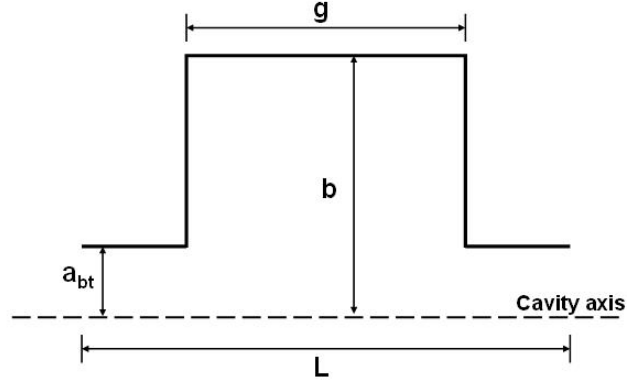


Figure 4.7: An illustration of the single cell cavity analysed in ref [173]

$$Z_L(k) = \frac{iZ_0}{\pi k a_{bt}^2} \left[ 1 + (1+i) \frac{L\alpha(\gamma)}{a_{bt}} \sqrt{\frac{\pi}{kg}} \right]^{-1} \quad (\text{for large } k) \quad (4.8)$$

$$\alpha(\gamma) \approx 1 - \alpha_1 \sqrt{\gamma} - (1 - 2\alpha_1)\gamma \quad (4.9)$$

Where  $Z_0 = 377\Omega$  and  $k = \frac{\omega}{c}$  are the free space impedance and wave number respectively.  $\alpha_1 = 0.4648$  is a fitted parameter from [173] and  $\gamma = \frac{g}{L}$ . The inverse Fourier transform of the longitudinal impedance  $Z_L$  of the cavity gives the longitudinal short range Wake function  $W_L$  as:-

$$W_L(s) \approx \frac{Z_0 c}{\pi a_{bt}^2} \phi(s) \exp\left(-\sqrt{\frac{s}{s_{00}}}\right) \quad (\text{for small } s) \quad (4.10)$$

$$s_{00} = \frac{g}{8} \left( \frac{a_{bt}}{L\alpha(\gamma)} \right)^2 \quad (4.11)$$

Where  $\phi(s)$  is a step function that satisfies the condition  $\phi(s) = 1$

for  $s > 0$ , and  $\phi(s) = 0$  for  $s < 0$ . The longitudinal Wakefield is dominated by monopole fields while the transverse Wakefield is dominated by the dipole fields [173]. The expression for the transverse Wake function is given in [173] as :-

$$W_x(s) = \frac{4Z_0cs_{00}}{\pi a_{bt}^4} \phi(s) \left[ 1 - \left( 1 + \sqrt{\frac{s}{s_{00}}} \right) \exp\left( - \sqrt{\frac{s}{s_{00}}} \right) \right] \quad (4.12)$$

Equations 4.10 and 4.12 were used to calculate the longitudinal and transverse short range Wake functions for PBG crab cavity respectively where  $L = 12.5\text{mm}$ ,  $g = 9.5\text{mm}$  and the value of the beam tube radius  $a_{bt}$  ranges from 0.4 mm to 0.6 mm. The plot of the Wake function against the axial separation distance  $s$  is shown in figure 4.8 and 4.9 below.

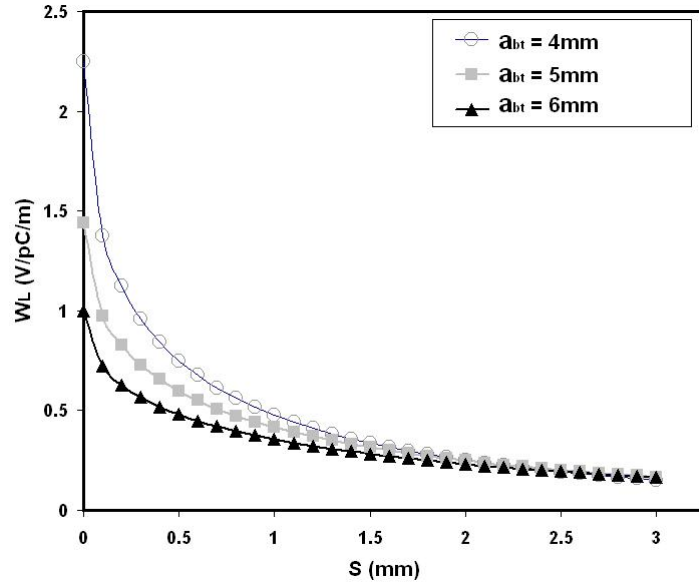


Figure 4.8: Plot of the analytically calculated short range longitudinal wake function for a 3mm long bunch traveling through a cavity with  $a_{bt} = 4\text{mm}$ , 5mm and 6mm.

Figure 4.8 shows that the value of the longitudinal wake function

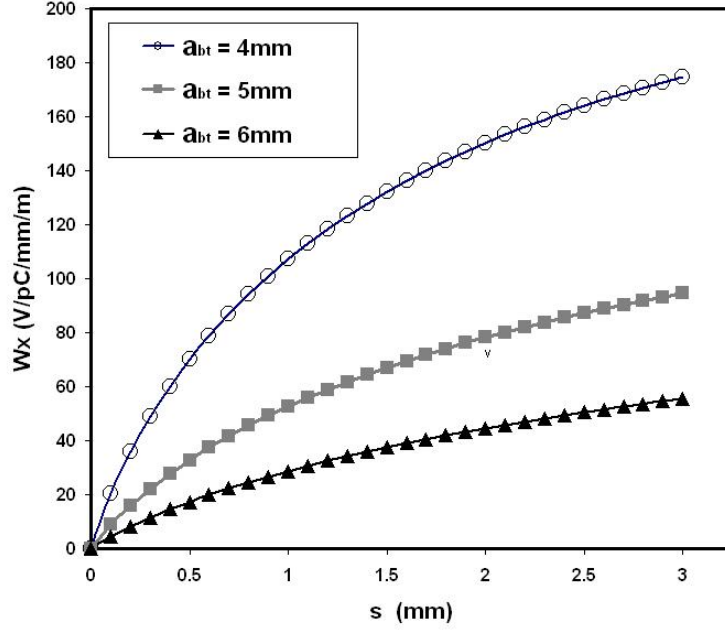


Figure 4.9: Plot of the analytically calculated short range transverse wake function for a 3mm long bunch traveling through a cavity with  $a_{bt} = 4\text{mm}$ , 5mm and 6mm.

decreases as the axial separation distance  $s$  increases between the constituent particles of a bunch. On the other hand in figure 4.9, the transverse wake function increases with larger values of  $s$ . The value of both longitudinal and transverse wake functions decreases with higher values of the beam tube radius. This study suggests that a PBG crab cavity with wider irises and beam tubes is preferred in order to minimized short range wakefields within the cavity.

#### 4.2.5 Convergence analysis of the HFSS simulation of a PBG crab cavity

Using the HFSS, realistic PC cavities with beam tubes (radius = 4 mm) and vacuum surroundings were modelled with different mesh resolutions to perform a convergence test. These PC cavities were modeled with lossy dielectric rods ( $\epsilon = 9.5$ , loss tangent = 0.0002),

copper plates and copper beam tubes. Convergence test are necessary in order to strike a balance between the accuracy of results and the computational resources and time required for a simulation. The adaptive meshing feature of HFSS was used where for any starting number mesh points, HFSS refines the mesh size after each run of the code until a set convergence condition is met. In this case a maximum tolerance of 2% variation in the eigenfrequency was set. Figure 4.10 shows that the frequency of the dipole mode oscillates about an average value of 11.9956 GHz as the mesh points were increased from 1000 to 400000. The standard deviation of the eigenfrequency was found to be 42.6 kHz (0.004%). The Q of the dipole mode was found to increase before oscillating about a stable value of  $\approx 19500$  as the number of mesh point is increased. This implies that the improvement in the accuracy of the results is small compared to the computational resources used as the starting mesh point is increased.

Also, the variation in the magnetic and electric field with increase in the mesh density is presented in figure 4.11. The peak magnetic field and electric fields can be seen to converge about  $4.0 \mu\text{A}/\text{m}$  and  $0.752 \text{ V}/\text{m}$  respectively. Furthermore, Figure 4.11 also indicates that the number of mesh points required for good approximation of the EM fields should be above 100000.

#### **4.2.6 Optimization of the PBG crab cavity**

As shown in [69] for conventional cavities, the iris and the beam tube dimensions have a strong effect on the figures of merits (frequency,

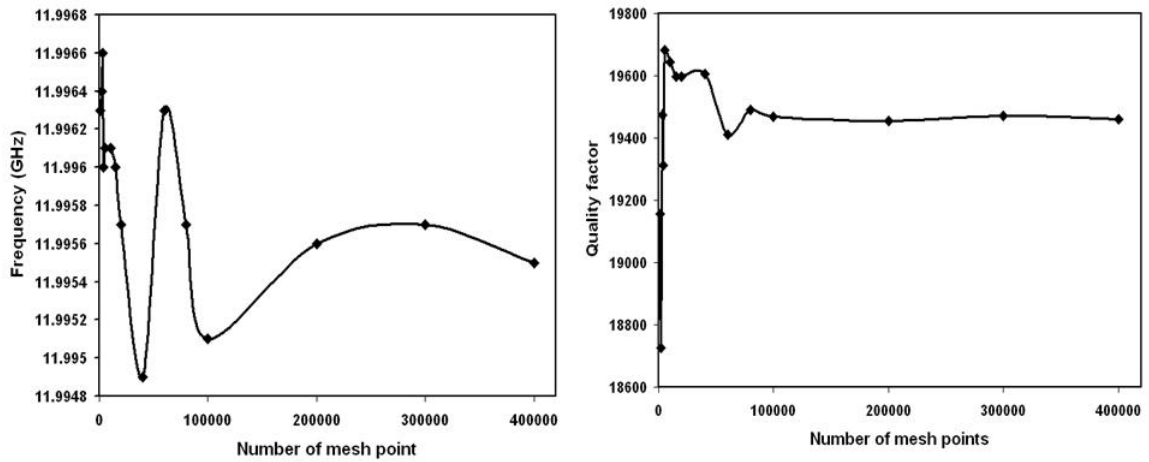


Figure 4.10: Convergence test result for HFSS simulation of a PBG crab cavity with beamtube radius (btr)= 4 mm, beamtube length (btl) = 10 mm, bulk lattice rod radius (r) = 1.189 mm and innermost rod radius (R) = 1.4885 mm. The variation in the dipole mode frequency and quality factor with increase in the number of mesh point solved is presented. Note that the HFSS adaptive mesh feature was used.

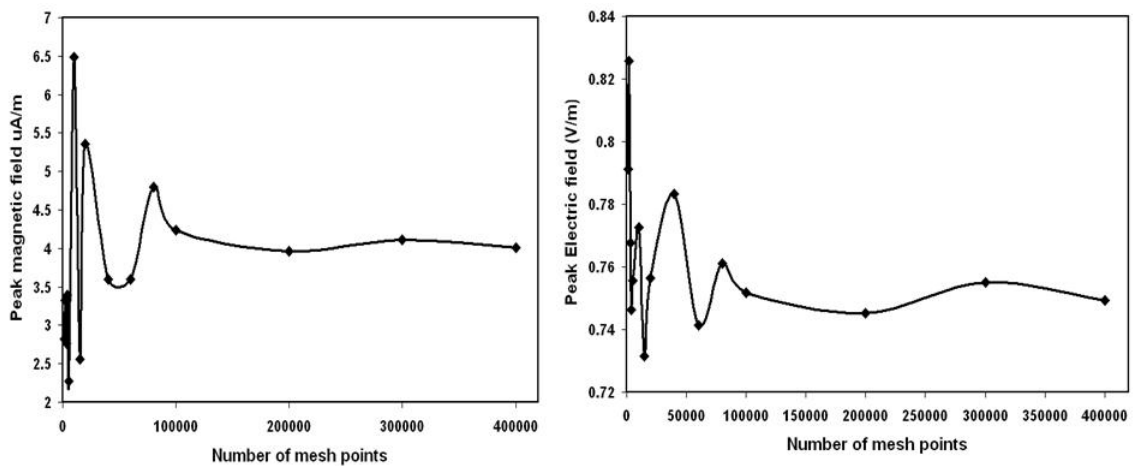


Figure 4.11: The effect of variation in the mesh density on (a) Peak electric field and (b) Peak magnetic field of the dipole mode at 11.9942 GHz.

$R/Q$ ,  $E_{\perp}/E_{peak}$ ,  $H_{peak}/E_{\perp}$ ) of a crab cavity. Following the approach of [69], the effect of the beam tube dimensions on the figures of merit of a PC crab cavity was investigated. In the case of a PBG structure, the introduction of the irises and the beam tubes can be considered as an extension of the defect region as they alter the local effective permittivity of the defect region. The presence of the beam tube causes the EM field of the confined mode to be redistributed and as a result altering the frequency and the parameters of merit of the confined EM state in the PBG structure. The introduction of two beam tubes (shown in figure 4.12) of radius 4 mm to either side of the crab cavity cause a frequency shift of -144.2 MHz (11.9942 GHz to 11.850 GHz).

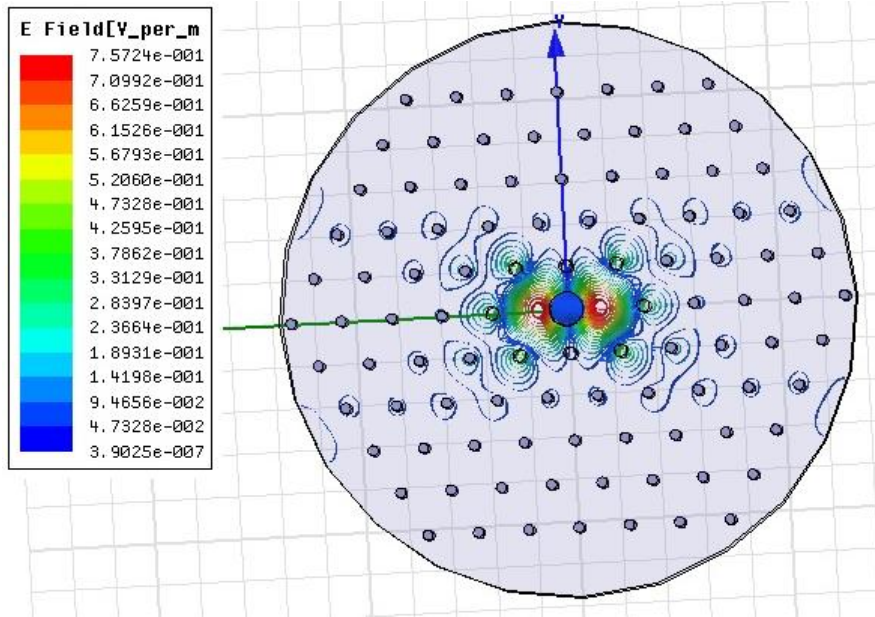


Figure 4.12: PBG crab cavity with the beam tube (radius = 4mm) introduced. The dipole mode has most of its field confined to the defect region of the PBG structure.

The extent of the frequency shift varies with the dimensions of the beam tube. The PC lattice needs to be optimized to correct this

frequency shift. This is important because the quality factor ( $Q$ ) of an EM states depend on the frequency of that state as follows [179]:-

$$Q = \frac{2\pi f_0 U_{mode}}{P} \quad (4.13)$$

Where  $U_{mode}$  is the stored energy of the mode,  $P$  is the power lost/dissipated and  $f_0$  is the resonant frequency. Figures 4.13, 4.14, 4.15 and Table 4.1 shows the frequency sensitivity of the dipole mode to the beam tube radius (btr), the beam tube length (btl), and the iris curvature radius (cc) respectively. A 1 mm increase in the radius and length of the beam tube caused a 48 MHz drop and 13.5 MHz increase in the frequency of the dipole mode respectively. Also an increase in the radius of the iris curvature by 1 mm gives a drop of 11.8 MHz in the frequency of the dipole mode. Compared to the conventional crab cavity in [69], the PBG crab cavity is less sensitive to variation in the cavity dimensions. This offers a less tight fabrication tolerance for the PBG crab cavity.

Table 4.1: Frequency sensitivity of the dipole photonic resonator.

Dimensions (mm)	Frequency sensitivity (MHz/mm)
btr	-48.2
btl	13.5
cc	-11.8

However, computer numeric control (CNC) machining can meet these fabrication tolerance requirements with accuracy up to a hundredth of a millimeter. For a beam tube length (btl=10 mm), the effect of varying the beam tube radius (btr) on the figures of merit

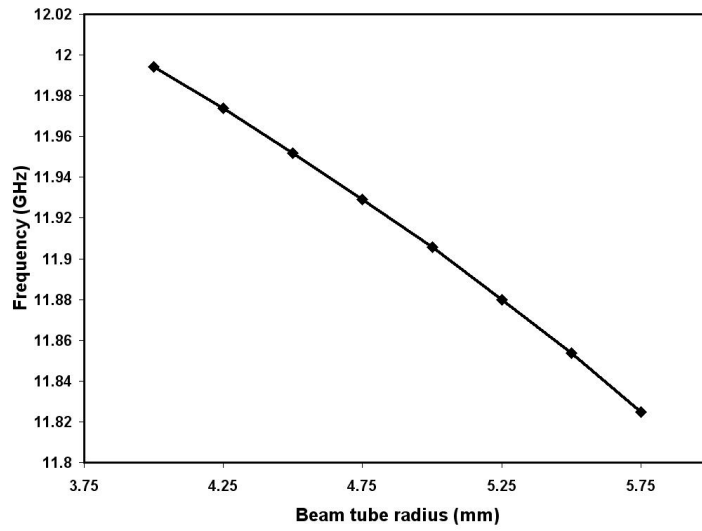


Figure 4.13: Frequency sensitivity of the dipole photonic resonator to variation in the beam tube radius.

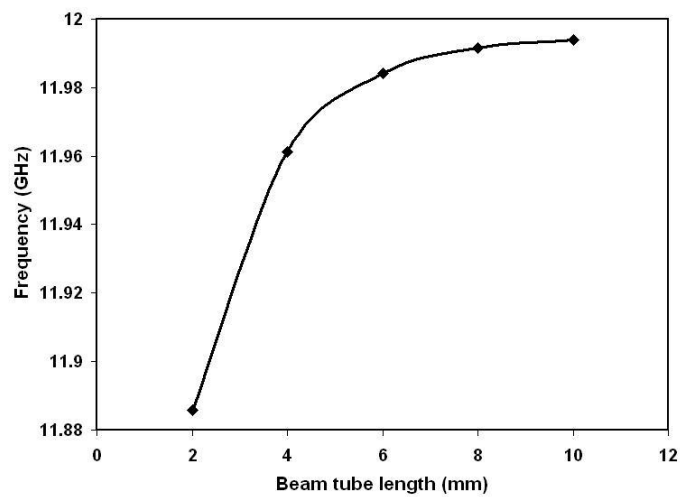


Figure 4.14: Frequency sensitivity of the dipole photonic resonator to variation in the beam tube length.

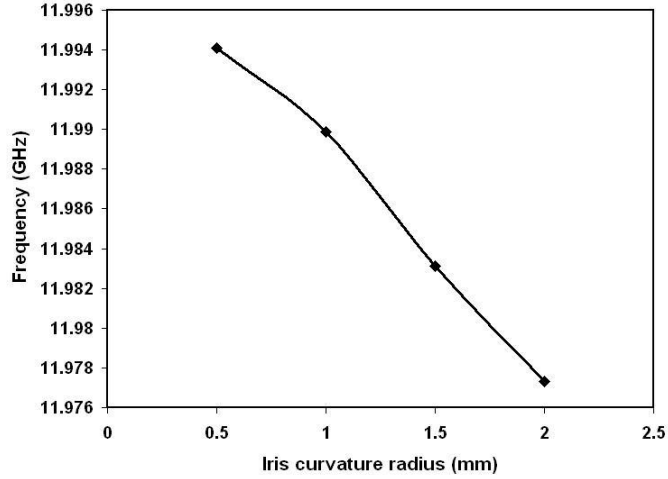


Figure 4.15: Frequency sensitivity of the dipole photonic resonator to variation in the iris curvature radius.

was investigated and the result are presented in figures 4.16, 4.17, and 4.18. The frequency shift caused by the variation in the beam tube radius was corrected in each case by optimizing the radius of the innermost rods so as to bring the frequency of the dipole mode back to 11.9942 GHz. The result of figures 4.16, 4.17, and 4.18 follow a similar pattern as those obtained in [69] with a decrease in  $R/Q$  and  $E_{\perp}/E_{peak}$  with increase in the beam tube radius. A wider beam tube increases the exposure of the electric field (which is totally internally reflected by the top and bottom plates) to the air region within the beam tube. This causes the longitudinal component of the electric field ( $E_z$ ) to decrease which in turn reduces the value of  $R/Q$  and  $E_{\perp}/E_{peak}$ . The values of  $R/Q$  in figure 4.16 are smaller than those published in figure 2 of [69] because the geometry studied is a single cell PC cavity with a long beam tube instead of the infinitely periodic travelling wave structure in [69]. As shown in [69] longer irises length causes a decrease in  $R/Q$  and  $E_{\perp}/E_{peak}$  of conventional

crab cavities. Also the quality factor of the dipole EM state in the dielectric PC resonators are higher than the Q values obtained for metallic pillbox cavities. This higher Q values in dielectric PC resonators results in a decrease in the R/Q values. On the other hand, the electric field ratio  $E_{\perp}/E_{peak}$  in figure 4.17 is comparable to those obtain in [69] for a cavity cell separation (iris length) of 7 mm. Figure 4.18 shows the effect of the beam tube radius on  $H_{peak}/E_{\perp}$ . The values of  $H_{peak}/E_{\perp}$  are comparable to those obtained in [69], however  $H_{peak}/E_{\perp}$  decreases with increase in the beam tube radius (btr) as both  $H_{peak}$  concentrated around the iris and  $E_{\perp}$  drop with increased beam tube radius.

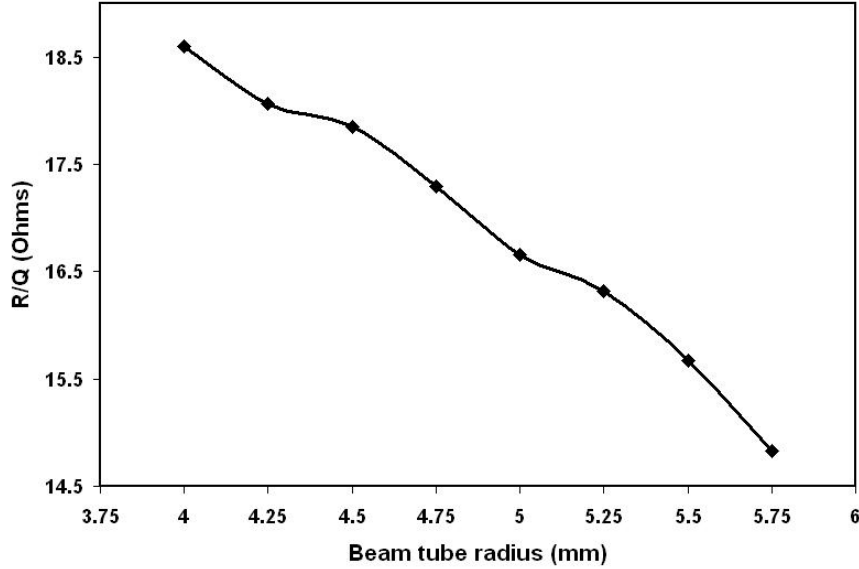


Figure 4.16: The effect of the beam tube radius (btr) on R/Q of the dipole mode at 11.9942 GHz.

In order to minimize the concentration of the magnetic field around the iris, a curvature of radius  $cc = 1mm$  was introduced to the iris. This resulted in a frequency shift of -389MHz for a beam tube radius of 5 mm. Again, the frequency shift was corrected by tuning the

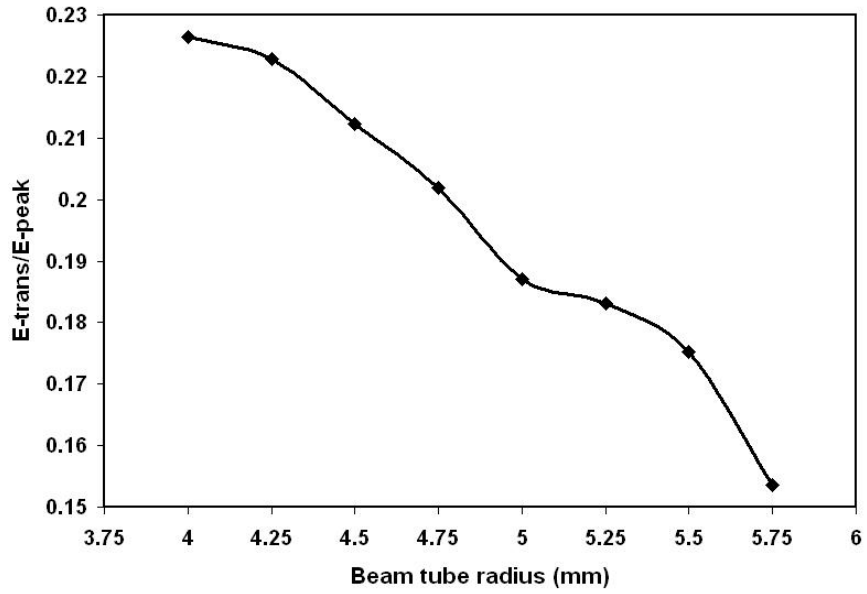


Figure 4.17: The effect of the beam tube radius (btr) on  $E_{\perp}/E_{peak}$  of the dipole mode at 11.9942 GHz.

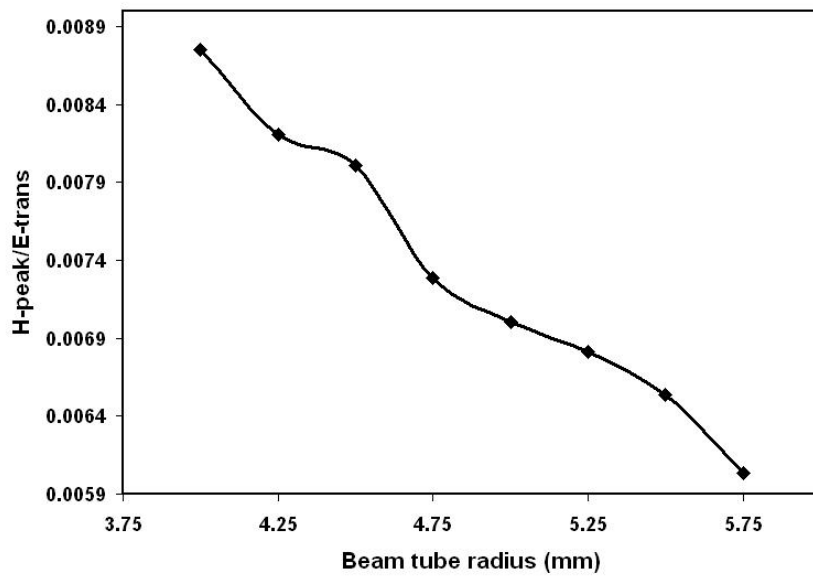


Figure 4.18: The effect of the beam tube radius (btr) on  $H_{peak}/E_{\perp}$  of the dipole mode at 11.9942 GHz.

radius (1.401mm) of the innermost rods closest to the defect. Also, the iris curvature caused a small increase of 1% in the quality factor of the dipole mode.

#### 4.2.7 Final single-cell Design Parameters

In this section the final design parameter of the single cell PC crab cavity is presented. Table 4.2 shows the dimensions of the final cavity design while table 4.3 gives the parameters of merit of the cavity. Also, figures 4.19 and 4.20 compare the  $E_z$  component of the electric field along the z-axis and x-axis respectively of a PBG crab cavity to those obtained from a pillbox cavity. Since the electric field strength depends on the power of the EM source driving the structure, the electric field of both the pillbox and the PBG crab cavities was normalized to 1W. The field seen by a particle bunch travelling through the PBG crab cavity compares very well with those obtained in the pillbox designs. However, the PBG design offers the additional benefit of wakefield suppression which is not intrinsic in the pillbox design.

Table 4.2: The dimensions of the PBG crab cavity.

Cavity length	12.5	mm
Lattice constant (a)	11.89	mm
Bulk rod radius (r)	1.189	mm
Innermost rod radius (R)	1.4	mm
Beam tube radius (btr)	5	mm
Iris curvature radius (cc)	1	mm
Beam tube length (btl)	10	mm
Phase Advance	180	Degrees

Table 4.3: The parameters of merit of the PBG crab cavity.

Frequency	11.9942	$GHz$
R/Q	16.7	$\Omega$
$Q_0$	18925	
Deflecting gradient ( $E_{\perp}$ )	63.6	$KV/m$
Transverse Voltage ( $V_{\perp}$ )	795	$V$
Input power	1	$Watt$
$E_{\perp}/E_{peak}$	0.187	
$H_{peak}/E_{\perp}$	0.007	$A/V$

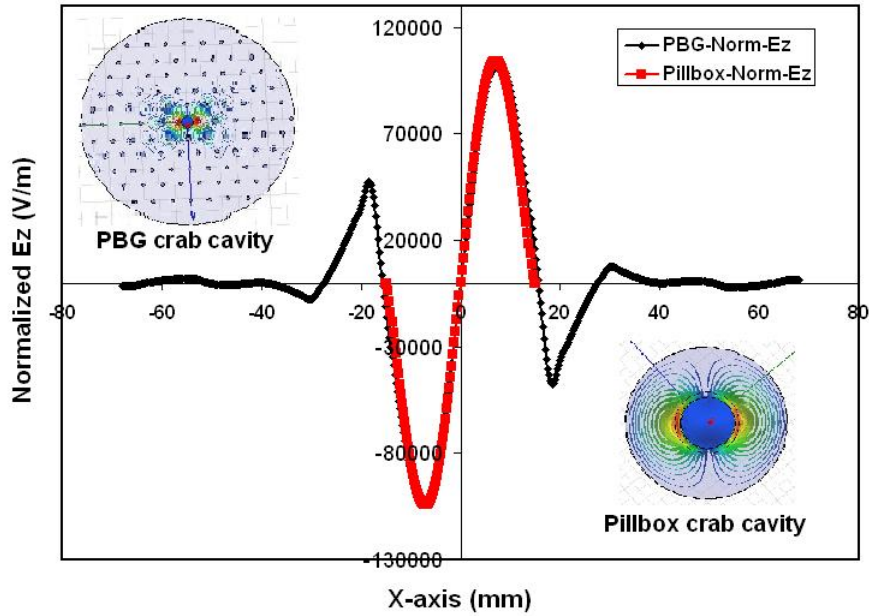


Figure 4.19: The Z-component of the electric field along the transverse X-axis for PBG crab cavity is compared to the equivalent values obtained for the pillbox crab cavity. The values of Ez in the two cavities was normalized to 1Watt input power.

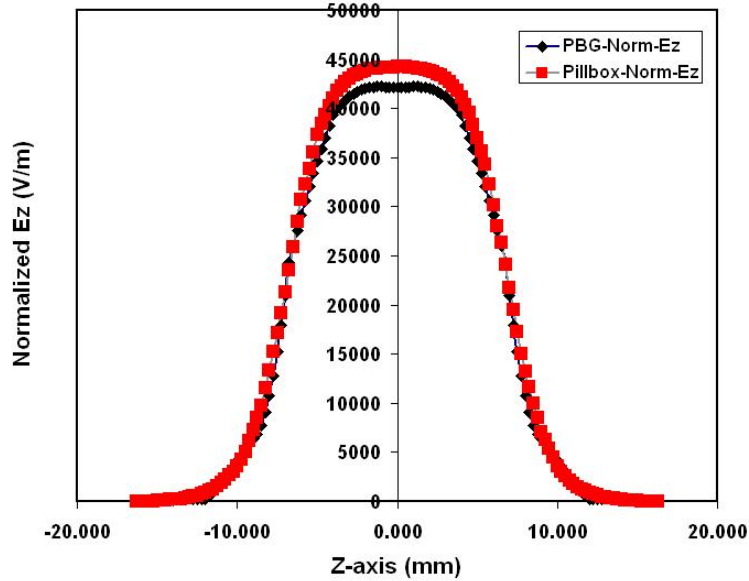


Figure 4.20: The Z-component of the electric field along a parallel longitudinal line which is 2 mm away from the Z-axis of the PBG crab cavity is compared to the equivalent values obtained for the pillbox crab cavity. The values of  $E_z$  in the two cavities was normalized to 1W input power.

### 4.3 Coupling of EM power into a PC crab cavity

This section discusses the transfer (coupling) of EM power into the PC resonator from an external RF source. The aim is to couple as much of the EM power as possible from the RF source to the dipole mode with very little power coupled to other modes and with minimum reflection back to the external RF source. This section presents two different methods of coupling EM power into the cavity resonator. The first method explored the coupling of EM power from a coaxial wire, via a stub antenna, into the PC resonant cavity. This coupling approach is suitable for the cold testing of the PBG crab cavity in the laboratory. However the high power associated with the hot testing and regular operation of the PBG crab cavity demands an alternative coupling approach because the high power will

damage the stub antenna. In the second coupling method, the coaxial line is replaced by a rectangular waveguide where the *door-knob* transition (discussed in [179]) was adopted to couple EM power from the waveguide into the PC resonant cavity. Detailed description of the two EM coupling scheme are presented in subsections 4.3.1 and 4.3.2 below.

### 4.3.1 Coupling of EM power from a coaxial wire

This coupling scheme was implemented by inserting a dipole antenna into the top plate of the PC resonator at the position shown in figure 4.21. The dipole antenna is connected to an EM wave port via a coaxial line. The EM power from the RF source travels through the coaxial line and is then radiated by the antenna within the PBG crab cavity. The position of the antenna was chosen to be close enough to the point of the peak electric field of the dipole mode in order to allow for a good coupling. On the other hand, the antenna was kept away from the peak field position in order to minimize any perturbation of the electric field of the dipole mode.

The presence of the antenna in the PBG structure has a capacitive effect and the length of the antenna controls the strength of the coupling. By varying the length of the antenna with the PC lattice, an optimum impedance matching can be achieved between the coaxial line and the double point defect of the PBG structure. Using the HFSS setup in figure 4.21, the depth of the antenna within the PC resonator was set to 7 mm and the reflection coefficient  $S_{11}$  was

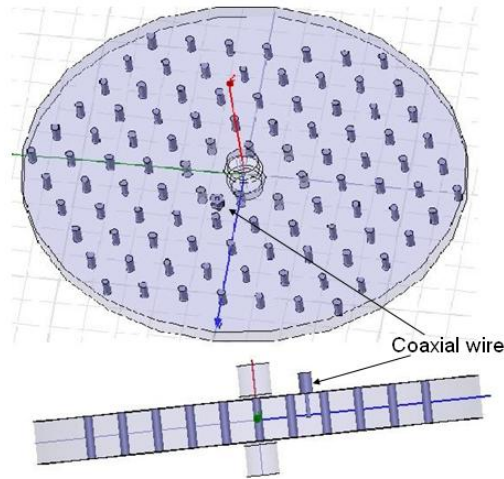


Figure 4.21: The image of the PBG resonator with an antenna positioned to couple EM power into the structure.

calculated at the port defined outside the cavity. The introduction of the antenna (radius=1.2 mm) caused a frequency shift of -517 MHz which was corrected by optimizing the lattice dimension (radius of innermost rods). Figure 4.22 shows the scattering parameter  $S_{11}$  for a PC dipole resonator with beam tube radius of 5 mm and iris curvature of 1 mm. A near critical coupling was achieved with  $S_{11} = 0.045$  at 11.99425 GHz.

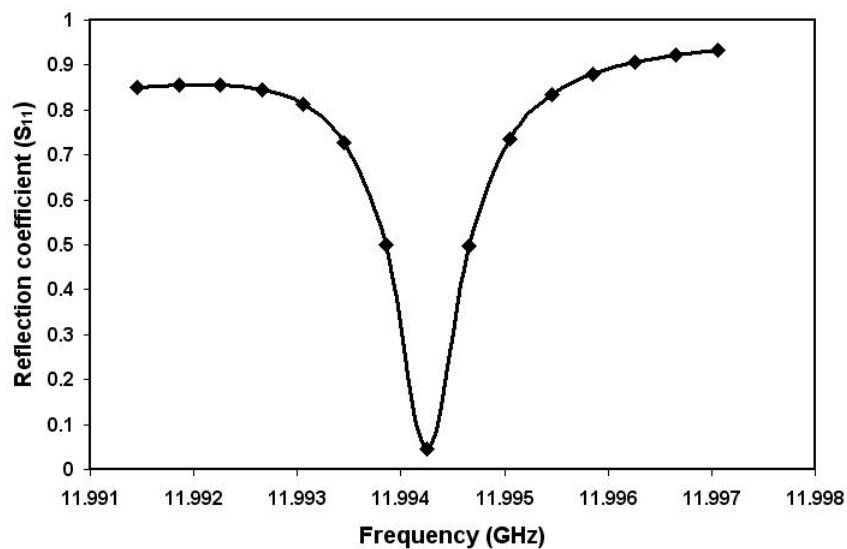


Figure 4.22: The reflection coefficient  $S_{11}$  of the dipole mode at 11.99425 GHz. 95.5% of the power from the antenna is stored in the PBG structure.

### 4.3.2 Coupling of EM power from a waveguide

This coupling scheme involves two transitional stages. In the first stage, EM power is coupled from a waveguide, via a coupling iris, into a single point defect in the PC lattice. The second stage involves the coupling of the EM power from the single point defect to the double point defect. This coupling scheme is shown in figure 4.23.

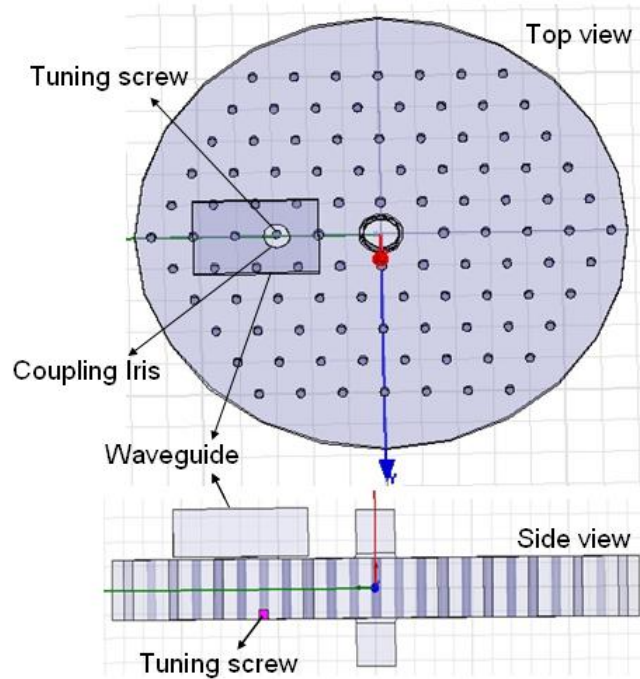


Figure 4.23: The image of the PBG resonator with a waveguide coupling scheme.

The EM wave propagation through the waveguide (shorted at one end) sees a discontinuity presented by the iris which alters both the electric and magnetic field line of its  $TE_{010}$  mode. The electric field of the waveguide's  $TE_{010}$  mode is perpendicular to the plane of the coupling iris while the magnetic field, rotating around the electric field, is parallel to the plane of the coupling iris. Although the height of the iris is small, it can be considered as a cylindrical waveguide. The

magnetic field of the  $TM_{010}$  mode of the cylindrical waveguide rotates in a plane parallel to the magnetic field of the  $TE_{010}$  mode of the waveguide. These indicate that the magnetic fields of these two modes are well matched. On the other hand, the electric fields of both modes are not well matched and will be redistributed at the discontinuity presented by the iris [179]. Furthermore, the magnetic field of the  $TM_{010}$  mode in the iris is well matched to the magnetic field of the fundamental  $TM_{010}$ -like EM state in the point defect. However, the electric field of the  $TM_{010}$ -like EM state is perturbed by boundary condition presented by the removal of part of the top metallic plate. As shown in [179], this type of iris coupling is both capacitive (displacement current) and inductive (conduction current). The strength of the coupling of the EM power between the waveguide and the point defect can be controlled by varying the dimensions (radius and/or height) of the iris. The second stage of this coupling scheme involves the matching of the impedance of the single point defect to the impedance of the double point defect. This was done by placing a capacitive tuning screw at the centre of the single point defect in order to vary its impedance until it is matched to the impedance of the double point defect. The strength of the coupling between the single and double point defects can be controlled by varying the height of the tuning screw. The tuning screw also perturbs the  $TM_{010}$ -like EM state of the single point defect and does not allow the sharing of the EM power from the RF source between the  $TM_{010}$ -like mode in

the single point defect and the  $TM_{110}$ -like dipole mode in the double point defect. A careful selection of an optimized combination of the iris radius and the length of the screw can minimize the impedance mismatch in the entire system. This will allow most of the EM power to be coupled to the dipole-like EM state in the double point defect.

This coupling scheme was implemented numerically by setting up a HFSS simulation as shown in figure 4.23 and the scattering parameter  $S_{11}$  was calculated at the RF source. The introduction of the waveguide, the coupling iris, and the single point defect to the previous HFSS setup (in table 4.2) caused a frequency shift of -19.8MHz (11.9942 GHz to 11.9744 GHz). This result was obtained when the coupling iris radius and the tuning screw length was set to 4 mm and 3 mm respectively. This shift in frequency was corrected by changing the lattice constant from 11.89 mm to 11.52 mm as the impedance matching method described above is not suitable for broadband impedance matching [179]. The  $r/a$  and  $R/a$  ratios of the lattice were kept the same at 0.1 and 0.125 respectively. This brings the resonant frequency of the dipole mode to 11.993 GHz which is closer to the target frequency of 11.9942 GHz. An increase in the radius of the coupling iris causes the frequency of the dipole mode in the double defect to decrease. Also a reduction in the length of the tuning screw causes an increase in the frequency of the dipole mode. These two effects can be explained by looking at the relationship  $\omega_0 = \frac{1}{\sqrt{LC}}$  between the eigenfrequency  $\omega_0$  and the capacitance  $C$  and

inductance  $L$  in the equivalent RLC circuit in figure 4.24 where  $Z_w$ ,  $Z_P$  and  $Z_D$  are the impedance of the waveguide, the point defect and the double-point defect respectively. The iris and the tuning screw are indicated by  $i$  and  $s$  while  $C$  and  $L$  are the associated capacitance and inductance respectively.

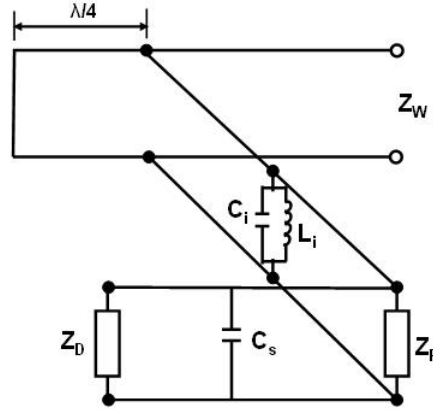


Figure 4.24: The equivalent circuit of the coupling scheme to transfer microwave power from a waveguide to the double point defect.  $Z_w$ ,  $Z_P$  and  $Z_D$  are the impedance of the waveguide, the point defect and the double-point defect respectively. The iris and the tuning screw are indicated by  $i$  and  $s$  while  $C$  and  $L$  are the associated capacitance and inductance respectively.

The increase in the radius of the coupling iris and the reduction in the length of the tuning screw both have the effect of reducing the capacitance which results in a reduction in the value of the eigenfrequency. An extensive optimization of the combined effect of coupling iris and tuning screw found that a near critical coupling can be achieved when the radius of the coupling iris is 3.69 mm and the tuning screw is 0.9 mm. All other parameters were kept the same with lattice constant  $a = 11.52\text{mm}$ , bulk lattice rod radius  $r = 1.152\text{mm}$ , innermost rod radius  $R = 1.33\text{mm}$  and the cavity height  $d = 12.5\text{mm}$ . The resulting scattering parameter  $S_{11}$  calcu-

lated using HFSS is shown in figure 4.25.

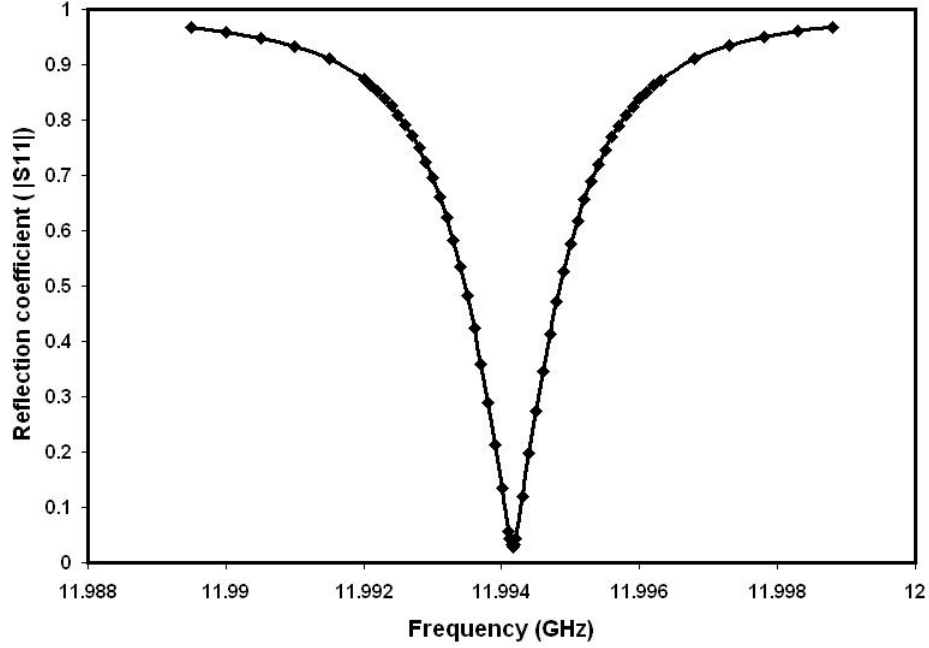


Figure 4.25: The reflection coefficient  $S_{11}$  of the dipole mode at 11.9942GHz. 97.21% of the EM power from the waveguide is coupled to the dipole mode in the double point defect of the PBG structure.

In figure 4.25, the  $S_{11}$  value at 11.9942 GHz is 0.0279. This indicates that more than 97% of the EM power sent from the RF source is coupled to the  $TM_{110}$ -like dipole mode confined to the double point defect. The strength of the coupling is shown in figure 4.26 where the  $S_{11}$  plot is very close to the centre point of the Smith chart that indicate critical coupling. The loaded quality factor  $Q_L$  was estimated from the ratio of the resonant frequency  $f_0$  to the bandwidth ( $f_2 - f_1$ ) at the  $-3dB$  point indicated by markers m2 and m3 on the polar plot in figure 4.26.

$$Q_L = \frac{f_0}{f_2 - f_1} = \frac{11.9942GHz}{11.9952GHz - 11.9930GHz} = 5452 \quad (4.14)$$

The field profile of the excited dipole EM state at 11.9942 GHz is shown in figure 4.27.

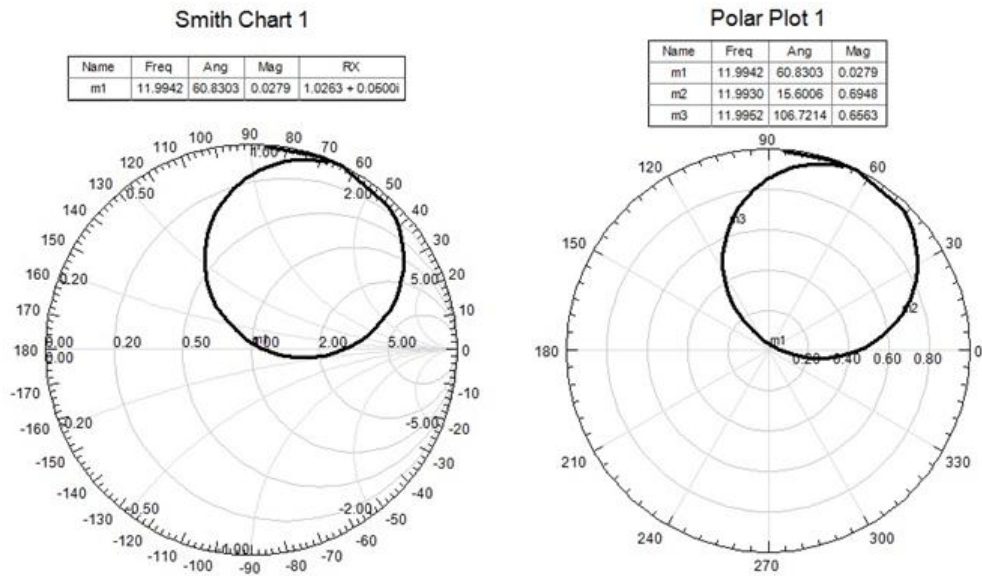


Figure 4.26: Smith chart and polar plot of the reflection coefficient  $S_{11}$  for the waveguide coupling of EM power to the dipole mode at 11.9942 GHz (marker: m1). A near critical coupling was achieved with markers m2 and m3 indicating the -3dB points on the polar plot on the right.

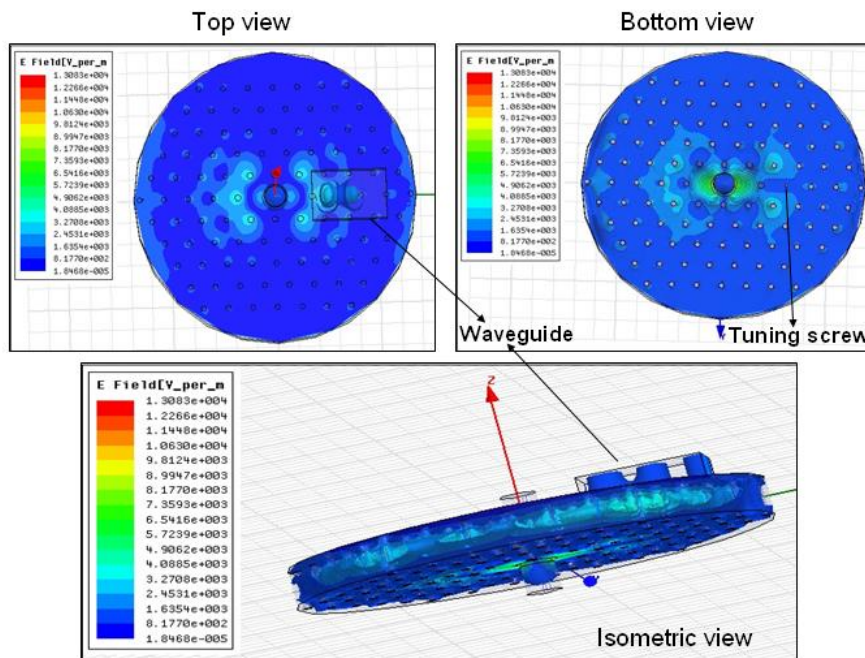


Figure 4.27: The distribution of the electric field of the dipole mode at 11.9942 GHz when EM power is coupled from a waveguide.

## 4.4 High Power application of Final Design Parameters

So far in this work, the benefit of using a PBG structure for crabbing applications has been demonstrated with the selective confinement of the dipole mode. On the other hand, this design like other resonant cavities used in high energy particle accelerators is susceptible to breakdown in the dielectric rods as well as the metallic plates [180]. Breakdown is the sudden drop in the electrical resistance of a material when it is exposed to an electric field with intensity beyond a critical value referred to here as the breakdown value. When this critical value is exceeded, a conduction path with high current density is formed in the material. The Joule heating generated by the sudden increase in the current density can lead to destructive effects such as melting or cracking of the material [181]. This section investigates how the performance of a single-cell PBG crab cavity is limited by breakdown. Also in this section, the performance of a multi-cell PBG crab cavity is calculated with consideration given to the breakdown value of the dielectric scatterers.

### 4.4.1 A single-cell PBG crab cavity for CLIC

The alumina rods closest to the defect region are exposed to higher magnitudes of electric field than those that make up the bulk lattice. This can be seen from the electric field distribution  $E_z$  along the X-axis given in figure 4.28 for the single-cell PBG crab cavity.

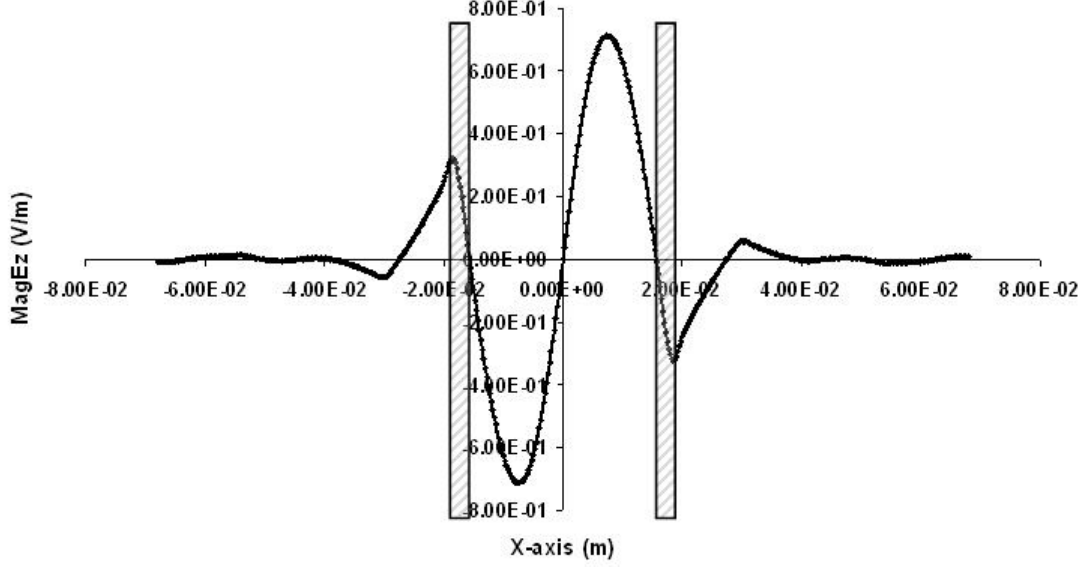


Figure 4.28: The Z-component of the electric field along the transverse X-axis of a single-cell PBG crab cavity. The position of the innermost rods along the X-axis are shown.

Considering that the DC breakdown value for alumina ( $\epsilon = 9.5$ ) is 13.4 MV/m [182], it is important to keep the electric field  $E_{inner}$  on the innermost alumina rod lower than this value. As stated in [69], the CLIC facility requires a crab cavity with a maximum transverse kick voltage  $V_{\perp}$  of 2.4 MV to give a beam with energy  $U_{beam} = 1.5 TeV$  a crossing angle of  $\theta_c = 20 \text{ mrad}$ . This was calculated from equation 4.6 as follows:

$$V_{\perp} = \frac{\theta_c U_{beam} c}{2\omega R_{12}} = \frac{(20 \times 10^{-3}) \times (1.5 \times 10^{12}) \times (2.9979245 \times 10^8)}{2 \times (2 \times \pi \times 11.9942 \times 10^9) \times 25} = 2.4 MV \quad (4.15)$$

In order to deliver the 2.4 MV of kick required by CLIC from a single cell PBG crab cavity of length  $d = 0.0325 \text{ m}$ , the cavity must have a transverse gradient  $E_{\perp}$  given as :-

$$E_{\perp} = \frac{V_{\perp}}{d} = \frac{2.4 \times 10^6}{0.0325} = 73.84 MV/m \quad (4.16)$$

The parameter of merit  $E_{\perp}/E_{peak}$  depends on the the cavity design and remains constant for any given design. For the single-cell PBG crab cavity with  $E_{\perp}/E_{peak} = 0.149$ , the peak electric field is calculated as:

$$E_{peak} = \frac{73.84}{0.149} = 495.6 MV/m \quad (4.17)$$

Considering the electric field distribution  $E_z$  along the X-axis given in figure 4.28 for the single-cell PBG crab cavity, the ratio of electric field  $E_{inner}$  in the innermost rods to the peak electric field  $E_{peak}$  is also constant and given as  $E_{inner}/E_{peak} = 0.386$ . Therefore  $E_{inner}$  is calculated as:

$$E_{inner} = E_{peak} \times 0.386 = 495.6 \times 0.386 = 191.3 MV/m \quad (4.18)$$

Although the value of  $E_{inner}$  (191.3MV/m) is higher than the DC breakdown value (13.4MV/m) for alumina, the field  $E_{inner}$  in the PBG crab cavity oscillate with time and the dielectric rods are exposed to the high value of  $E_{inner}$  only once in every 0.0834ns (period of the dipole mode). However, based on the DC breakdown value for alumina, the single cell PBG crab cavity designed in this chapter cannot be used to deliver the 2.4 MV transverse kick required by

CLIC. On the other hand, the single-cell PBG crab cavity can serve as a starting platform on which a multi-cell crabbing solution can be developed. Also, the single-cell dipole PBG cavity can be used in high power applications where the transverse kick requirement is much lower than that of CLIC.

In order to determine the limit of the transverse kick voltage that can be delivered by this single-cell design of PBG crab cavity, the DC breakdown value of 13.4 MV/m is assigned to  $E_{inner}$  and the transverse gradient as well as the maximum transverse kick is calculated as :-

$$E_{peak} = \frac{E_{inner}}{0.386} = \frac{13.4 \times 10^6}{0.386} = 34.7 MV/m \quad (4.19)$$

$$E_{\perp} = E_{peak} \times 0.149 = 34.7 \times 10^6 \times 0.149 = 5.17 MV/m \quad (4.20)$$

The maximum transverse kick that can be delivered is calculated as:

$$V_{\perp} = E_{\perp} \times d = 5.17 \times 10^6 \times 0.0325 = 168 KV \quad (4.21)$$

This single-cell crab cavity can be safely used for applications that requires a transverse kick that is less than 168 KV. In order to meet the transverse kick requirement for CLIC, a different design of PBG crab cavity is needed. One of the design options is a multi-cell PBG

crab cavity with higher longitudinal drift distance  $d$  which reduces the transverse gradient of the structure. This multi-cell approach is considered in the next subsection.

#### **4.4.2 A multi-cell PBG crab cavity for CLIC**

The multi-cell PBG crab cavity is investigated by considering two design scenarios. In the first scenario, the design is based on the assumption that when several single-cell PBG crab cavities are cascaded together (iris to iris), the performance of each single-cell is retained in a multi-cell design. This assumption allows for the extrapolation of the performance of a multi-cell PBG crab cavity from those of a single-cell crab cavity. In the second scenario, the performance of a finite size multi-cell PBG crab cavity is extrapolated from an infinitely long multi-cell PBG crab cavity. In this case the cell-to-cell coupling and the  $\pi$  phase advance between the cells are considered in the HFSS simulation. The two design scenarios outlined above are necessitated by the unavailability of huge computational resources required to directly simulate large geometrical structures using HFSS.

##### **Scenario 1: The cascading of single-cell PBG crab cavities**

In this scenario, an assumption is made that a multi-cell PBG crab cavity can be made by cascading several single-cell PBG crab cavities where the parameters of merit of the single-cell structure is retained in the multi-cell cavity design.

For the purpose of calculating the maximum transverse gradient  $E_{\perp}$  that can be delivered by this multi-cell PBG crab cavity design without damaging the alumina rods, 90% of the DC breakdown value (13.4 MV/m) for alumina is assigned to  $E_{inner}$  (i.e 12.06 MV/m). From the electric field distribution  $E_z$  along the X-axis in figure 4.28, the ratio of electric field  $E_{inner}$  in the innermost rods to the peak electric field  $E_{peak}$  is constant and given as  $E_{inner}/E_{peak} = 0.386$ . Therefore the  $E_{peak}$  is calculated as:

$$E_{peak} = \frac{E_{inner}}{0.386} = \frac{12.06 \times 10^6}{0.386} = 31.24 MV/m \quad (4.22)$$

The parameter of merit  $E_{\perp}/E_{peak}$  depends on the the cavity design and remains constant for any given design. For the single-cell PBG crab cavity with  $E_{\perp}/E_{peak} = 0.149$  (shown in table 4.3), the maximum transverse gradient  $E_{\perp}$  that can be delivered is calculated as:

$$E_{\perp} = E_{peak} \times 0.149 = 31.24 \times 10^6 \times 0.149 = 4.66 MV/m \quad (4.23)$$

In order to deliver the 2.4 MV of transverse kick required by CLIC from a crab cavity with transverse gradient  $E_{\perp}$  of 4.66 MV/m, the cavity must have a longitudinal length  $d$  given as :-

$$d = \frac{V_{\perp}}{E_{\perp}} = \frac{2.4}{4.66} = 0.515m \quad (4.24)$$

In order to meet the requirement of a longitudinal length of 0.515 m, a multicell PBG crab cavity design is needed. Based on the assumption stated above and using only the active (distance between the copper plates) longitudinal length  $d'$  of 0.0125 m, the number of cells  $N$  required for the multicell design is calculated as:

$$N = \frac{d}{d'} = \frac{0.515}{0.0125} = 41\text{cells} \quad (4.25)$$

Scenario 1 suggest that a 51.5 cm long, 41 cell PBG crab cavity will deliver the 2.4 MV transverse kick required by CLIC while avoiding breakdown in the dielectric rods.

#### **Scenario 2: An infinitely long multi-cell PBG crab cavity**

In this scenario, an infinitely long periodic multi-cell PBG dipole cavity is investigated in order to extrapolate the performance of a long multi-cell PBG crab cavity. In this case, the dielectric rods are sandwiched in-between two copper disk plates. Each disk plate of a cell has an iris that allows it to couple to adjacent cells. The infinitely periodic PBG crab cavity was implemented by applying the HFSS periodic boundary condition on both irises of the single-cell structure shown in figure 4.29.

In figure 4.29,  $R_c$  is the outer radius of each cell,  $r_b$  is the radius of the iris,  $cc$  is the radius of the iris curvature and  $d'$  is the cavity length (cavity+iris) which is determined by the phase advance per cell  $\phi_c = \frac{k_{RF}}{d} = \pi \cdot k_{RF}$  is the free space phase constant in radians/meter. The

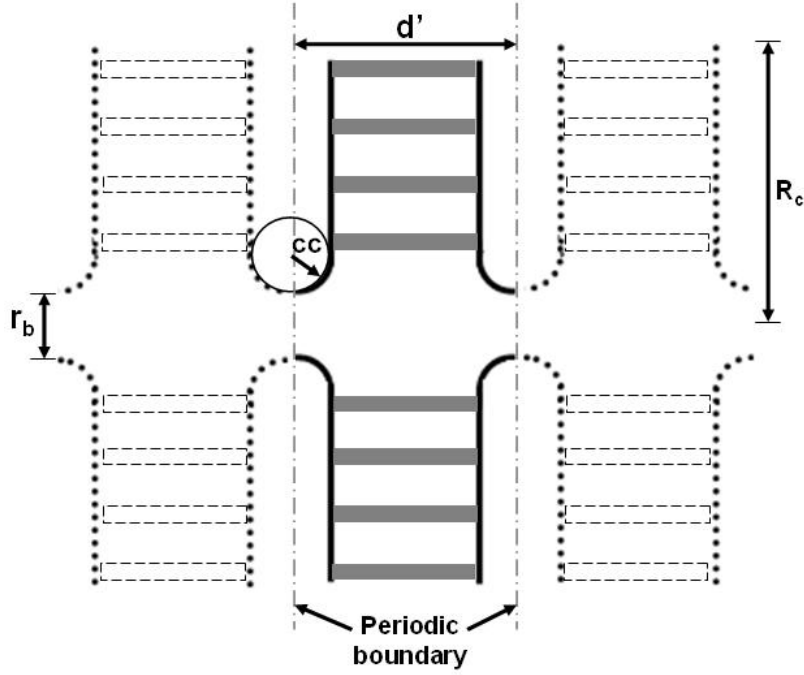


Figure 4.29: An infinitely periodic PBG resonating cavity.  $cc$  is the radius of the iris curvature while  $d'$  is the cavity length (cavity + iris).

approach used in [69], where the iris is curved to avoid surface field enhancement and field emissions was adopted in this scenario. The radius of the iris curvature was optimized by investigating the effect of variations in the iris curvature  $cc$  on the parameters of merit ( $R/Q$ ,  $E_{\perp}/E_{peak}$ ,  $H_{peak}/E_{\perp}$ ). For each case of iris curvature  $cc$ ,  $r_b = 5\text{mm}$ ,  $d' = 12.5\text{mm}$  and  $R_c = 68\text{mm}$ . The lattice dimension (radius of the innermost rods) was varied to keep the frequency of the dipole-like EM state fixed at 11.9942 GHz. Figures 4.30, 4.31 and 4.32 shows the effect of variations in  $cc$  on  $R/Q$ ,  $E_{\perp}/E_{peak}$ , and  $H_{peak}/E_{\perp}$  respectively.

As pointed out in [69], it is desirable for a crab cavity design to have a higher value of  $E_{\perp}/E_{peak}$  while keeping  $H_{peak}/E_{\perp}$  as low as possible. This is important in order to minimize the surface fields of

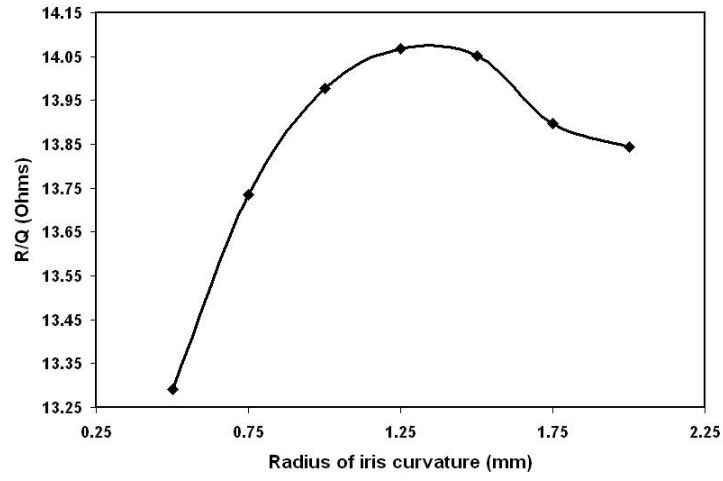


Figure 4.30: The effect of variation in the radius of the iris curvature  $cc$  on the  $R/Q$  of the dipole-like EM state. This result is for an infinitely periodic PBG crab cavity.

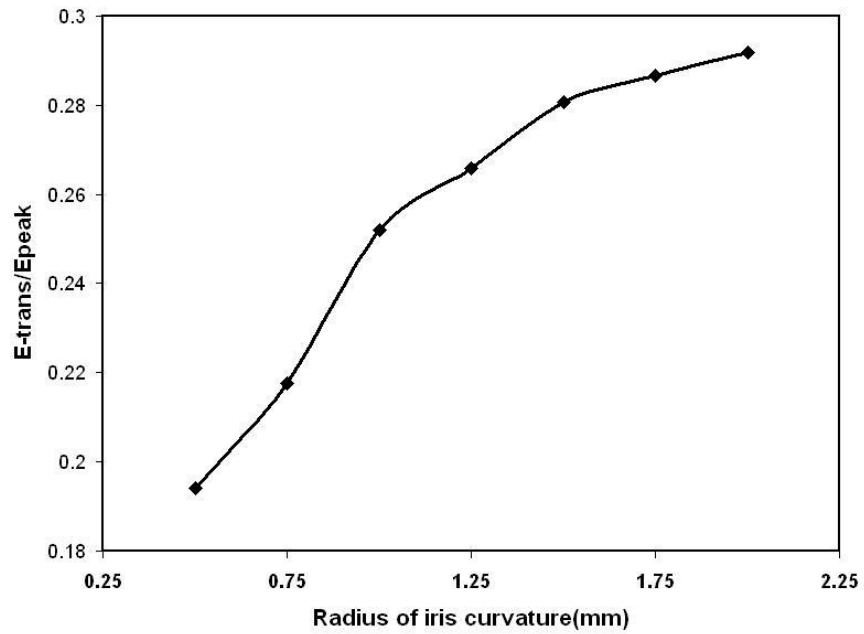


Figure 4.31: The effect of variation in the radius of the iris curvature  $cc$  on the  $E_{\perp}/E_{peak}$  of the dipole-like EM state. This result is for an infinitely periodic PBG crab cavity.

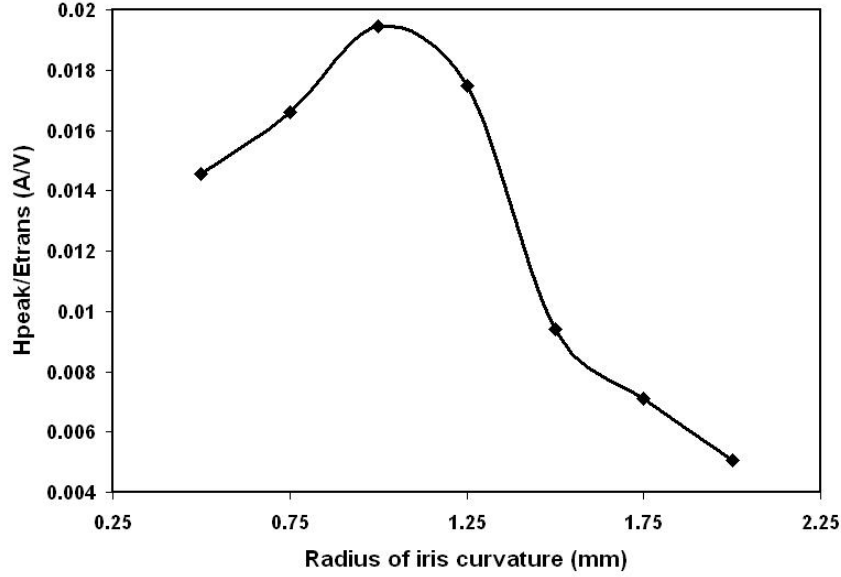


Figure 4.32: The effect of variation in the radius of the iris curvature  $cc$  on the  $H_{peak}/E_{\perp}$  of the dipole-like EM state. This result is for an infinitely periodic PBG crab cavity.

the resonant cavity. High surface fields can lead to X-ray emissions, surface melting and breakdown in a resonant cavity [183, 184]. Figure 4.30 suggest that the highest R/Q of this PBG crab cavity can be obtained when the iris curvature  $cc = 1.25\text{mm}$ . In figure 4.31, the value of  $E_{\perp}/E_{peak}$  was found to increase with increasing value of  $cc$ . The value of  $E_{\perp}/E_{peak}$  for this multicell PBG crab cavity is comparable to those obtained in [69] for a conventional travelling wave crab cavity. Also in figure 4.32, the lowest value of  $H_{peak}/E_{\perp}$  was found when  $cc = 2\text{mm}$ . From figures 4.30, 4.31 and 4.32 and based on the desire to minimize the surface fields as well as input RF power requirement, a PBG crab cavity with iris curvature  $cc = 1.5\text{mm}$  could be a preferred choice. The approach used in scenario 1 above to calculate the number of cells required to deliver the necessary 2.4MV transverse kick is adopted here in scenario 2. In order to avoid breakdown in

the alumina rods, 90% of the DC breakdown value (13.4 MV/m) for alumina is assigned to  $E_{inner}$  (i.e 12.06 MV/m).

From the electric field distribution of the dipole mode for  $cc = 1.5$  mm in the periodic cavity, the ratio of electric field  $E_{inner}$  in the innermost rods to the peak electric field  $E_{peak}$  is constant and given as  $E_{inner}/E_{peak} = 0.285$ . Therefore  $E_{peak}$  is calculated as:

$$E_{peak} = \frac{E_{inner}}{0.285} = \frac{12.06 \times 10^6}{0.285} = 42.37 MV/m \quad (4.26)$$

The parameter of merit  $E_{\perp}/E_{peak}$  depends on the the cavity design and remains constant for any given design. For the infinitely periodic PBG crab cavity with  $E_{\perp}/E_{peak} = 0.28$ , the maximum transverse gradient  $E_{\perp}$  that can be delivered is calculated as:

$$E_{\perp} = E_{peak} \times 0.28 = 42.37 \times 10^6 \times 0.28 = 11.86 MV/m \quad (4.27)$$

In order to deliver the 2.4 MV of transverse kick required by CLIC from a crab cavity with transverse gradient  $E_{\perp}$  of 11.86 MV/m, the cavity must have a longitudinal length  $d$  given as :-

$$d = \frac{V_{\perp}}{E_{\perp}} = \frac{2.4}{11.86} = 0.202m \quad (4.28)$$

In order to meet the requirement of a longitudinal length of 0.202 m for a  $\pi$  phase advance multicell structure where the active longitudinal length per cell  $d' = 0.0125$  m, the number of cells  $N$  required

for the multicell design is calculated as:

$$N = \frac{d}{d'} = \frac{0.202}{0.0125} = 16.18 \approx 16 \text{cells} \quad (4.29)$$

Scenario 2 suggest that a 20.2 cm long, 16 cells PBG crab cavity will deliver the 2.4MV transverse kick required by CLIC while avoiding breakdown in the dielectric rods. While bearing in mind that practical crab cavities are of finite longitudinal length and may have small variation in their parameters of merit, the periodic crab cavity is a good approximation for a long cavity [69]. The results scenario 2 is more believable because the cell-to-cell coupling is accounted for and the  $\pi$  phase advance between the periodic boundaries is enforced. The eigenfrequency simulation of the entire 16 cell PBG crab cavity requires more computational resources (computer memory) than was available for this work. However, at lower mesh density and taking advantage of the geometrical symmetries, the eigenfrequency simulation of a 4 cell PBG structure was performed and a plot of the electric field distribution of the dipole-like EM state is presented in figure 4.33.

#### 4.4.3 Power requirement for the PBG crab cavity design

The transverse voltage  $V_{\perp}$  scales with the amount of energy  $U_{cav}$  stored in the multi-cell PC cavity ( $N = 16$  cells) as follows:

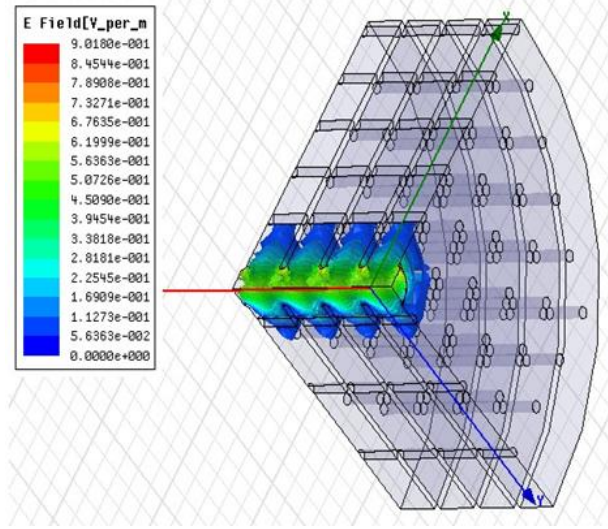


Figure 4.33: The electric field distribution of the dipole-like EM state confined by the lattice of a 4-cell PBG crab cavity. Note that only one quarter of the PBG structure is simulated with symmetric boundaries conditions set along the XZ and YZ planes.

$$U_{cav} = \frac{V_{\perp}^2}{\omega \frac{R}{Q} N} = \frac{(2.4 \times 10^6)^2}{(2 \times \pi \times 11.9942 \times 10^9) \times 14.05 \times 16} = 0.34 \text{ Joules} \quad (4.30)$$

Since the quality factor of the dipole mode was calculated to be  $Q_0 = 12956$ , the power dissipation  $P_{cav}$  required to achieve a stored energy of 0.34 Joules can be calculated as:

$$P_{cav} = \frac{\omega U_{cav}}{Q} = \frac{(2 \times \pi \times 11.9942 \times 10^9) \times 0.34}{12956} = 1.98 \text{ MW} \quad (4.31)$$

In practical accelerator application, the beams are not always on the Z-axis where the  $E_z$  of the dipole mode is zero but at an offset distance away from it. The beam sees the longitudinal component of the electric field  $E_z$  of the dipole mode which (depending on its phase

and the position of the beam) can give energy to or take energy away from the bunch. This energy exchange can accelerate or decelerate the bunch and can cause the amplitude and the phase of the cavity fields to change [68]. This is the beam loading effect which requires that the power deposited into or extracted from the cavity by the current train of particle bunches is taken into consideration when calculating the total input power for the PBG crab cavity. A bunch train of current  $I_b$  traveling through a cavity at a phase  $\omega t$  will deposit or extract power  $P_b$  which is given as :-

$$P_b = I_b V_z(x, t) = \frac{iqf_b\omega x_0 V_\perp e^{\omega t}}{c} \quad (4.32)$$

Where  $q$  is the bunch charge,  $f_b$  is the bunch repetition frequency,  $x_0$  is the maximum bunch offset away from the Z-axis,  $c$  is the free space speed of light,  $\omega$  is the angular frequency of the dipole mode,  $t$  is time of travel,  $V_\perp$  is the transverse voltage and  $i = \sqrt{-1}$  indicate that the transverse kick is  $90^\circ$  out of phase with the beam loading. For  $q = 0.6\text{nC}$ ,  $f_b = 2\text{GHz}$ ,  $x_0 = 0.0004\text{m}$ , phase  $\omega t = 0$ ,  $V_\perp = 2.4\text{MV}$  and with a cavity frequency of  $11.9942\text{ GHz}$ , the beam loading can be calculated as:-

$$\begin{aligned} P_b &= \frac{0.6 \times 10^{-9} \times 2 \times 10^9 \times 2 \times \pi \times 11.9942 \times 10^9 \times 4 \times 10^{-4} \times 2.4 \times 10^6}{2.99792458 \times 10^8} \\ &= 0.29\text{MW} \end{aligned} \quad (4.33)$$

Therefore the total power required to be delivered to the PBG

crab cavity is given as:-

$$P_{total} = P_{cav} + P_b = 1.98 + 0.29 = 2.27MW \quad (4.34)$$

The power requirement of the RF source for the entire multicell PBG crab cavity is estimated with consideration for the RF coupling scheme discussed in subsection 4.3.2 where only 97.21% of the input power couples into PC crab cavity (figure 4.25). In order to couple 2.27MW of power into the multicell crab cavity, an input power of 2.34MW is required from the RF source. Therefore each individual cavity of the 16 cell PBG structure will receive approximately 146KW of power.

#### 4.4.4 Damping the power of the parasitic modes

In previous sections, the selective confining ability of PBG structure have been demonstrated where a carefully designed PC lattice confined only the dipole-like EM state while forcing the LOM and the HOMs to propagate to the surroundings of the PBG crab cavity. Considering the amount of EM power (8.46 MW) that is needed to deliver the required 2.4 MV transverse kick and that part of this power will couple to the LOM and HOMs, it is important to find a way of dissipating/damping of the energy of these parasitic EM states. Silicon Carbide (SiC) blocks have been shown to be good microwave absorbers in [185] where they have been placed in the beam ducts of a 500 MHz cavity to dissipate the energy of HOMs. A sim-

ilar approach can be adopted for the PBG crab cavity to dissipate the power of the parasitic modes as they reach the outer boundaries of the PC lattice. In this case, tapered blocks of SiC ( $\epsilon_r = 6.25$ ; loss tangent = 0.6) can be placed around the outer edges of the PBG structure as show in figure 4.34.

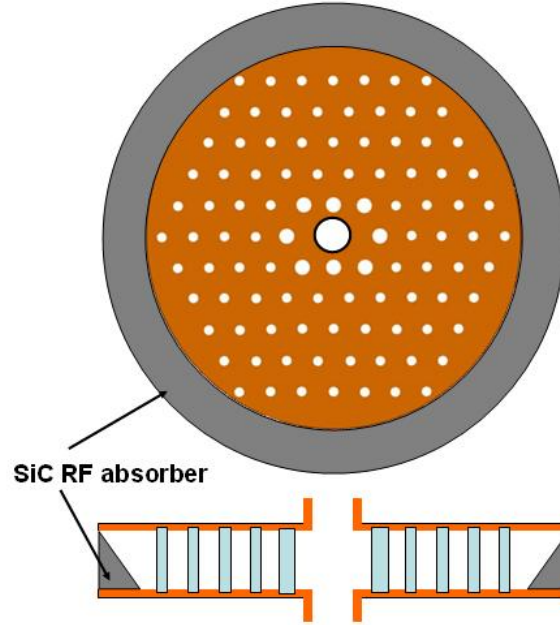


Figure 4.34: Schematic diagram showing the position of the silicon carbide RF absorber at the outer boundary of the PC lattice.

The microwave damping ability of SiC blocks was investigated by calculating the scattering parameter  $S_{11}$  of an incident wave on the tapered SiC block in a waveguide. For a tapered angle of  $14^\circ$ , the  $S_{11}$  calculated for a frequency range of 6 GHz to 30 GHz is shown in figure 4.35 while the distribution of the electromagnetic field inside the SiC block is shown in the inset.

The average value of  $S_{11}$  in figure 4.35 are of the order of 0.007 ( $< 1\%$ ) which indicate that the reflected energy is negligible. The EM field can be seen in figure 4.35 to penetrate the SiC block just

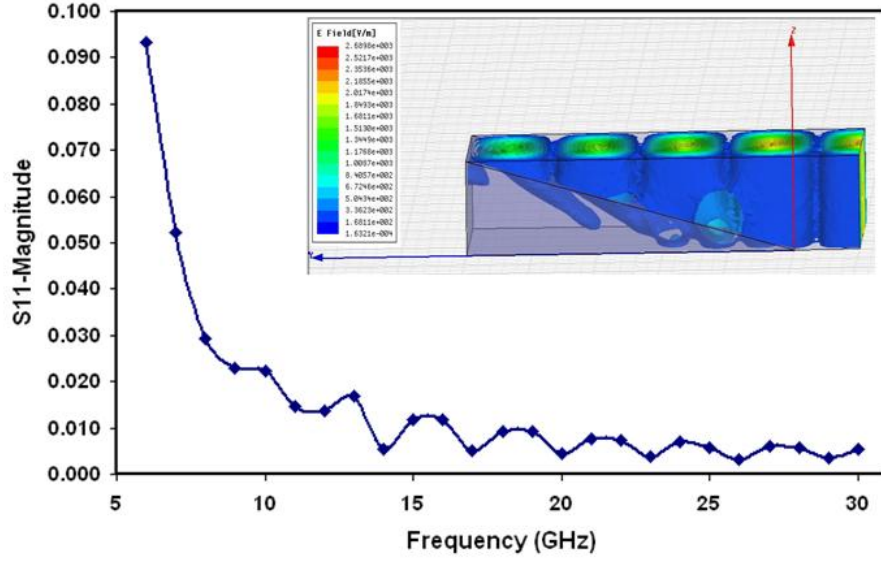


Figure 4.35: The reflection coefficient  $S_{11}$  of an EM wave (6 GHz to 30 GHz) incident on a tapered block of silicon carbide RF absorber. The distribution of the electric field within the SiC block is shown in the inset.

slightly without reaching the other side of the block. This setup ensures that the energy of the parasitic modes are not allowed to bounce around in the vacuum chamber in which the PBG crab cavity will be operated.

## 4.5 A cooling system for the PBG crab cavity

This section discusses a possible cooling approach for the PBG crab cavity. First of all, it is important to determine the parts of the PBG structure that is most likely to become very hot and damaged by the heat. The heat in the system is caused by losses in both the dielectric rod as well as the metallic plates. A numerical calculation of the volumetric losses  $P_v$  in the dielectric rods (from equation 4.35) and the surface losses  $P_s$  in the metallic plates (from equation 4.36) was performed using HFSS and the results were found for the infinitely

periodic PBG structure to be  $6.14 \times 10^{-31}$  J and  $5.42 \times 10^{-12}$  J respectively.

$$P_v = \frac{1}{2} \text{Re}(E \cdot J^* + (\nabla \times E) \cdot H^*) \quad (4.35)$$

$$P_s = \text{Re}(S \cdot \hat{n}) \quad (4.36)$$

Where  $S$  is the poynting vector on the boundary and  $\hat{n}$  is the outward unit vector that is normal to the boundary.  $J^*$  and  $H^*$  are the conjugate of the volumetric current density and the magnetic field respectively. This indicates that the entire losses in the PBG structure are dominated by the Ohmic losses in the metallic plates. The tangential magnetic field on the surface of the metallic plate induces an eddy current which causes that surface to heats up [187]. When the high power RF source is pulsed, the heating as well as the resulting thermal stress on the surface of the metal will occur faster than the material has time to expand. This thermal stress can cause thermal fatigue in the form of micro-cracks and surface roughness in the metal over many RF cycles [187]. This is generally referred to as pulsed heating. The concentration of the peak magnetic field (shown in figure 4.36) around the iris suggest that this region of the metallic plate is most likely to become hot and will require cooling.

The temperature rise threshold beyond which degradation begins to occur in Oxygen Free Electronic (OFE) copper is given in [186, 187] to be 40 K. A temperature rise of  $\approx 50 - 60^\circ C$  per pulse

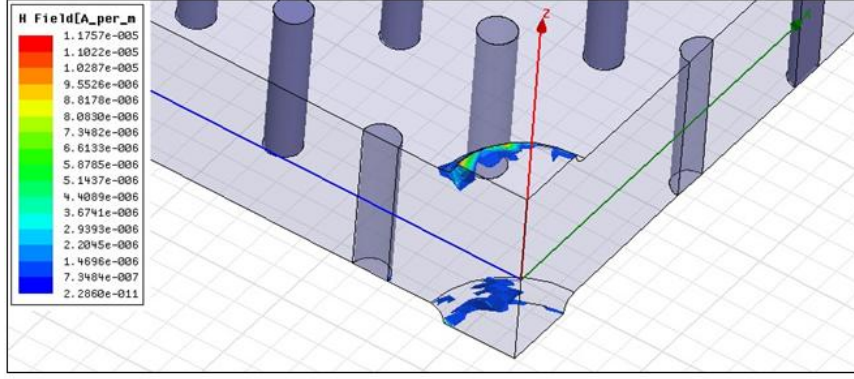


Figure 4.36: Peak magnetic field is concentrated around the iris of the PBG crab cavity.

was calculated for the accelerating structures at CLIC [188]. This temperature rise is above the threshold for damage in the copper structures and remains a major concern for researchers working on the project. The increase in temperature  $\Delta T$  of the PBG structure as a result of pulse heating was calculated using the approach of [36, 186, 189] and applying the following formula:-

$$\Delta T = R_s H_{peak}^2 \sqrt{\frac{t_{pulse}}{\pi \rho c_v k'}} \quad (4.37)$$

Where  $H_{peak}$  is the peak magnetic field found anywhere within the PBG structure,  $R_s = 0.1\Omega$  is the surface resistance of Oxygen Free Highly Conductive (OFHC) copper at room temperature [190],  $t_{pulse} = 100\text{ns}$  is the pulse duration of the RF source,  $\rho = 8900\text{kg/m}^3$  is the density of copper,  $c_v = 384\text{J/Kg/}^\circ\text{C}$  is the specific heat per unit mass of copper and  $k' = 380\text{W/}^\circ\text{C/m}$  is the thermal conductivity of copper. From the HFSS simulation result for the multi-cell PBG crab cavity in figure 4.32, the parameter of merit  $H_{peak}/E_{\perp}$  is given as  $0.0094\text{A/V}$  for an iris with curvature radius of  $cc = 1.5\text{mm}$ . Using

the value of transverse gradient  $E_{\perp} = 11.86\text{MV/m}$  calculated in equation 4.27 for a transverse kick of 2.4 MV, the magnitude of the magnetic field in the PBG structure is calculated as :-

$$H_{peak} = \left( \frac{H_{peak}}{E_{\perp}} \right) \times E_{\perp} = 0.0094 \times (11.86 \times 10^6) = 111.484\text{kA/m} \quad (4.38)$$

When the parameters given above are applied to equation 4.37, the maximum rise in temperature  $\Delta T$  is calculated to be  $\sim 6^{\circ}\text{c}$ . This indicates that the iris being the hottest point in the PBG crab cavity will have a temperature rise of  $6^{\circ}\text{c}$ . This temperature rise is comparable to those obtained for metallic PBG structure in [36] and is below the threshold for damage in the copper plate. For an ambient temperature of  $25^{\circ}\text{c}$ , the temperature at the iris will be  $31^{\circ}\text{c}$ . Furthermore, the temperature distribution on the surface of the metallic plate was simulated with COMSOL in figure 4.37 and the effect of water cooling is shown in figures 4.38 and 4.39. In the absence of any cooling, figure 4.37 shows how the peak temperature of  $31^{\circ}\text{C}$  at the iris drops exponentially to the ambient temperature of  $25^{\circ}\text{C}$  with distance away from the iris. The conduction of the heat away from the iris results in a temperature rise in the entire plate over a period of time.

Since the iris is close to the centre of the PBG structure, it is not accessible to be cooled directly. However, the heat energy concentrated at the iris will be transferred to the edges of the metallic plate

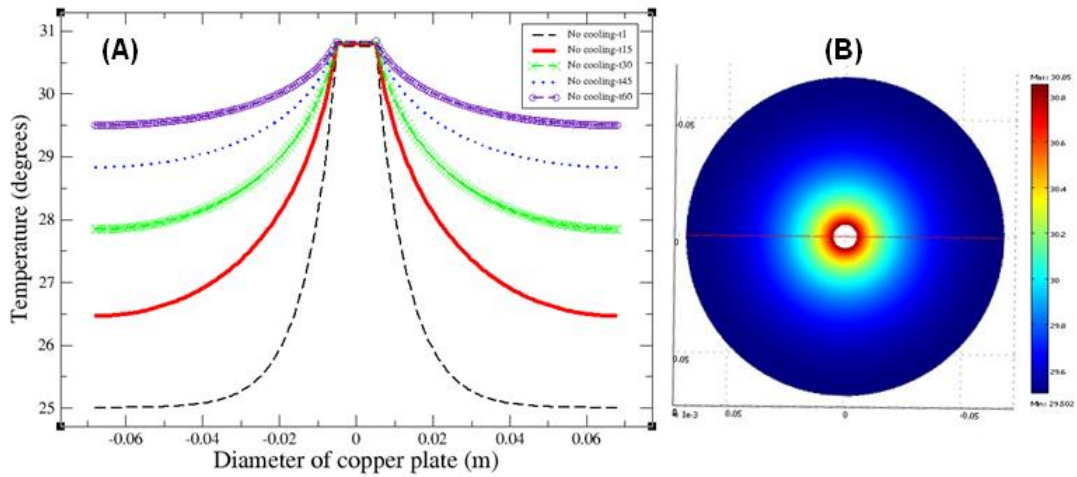


Figure 4.37: (A) The temperature distribution across the copper plate over a period of time when there is no cooling. (B) The maximum temperature on the iris decreases with distance towards the edges.

by conduction as copper is a very good conductor of heat [191]. The PBG structure can then be water cooled by allowing a fast moving water current to flow through a hollow copper tube attached to the edges of the copper plates as shown in figure 4.38. The water current carries away the heat as it is generated by the RF power.

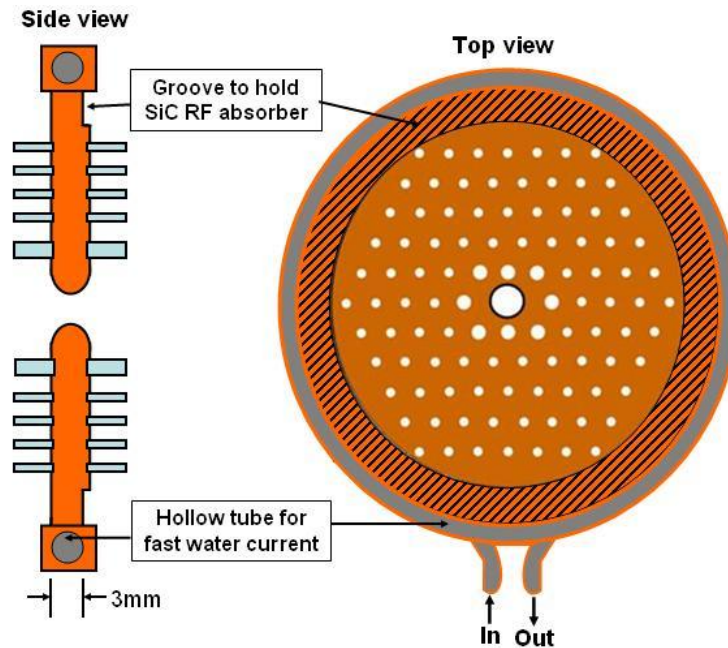


Figure 4.38: Schematic diagram showing the hollow water cooling tube attached to the outer edges of the metallic plate.

In figure 4.39, the water cooling of the copper plate caused a significant drop in the temperature of the plate and the relative temperature drop becomes greater with time. Water cooling is an easy and popular way to control the temperature of normal conducting cavities [36, 187].

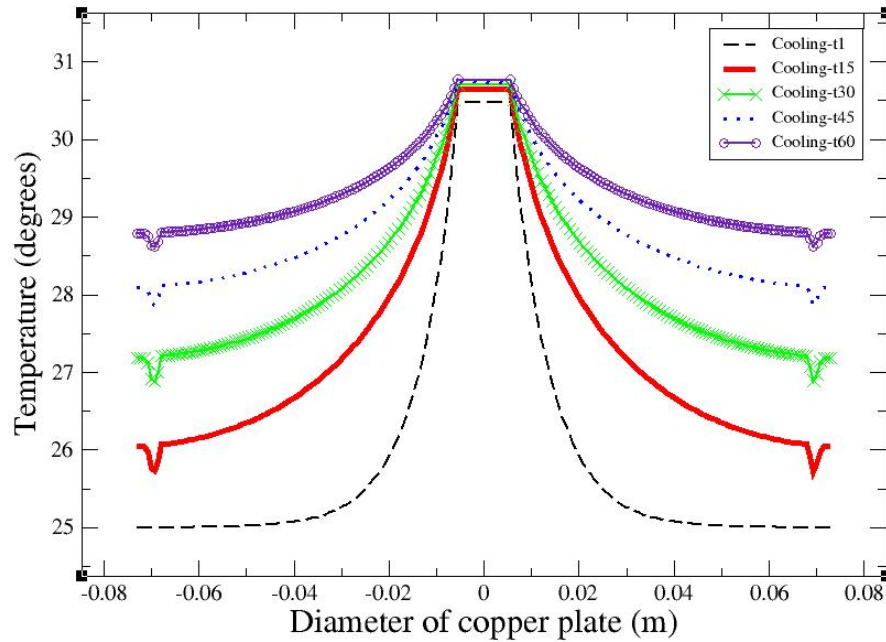


Figure 4.39: The effect of cooling on the temperature distribution across the copper plate over a period of time. The temperatures across the copper are lower when water cooling is used than in the case when there is no cooling.

## 4.6 A fabrication approach for the PBG crab cavity

This section describes a possible fabrication approach for the 16 cells PBG crab cavity. Based on the final design parameter in table 4.2 , a description of the individual component parts as well as the method of assemblage is detailed below.

### 4.6.1 The dielectric rods

The PBG crab cavity is made of dielectric rods ( $\epsilon = 9.5$ ; loss tangent = 0.0002) of four different sizes. The innermost rods closest to the double point defect of the coupling cavities have a radius of 1.327 mm while the bulk lattice rods of the coupling cavities have a radius of 1.152 mm. For non-coupling cavities, the innermost rods closest to the defect have a radius of 1.401 mm while the bulk lattice rods have a radius of 1.189 mm. All the dielectric rods are 10.5 mm long with 0.5 mm on either end tapered for easy fit into small hole in the top and bottom plates as shown in figure 4.40.

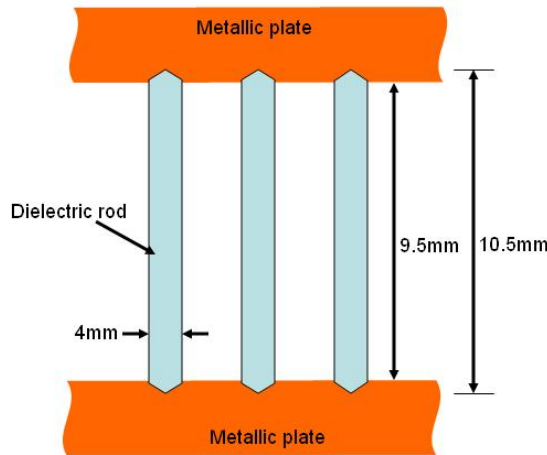


Figure 4.40: Schematic diagram showing how the dielectric rod can fit into the metallic plates.

Sapphire is a low loss dielectric material which, depending on its purity, has a permittivity range between 9 and 12 and loss tangent of 0.0001 [192]. Sapphire rods can be machined to an accuracy of 0.001 mm. This makes off-the-shelf sapphire rods a good candidate for the fabrication of the PBG crab cavity.

## 4.6.2 The metallic plates

The function of the metallic top and bottom plates is to present a total-internal-reflection boundary to the EM waves in the direction that is perpendicular to the dielectric rods of the 2D PBG structure. The metallic plates also offer structural support to the dielectric rods and provide an iris through which the particle bunches can travel. Furthermore, the metallic plates must provide space for the installation of the Silicon Carbide microwave absorber on the outer boundaries of the PC lattice along the plane of periodicity. The design of the metallic plates must also take into consideration a means of connecting the multiple cells of the PBG crab cavity. Figure 4.41 shows a design of a metallic plate that take into consideration all the issues mentioned above.

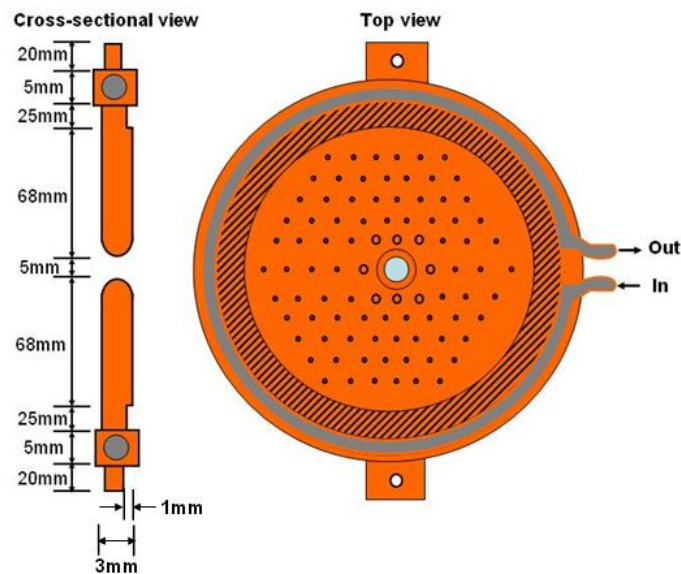


Figure 4.41: Schematic diagram showing the design of the metallic plates. The flanges are attached to allow several plates to be attached using bolts and nuts. Note that the diagram is not to scale.

The metallic plate should be made of OFHC copper to minimize

Ohmic losses. The plates should be electropolished to achieve a very smooth surface finish and prevent the concentration of high electric fields on rough edges. The centre bears an iris through which the particle bunches will travel. The iris should be rounded with an iris curvature radius of 1.5 mm. The positions of the dielectric rods are marked on the surface of the metallic plates by small holes drilled by a CNC machine to an accuracy of 0.01 mm. This design incorporates a small groove where the SiC microwave absorbers will be positioned at the outer edges of the lattice. Beyond the small grooves of the metallic plates is a ring hollow tube which allow the flow of water to cool the plates. Furthermore, the attached flanges on two sides of the plate provide structural support for the multicell PBG structure. The flanges bear holes to allow several metallic plates to be attached using nuts and bolts.

### **4.6.3 The assemblage of the PBG crab cavity**

This subsection discusses how individual component parts of the designed 16 cell PBG crab cavity are coupled together into a complete particle deflecting cavity. For ease of tuning and optimization after fabrication, the 16 cell design of the PBG crab cavity can be divided into four sets of 4-cell PBG structure. An illustration of a set of 4-cell PBG structure is shown in figure 4.42.

Figure 4.42 presents the assembly of a 4 cell module of the 16 cell PBG design. The beam tube and the iris of each cell must be properly aligned to create a clear path in-which the particle bunches

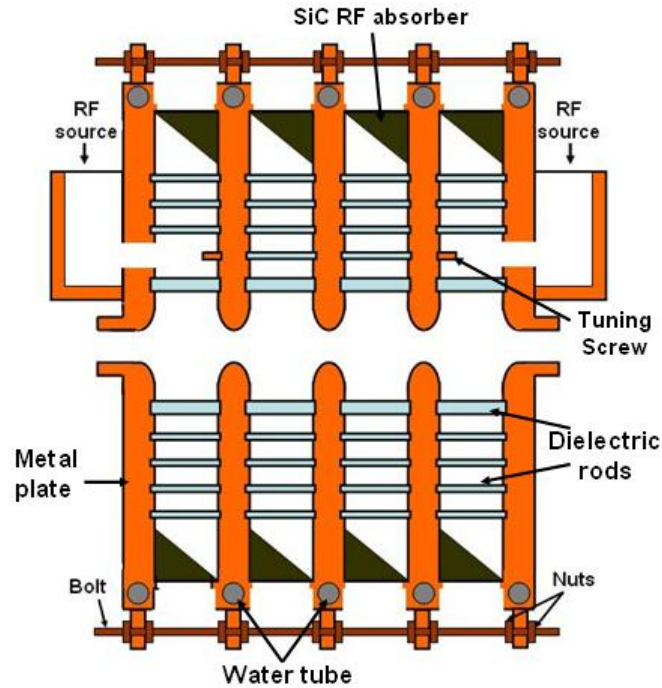


Figure 4.42: Cross-sectional schematic diagram showing the assemblage of a 4-cell PBG crab cavity. The two cells at the ends of the setup are coupling PBG cavity cells with waveguides attachments to couple EM power from an RF source. Note that the diagram is not to scale.

can travel. The dielectric rods are arranged according to the triangular lattice of holes drilled into both sides of the metallic plates. The dielectric rods are sandwiched between the metallic plates with 0.5 mm on either side of each rod buried within the plates. Each rod must be aligned to be as perpendicular as possible to the metallic plate. In this assembly, the two outer cells provide RF coupling with waveguides attached to them. As discussed in section 4.3.2, the lattice dimension of the coupling cells is different from those of the two inner PBG cavities. By counting the metallic plates from left to right in figure 4.42, the 2nd and 4th plates incorporate small metallic tuning rods at the point opposite the coupling iris of the waveguide. The flanges on all the metallic plates can be attached

together using a set of bolts and nuts as shown in figure 4.42. A long bolt is passed through the round hole in each metallic plate where the plates is fastened to the bolt by two nuts on either side of each flange of the metallic plate. The nuts should be fastened carefully to ensure that the required cavity height of 9.5 mm is achieved. This assembly approach allow for easy dismantling of the PBG structure in order to make minor alterations which are usually required to compensate for unavoidable fabrication errors. When the entire 16 cell PBG structure is put together as shown in figure 4.43, the size of the complete PBG crabbing system can be calculated by summing up the dimensions of individual PBG cavity cells and other components. The dimensions of the metallic plate shown in figure 4.41 gives the total transverse length of 24.1 cm for the complete multicell PBG crab cavity. Also by adding up the single cell length of 1.25 cm for the 16 cells structure and the X-band waveguide height of 1 cm for 8 waveguides gives a total longitudinal length of 28 cm. Therefore a standard 12"  $\times$  18" horizontal industrial vacuum chamber is ideal to contain the PBG crab cavity. An illustration of how the complete PBG crabbing system might look is given in figure 4.43 below.

This chapter has presented the use of a PBG structure for crabbing application. The lattice design presented in chapter 3 was rescaled and optimized to confine only the  $TM_{110}$ -like dipole EM state at 11.9942 GHz while forcing all other EM state to propagate away from the defect region. The suppression of long range Wake-

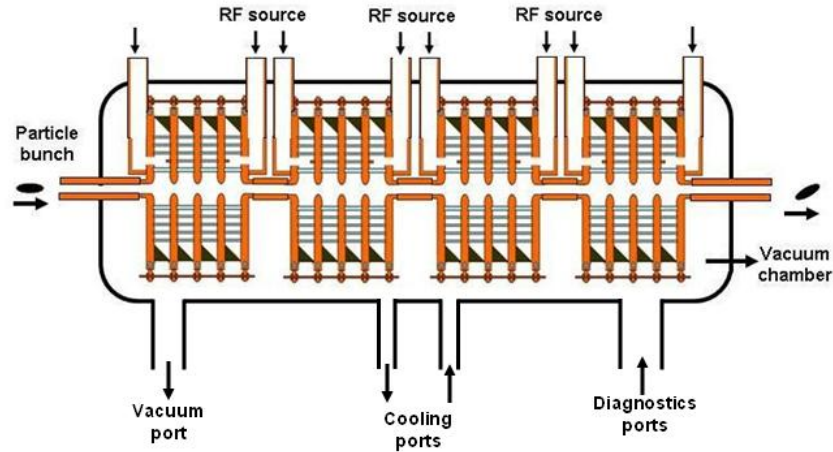


Figure 4.43: Cross-sectional schematic diagram showing how the complete 16-cell PBG crabbing system might fit into a vacuum chamber. Note that the diagram is not to scale.

fields in the PBG crab cavity was demonstrated without the use of any external mode damping scheme. This work found that the 2.4 MV transverse kick required by CLIC can be delivered by a 16-cell PBG crab cavity. Operational issues such as the damping of the parasitic modes on the boundary of the lattice, the cooling of the metallic plates, and the eventual fabrication of the PBG structure have been addressed in this chapter. Overall, this PBG crab cavity design improves on the conventional pillbox-type crab cavities by minimizing the effect of long range wakes without any major addition to the complexity of the crab cavity.

# Chapter 5

## Dirac Point in Photonic Analogues of Graphene

### 5.1 Introduction

As discussed in chapter 1, photonic crystals are best known for the presence of band gaps in their dispersion diagram. This is analogous to the presence of electronic band gaps in semiconductors. In semiconductors and photonic crystals, perturbations are used to control the flow of electrons and photons respectively. Other effects whose analogs have been investigated in photonic crystals include negative refraction [193, 194, 195, 196], localization in disordered PCs [197, 198], the Zitterbewegung effect [199], the Hofstadter butterfly effect [200], quantum hall effects [201] etc. Since the successful fabrication of graphene in 2004 [98, 107], the interest in graphene has increased due to its fascinating electronic properties [107]. Graphene is a single layer of carbon atoms arranged in a 2D honeycomb lattice. The electronic energy dispersion of graphene has, at the corners

of the Brillouin zone, points where the conduction and the valence band touch to create a conical singularity which is usually called the Dirac point [92]. As the Dirac point is approached, the energy of the electron travelling through the graphene sheet depends linearly on their quasi-momentum [94] as illustrated in section 5.2. Recently, the exhibition of a Dirac point in the dispersion plot of photonic crystals has been investigated both theoretically [202, 203, 204] and experimentally [48, 49]. This is analogous to the conical singularity found in the electronic band structure of graphene [107, 97].

Since photonic crystals can be fabricated at a macroscopic length scale, they offer an easier means of investigating many nanoscale effects which are usually challenging to study in natural crystals like a single sheet of graphene. For example, the pseudo-diffusive transmission extremal found near the Dirac point of photonic crystals [206] is difficult to observe in the electronic case due to the challenge of maintaining a homogeneous electron density in the whole system [207]. In this chapter, a carefully designed experimental measurement of the transmission spectrum of microwaves in a photonic crystal was used to demonstrate a well pronounced appearance of the Dirac point similar to those obtained in [48, 49]. This work adds to the two aforementioned articles by studying the sensitivity of the Dirac point to the incident and receiving angles of waves propagating away from the  $\Gamma - K$  direction at the input and output boundaries respectively.

## 5.2 Theoretical background of Dirac point in Photonic crystals

In a similar way to the energy dispersion of graphene, the electromagnetic dispersion plot of photonic crystals has bands of modes touching at the corner of the Brillouin zone (K-point of symmetry). There are two sets of equivalent K-points ( $K_n$  and  $K_n'$ ) at the corners of the Brillouin zone of PCs, where ( $n = 1, 2, 3$ ) as shown in figure 5.1.

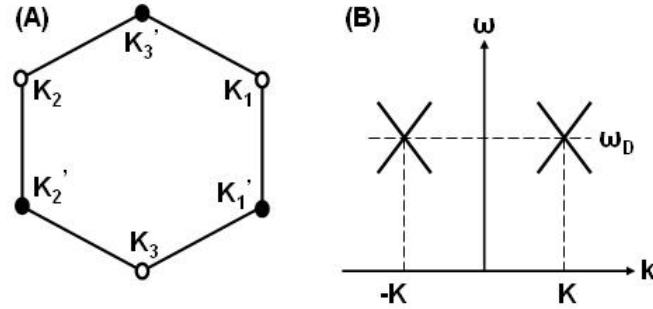


Figure 5.1: (A) The Brillouin zone of a hexagonal PC showing the two sets of equivalent corners at  $K_n$  and  $K_n'$  where  $n = 1, 2$ , and  $3$ . (B) The dispersion plot of the doublet mode at the corners of the Brillouin zone. The frequency of the doublets separates linearly as the  $k$ -direction shift away from the corner of the Brillouin zone

Due to the periodicity of the dielectric PC medium, normally degenerate modes in homogeneous dielectric medium are split into a pair of doublets and a pair of singlets at the K-point of the Brillouin zone [201, 208, 209]. Each of the two equivalent sets of K-point have a doublet at the Dirac frequency ( $\omega_D$ ) and a singlet at a different frequency [206]. As the wave vector is shifted away from the K-point of the Brillouin zone by ( $dk$ ) each doublet mixes and separates linearly to create a Dirac point. The theoretical background presented

in this section is based on the analysis presented in [206] where the photonic crystal is considered as a system with input and output signals as well as transfer matrices for individual subsystems that make up the photonic crystal. For a planewave propagating in free space, Maxwell's equation is reduced to the Helmholtz equation given as :-

$$\nabla_{\perp}^2 \vec{E}(x, y) + \left(\frac{\omega}{c}\right)^2 \vec{E}(x, y) = 0 \quad (5.1)$$

Where  $\nabla_{\perp}^2$  is the Laplacian,  $\omega$  is the angular frequency and  $c$  is the speed of light in free space. On the other hand, for a wave propagating inside a photonic crystal, Maxwell's equation reduces to the Dirac equation [201, 208] given as :-

$$\begin{pmatrix} 0 & \partial x - i\partial y \\ \partial x + i\partial y & 0 \end{pmatrix} \begin{pmatrix} \psi_1 \\ \psi_2 \end{pmatrix} = \frac{i(\omega - \omega_D)}{V_D} \begin{pmatrix} \psi_1 \\ \psi_2 \end{pmatrix} \quad (5.2)$$

Where  $V_D$  is the group velocity of the wave inside the photonic crystal, while  $\psi_1$  and  $\psi_2$  are the amplitude of the doublet of two degenerate states at a given K-point of the Brillouin zone. In order to excite the doublet states within the photonic crystal, the wave vector  $\mathbf{k} = (k_x, k_y)$  of the incident wave must be matched to at least one of the K-points  $\mathbf{K}=(K_x, K_y)$ . If the y-component of the wave vector  $k$  of the incident wave is assumed to be conserved at the input boundary of the PC because the planewave is propagating in the direction of  $k_x$ , then the matched incident wave can be written as :-

$$\vec{E}_{in}(x, y) = \vec{E}_+(x, y)e^{i(k_0x+K_yy)} \quad (5.3)$$

$$k_0 = \sqrt{\left(\frac{\omega_D}{c}\right)^2 - K_y^2} \quad (5.4)$$

Where  $\vec{E}_+$  is a slowly varying function in the forward direction.  $k_y = K_y$  and  $k_x = k_0$  for a matched incident wave. The type of boundary seen by the incident wave determines the type of mode excited within the photonic crystal. For an arm-chair boundary, only one of the inequivalent doublet modes is excited while a mixture of the two inequivalent doublets is excited in the case of a zig-zag boundary [206]. In order to determine the amplitude of the excited modes, the solution of the Helmholtz equation in free space must be matched to the solution of the Dirac equation inside the photonic crystal. This matching is done assuming that the photon number flux ( $J = \text{photon power}/\text{photon energy}$ : unit is  $s^{-1}$ ) across the boundaries is conserved. The photon number flux  $J_H$  for the Helmholtz equation is given in [210] as :-

$$J_H = \frac{\varepsilon_0 c^2}{4i\hbar\omega^2} \left( \vec{E}^* \frac{\partial \vec{E}}{\partial x} - \vec{E} \frac{\partial \vec{E}^*}{\partial x} \right) = V_H \xi^* \sigma_x \xi \quad (5.5)$$

$$\text{Where } V_H = \frac{\varepsilon_0 c^2 k_0}{4\hbar\omega^2} \quad \text{and} \quad \xi = \begin{pmatrix} \vec{E}_+ + \vec{E}_- \\ \vec{E}_+ - \vec{E}_- \end{pmatrix} \quad (5.6)$$

$\vec{E}_-$  is a slowly varying function in the reverse direction away from

the input boundary. Also the photon number flux  $J_D$  for the Dirac equation is given as :-

$$J_D = V_D(\psi_1^*\psi_2 + \psi_2^*\psi_1) = V_D\psi^*\sigma_x\psi \quad (5.7)$$

At the input boundary for the planewave, the conservation of the photon number flux requires that  $J_H = J_D$ .

$$V_H\xi^*\sigma_x\xi = V_D\psi^*\sigma_x\psi \quad (5.8)$$

Therefore, the amplitude of the doublet mode at the input boundary is given as:-

$$\psi = \left(\frac{V_H}{V_D}\right)^{\frac{1}{2}} M\xi \quad (5.9)$$

Where M, which must satisfy the unitary condition, is the transfer matrix for the input boundary and its value depends on the detail of the boundary at the scale of the lattice constant [206].

$$M^{-1} = M^\dagger \quad (5.10)$$

Where  $M^\dagger$  is the conjugate transpose of  $M$ . Also at the exiting boundary, the amplitude of the doublet is given as:-

$$\psi = \left(\frac{V_H}{V_D}\right)^{\frac{1}{2}} M'\xi \quad (5.11)$$

Where  $M'$  is the transfer matrix for the exiting boundary and it must also satisfy the unitary condition. The amplitude of any

particular  $n^{th}$  mode  $\phi_x$  at the input boundary ( $x = 0$ ) is related to the amplitude at the exiting boundary ( $x = L$ ) by the transfer matrix  $M_n(L, y)$  which can be calculated by solving the Dirac equation inside the photonic crystal.

$$\phi_n(L) = M_n(L, y)\phi_n(0) \quad (5.12)$$

The total transfer matrix  $\eta$  of the entire photonic crystal system can be written as [206]:-

$$\eta = M' M_n M \quad (5.13)$$

$$\eta \begin{pmatrix} 1 + r_n \\ 1 - r_n \end{pmatrix} = \begin{pmatrix} t_n \\ t_n \end{pmatrix} \quad (5.14)$$

Where  $r_n$  and  $t_n$  are the reflection and the transmission amplitude and the transmission probability is  $T_n = |t_n|^2$ . For an incident photon current  $I_0$  of a mode at frequency  $d\omega$ , the transmitted time averaged photon current through the photonic crystal is given as:-

$$I(d\omega) = I_0 \sum_{n=-\infty}^{\infty} T_n(d\omega) \quad (5.15)$$

As shown in [48, 49], the transmitted photon current drops linearly towards zero as the Dirac point is approached.

### 5.3 The Experimental Setup

In this work, a photonic analog of graphene was studied using a PC made from a hexagonal lattice of sapphire ( $\varepsilon = 11$ ) cylindrical rods embedded in air with  $r/a = 0.2$  and length  $L = 10\text{mm}$ . Sapphire is a good non-absorbing dielectric material that can be machined to a precision of 0.001 mm. This eliminates the losses in the EM fields due to absorption by the dielectric material and minimizes disorder usually introduced to the PC by variations in the radius of the cylindrical rods along their length. The hexagonal lattice of sapphire rods was sandwiched between top and bottom aluminum plates. The separation ( $L$ ) between the plates only allows the propagation of EM states with Transverse Magnetic (TM) polarization with electric field perpendicular to the metallic plates. Each sapphire rod is carefully positioned to sit in holes forming a hexagonal lattice in the bottom plate. The position of each point is accurate to 0.01 mm.

As shown in figures 5.2 and 5.3, the experimental setup used in this study was driven by a dipole antenna. The entire boundary of the setup was covered with an off-the-shelf EM absorbers called Eccosorb. First, to chop off the curvature of the radial wave emitted by the antenna in order to form a planewave and secondly to prevent the effects of wave reflections from side walls or surrounding objects in the laboratory. On the other end of the lattice, another dipole antenna was used to measure the transmitted power of EM states. Both antennas were connected to the ports of a network analyzer

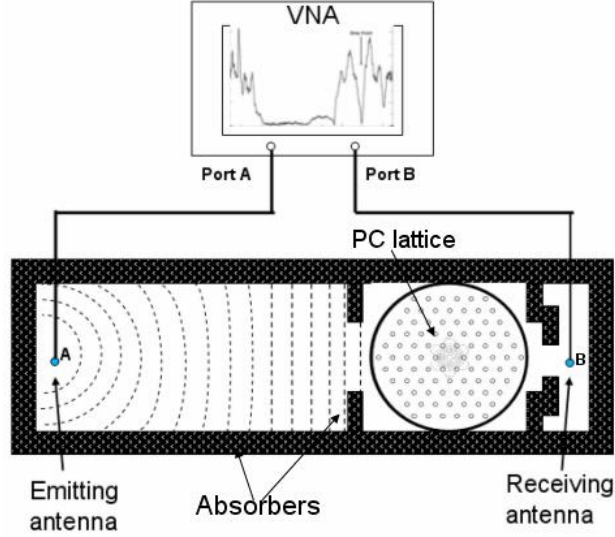


Figure 5.2: A schematic diagram of the experimental setup to measure the transmission plot  $S_{21}$  for a plane wave through a hexagonal lattice of sapphire rods ( $\epsilon = 11$ ) and  $r/a = 0.2$ .

which calculated the scattering matrix of waves sent between the ports. At the input boundary of the PC, EM absorbers are used to shield off components of the incident wave propagating in directions that are away from the  $\Gamma - K$  direction. The EM absorbers at the input boundary of the lattice also ensure that the incident wave has the flat wave front expected from a plane wave. Once the plane wave enters the PC, multiple scattering occurs and the emanating waves at the other end of the lattice propagate in various directions depending on their wave vector  $k$ . In order to isolate and measure only EM states in the  $\Gamma - K$  direction, additional absorbers were placed around the receiving antenna to shield off and prevent the measurement of wave propagation at arbitrary angles. A photograph of the physical experimental setup is shown in figure 5.3.

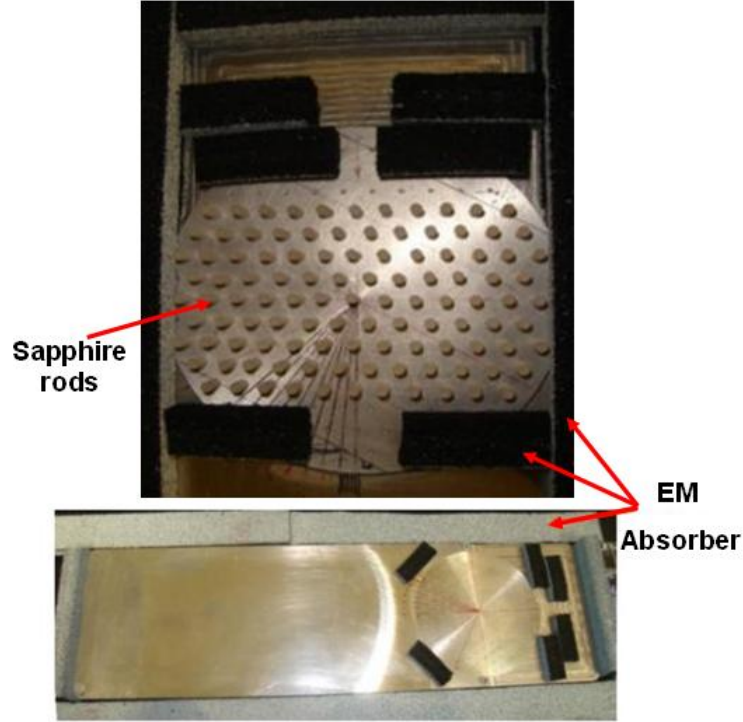


Figure 5.3: Experimental setup to measured the transmission plot  $S_{21}$  for a planewave through a hexagonal lattice of sapphire rods( $\varepsilon = 11$ ) and  $r/a = 0.2$ .

## 5.4 Experimental results for a hexagonal lattice of cylindrical rods

The dispersion diagram for a 2D infinite hexagonal lattice with  $r/a = 0.2$  and  $\varepsilon = 11$  was calculated using the Plane Wave Expansion (PWE) method. As shown in the figure 5.4, the second and third bands of eigenstates are touching at the corner of the Brillouin zone due to doubly degenerate states that create the conical singularity called the Dirac point. The local bandgap for the  $\Gamma - K$  direction can be seen between  $a/\lambda = 0.29$  and  $a/\lambda = 0.47$ . The Dirac point was found at  $a/\lambda = 0.504$ . Although the 2D PWE simulation code was for an infinite lattice of cylindrical rod, in reality, and in our experimental implementation a finite lattice had to be used.

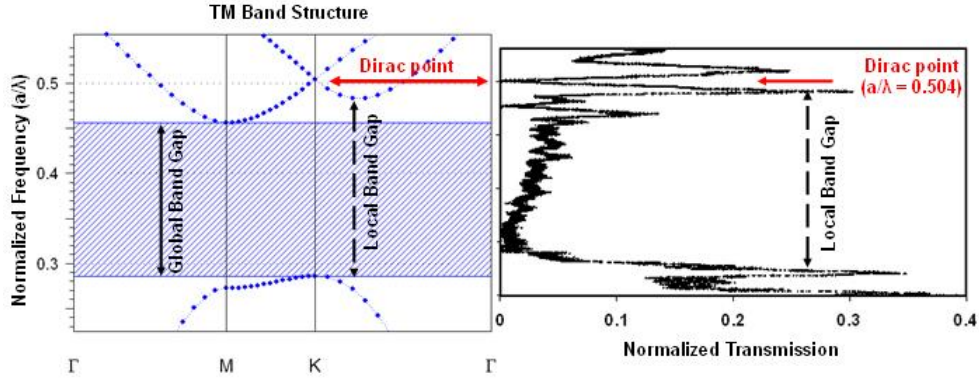


Figure 5.4: The dispersion plot for a 2D hexagonal lattice of dielectric cylinders ( $\epsilon = 11$ ) with  $r/a = 0.2$ . The Dirac point seen at  $a/\lambda = 0.504$  at the corner of the Brillouin zone (K-point) matches the linear drop in the transmission shown in the experimental measurement on the right.

A reference measurement (shown in figure 5.5) was taken without the lattice of sapphire rods and used to normalize the subsequent measurements taken with the lattice. This ensures that the observed effects and phenomena are due to the presence of the hexagonal lattice of sapphire rods.

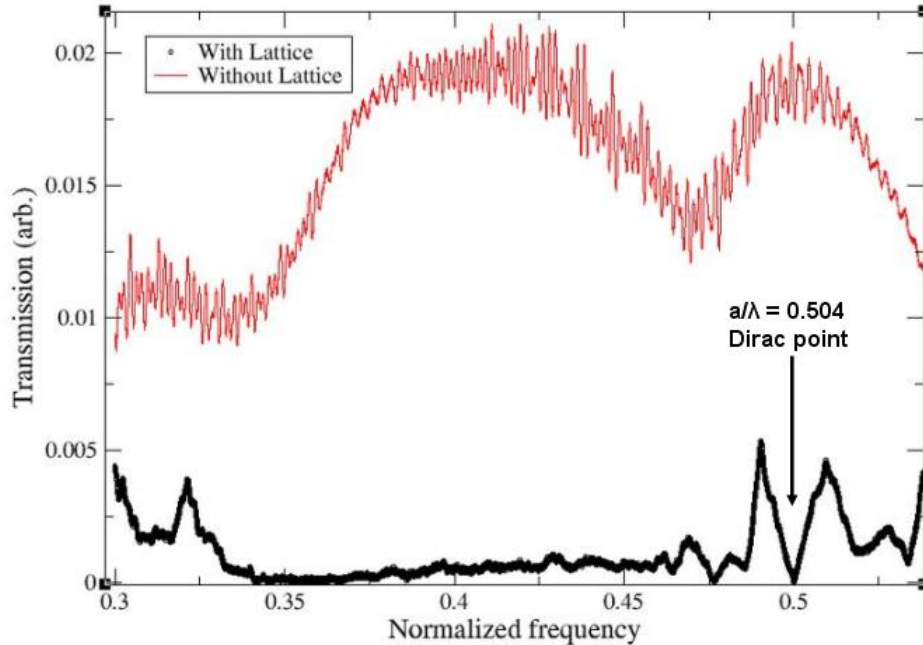


Figure 5.5: Measured transmission plot  $S_{21}$  for a planewave propagating through a hexagonal lattice of sapphire rods ( $\epsilon = 11$ ) with  $r/a = 0.2$ . The Dirac point seen at  $a/\lambda = 0.504$  is as a result of the lattice

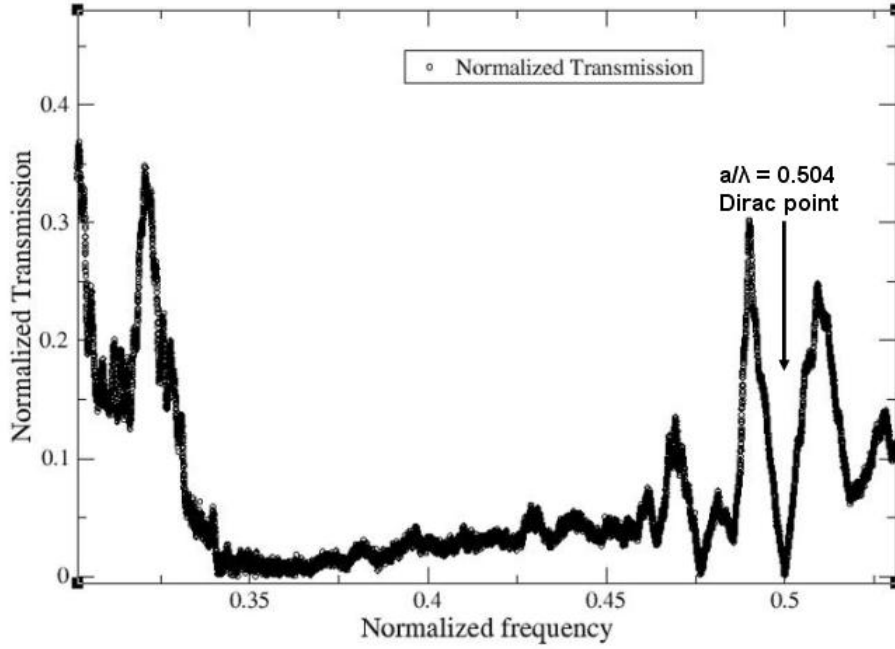


Figure 5.6: Normalized transmission plot  $S_{21}$  for a planewave propagating through a hexagonal lattice of sapphire rods ( $\varepsilon = 11$ ) with  $r/a = 0.2$ . The Dirac point can be seen at  $a/\lambda = 0.504$

In the experimental result shown in figure 5.6, the band gap can be seen between  $a/\lambda = 0.325$  and  $a/\lambda = 0.475$  and a sharp linear drop in transmitted EM states with a minimum at the Dirac point was found at  $a/\lambda = 0.504$ . The small variations between the PWE numerical values and the experimental values are due to the finite size of the lattice used in the experiment as compared to the infinitely periodic lattice of the PWE code. Since the Dirac point in a PC is determined by the dielectric constant of the scatterers and the filling factor of the lattice, small experimental errors between the numerical and experimental values of the lattice parameters will cause a shift in the position of the bandgap and the Dirac point. Nevertheless, the linear drop in the Density of states (DOS) at the Dirac point is unmistakable.

In order to investigate the repeatability and the experimental error in the setup, 10 different ensembles of the metallic top plate positions were used and the measurements were repeated for each case. The average transmission measurement and the error limits calculated from the standard deviation is presented in figures 5.7.

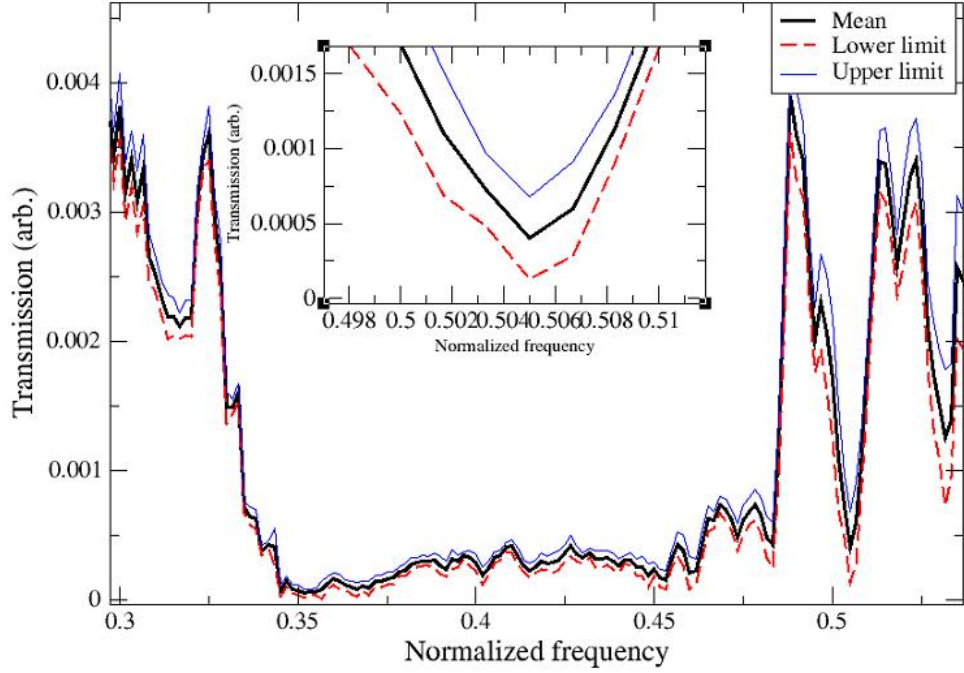


Figure 5.7: Measured transmission plot  $S_{21}$  for 10 ensembles of top plate configurations. The mean value of the 10 measurements and error limits from the standard deviation are shown for a hexagonal lattice of sapphire rods.

In this experimental study, the fixed hole that holds a receiving antenna in the top metallic plate was also replaced with a slot (figure 5.8) that allowed the antenna to slide to arbitrary angle away from the centre of the setup. This new setup was used to investigate the effect of measuring the transmitted waves at arbitrary angles away from the  $\Gamma - K$  direction. In figure 5.9, the transmission at the Dirac point is shown to increase with increasing deviation of the receiving antenna away from the  $\Gamma - K$  direction.

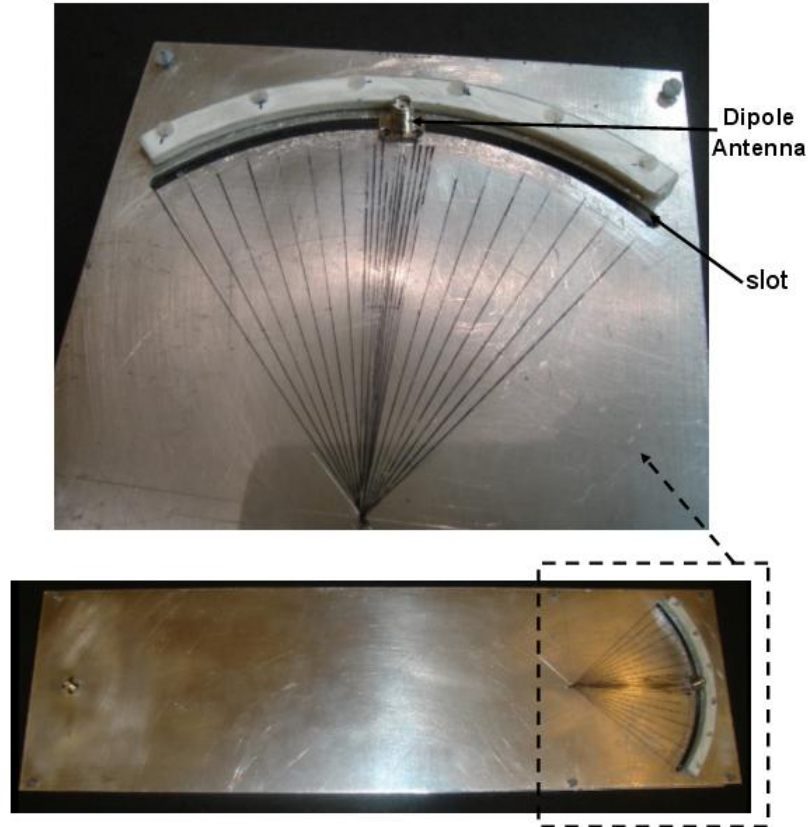


Figure 5.8: A Slot in the top plate to allow measurement of transmission at arbitrary angles.

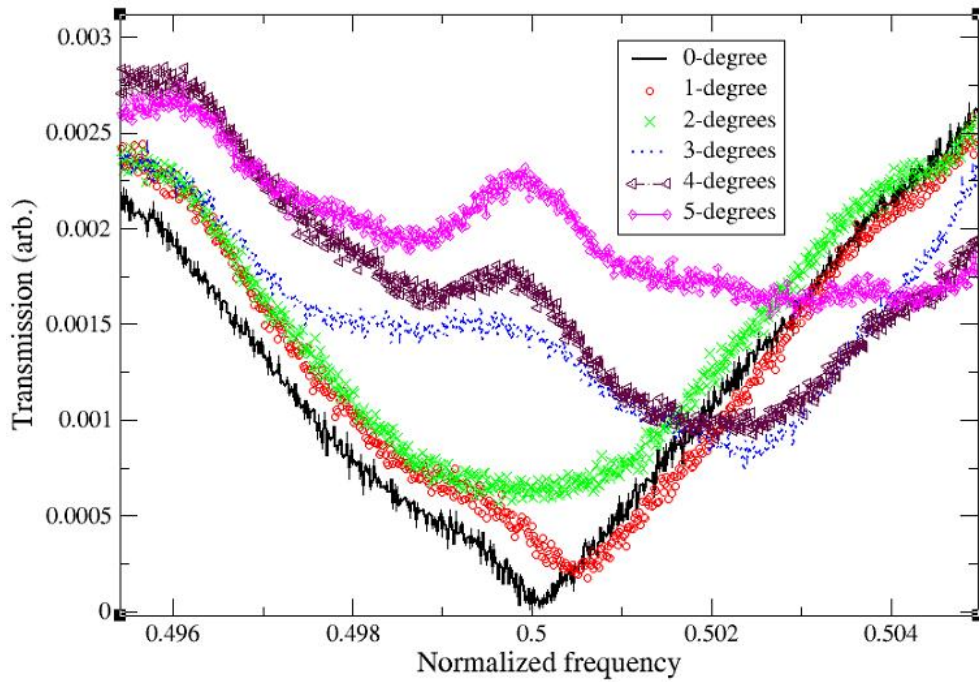


Figure 5.9: The effect of varying the measuring angle of the receiving antenna at the output boundary of a hexagonal lattice of sapphire rods on the Dirac point. The angles is taken from the  $\Gamma - K$  direction (0 degree).

The effect of varying the angle of incidence of the planewave on the photonic lattice was also studied. In this case, the transmitting and receiving antenna were fixed while the lattice was rotated. As shown in figure 5.10, the transmission at the Dirac point increased with wider angles of incidence. Considering the small ( $1^\circ$ ) steps in the variation of both incident and receiving angles, the Dirac point can be said to be sensitive to the quasi-momentum component of the EM states.

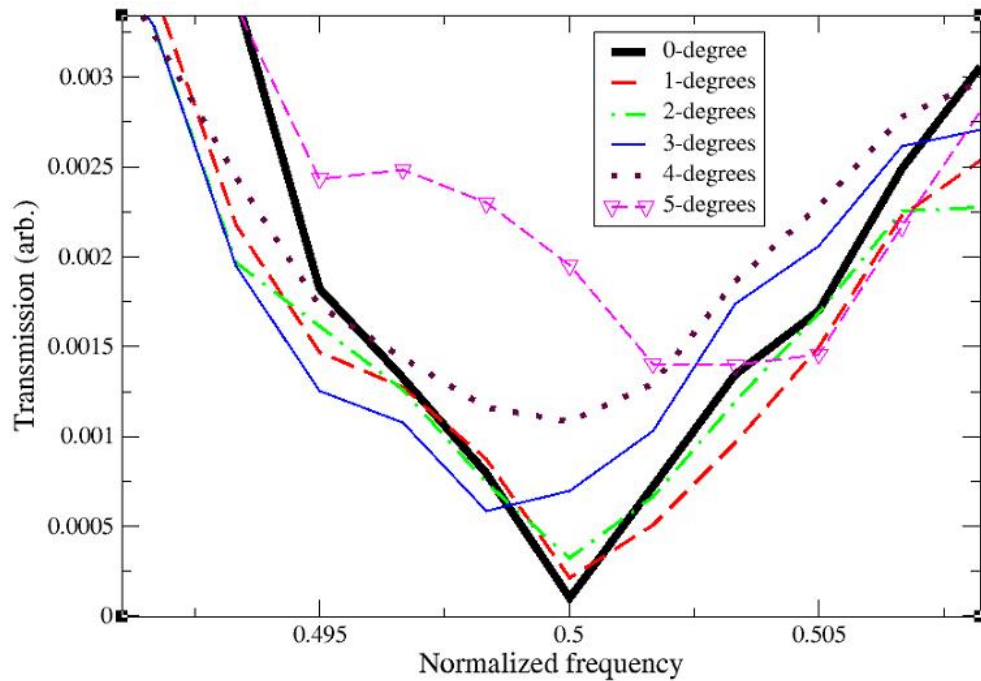


Figure 5.10: The effect of variation in the incident angle of the waves at the input boundary of a hexagonal lattice of sapphire rods on the Dirac point. The angles is taken from the  $\Gamma - K$  direction (0 degree).

## 5.5 Experimental results for a hexagonal lattice of spheres

Since atoms found in nature are usually depicted as spheres in their macroscopic geometry, a hexagonal lattice of sapphire spheres was also investigated to check if it also exhibits a Dirac point. In this case the hexagonal lattice of sapphire spheres ( $r/a = 0.2$ ) was sandwiched between top and bottom aluminum plates. The separation ( $2r = 4$  mm) between the plates allows only the propagation of EM states with Transverse Magnetic (TM) polarization with electric field perpendicular to the metallic plates. Each sapphire sphere sits on tiny (0.3 mm deep) indentations in the bottom plate. These dents prevent the spheres from rolling away from their lattice position. The position of each dent is accurate to 0.01 mm.

Again a reference measurement (shown in figure 5.11) was taken without the lattice of sapphire spheres and used to normalize the subsequent measurements taken with the lattice present. This ensures that the observed effects and phenomena are due to the lattice of sapphire spheres.

In the case of the hexagonal lattice of sapphire spheres, the position of the band gap can be seen between  $a/\lambda = 0.45$  and  $a/\lambda = 0.54$  and a sharp linear drop in transmitted EM states with a minimum at the Dirac point was found at  $a/\lambda = 0.575$ . The repeatability and the experimental error in the setup was investigated by considering 10 different ensembles of absorbers and the metallic plate positions

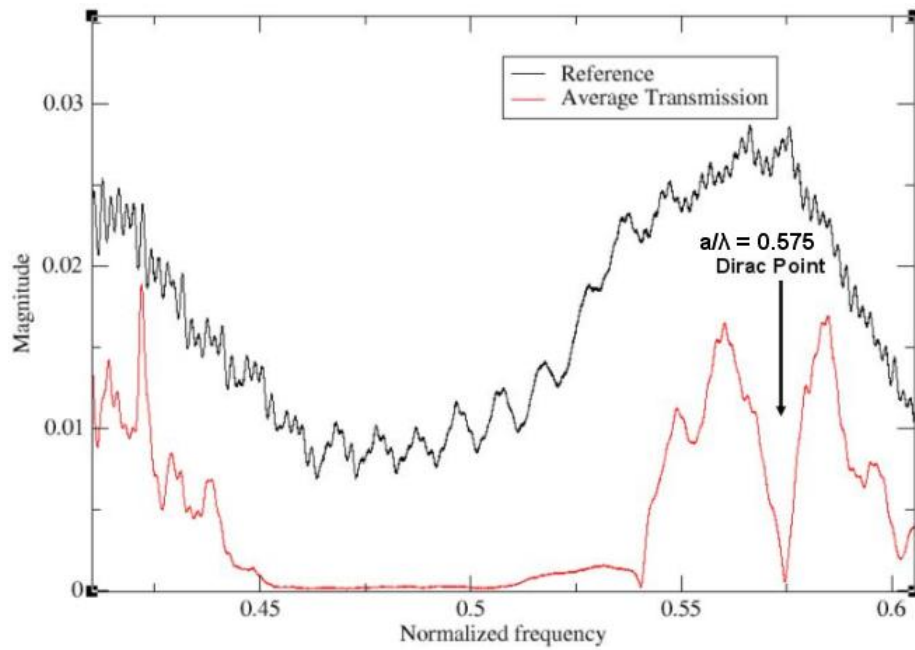


Figure 5.11: Measured transmission plot  $S_{21}$  for a planewave through a hexagonal lattice of sapphire spheres ( $\epsilon = 11$ ) with  $r/a = 0.2$ . The Dirac point seen at  $a/\lambda = 0.575$  is as a result of the lattice

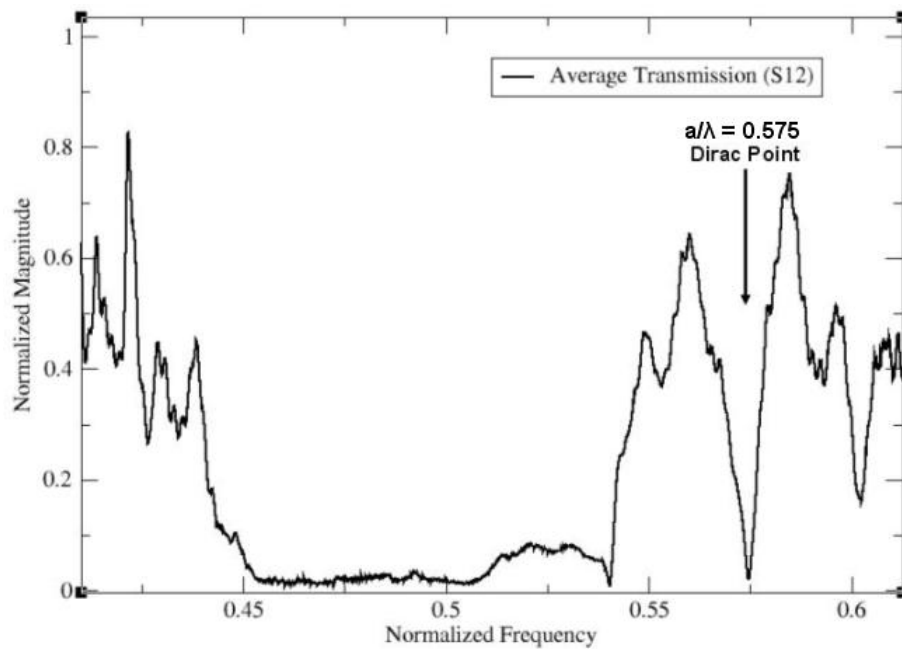


Figure 5.12: Normalized transmission plot  $S_{21}$  for a planewave through a hexagonal lattice of sapphire spheres ( $\epsilon = 11$ ) with  $r/a = 0.2$ . The Dirac point can be seen at  $a/\lambda = 0.575$

respectively. The average transmission measurement and the error limits calculated from the standard deviation is presented in figures 5.13 for absorbers and 5.14 for metallic plates.

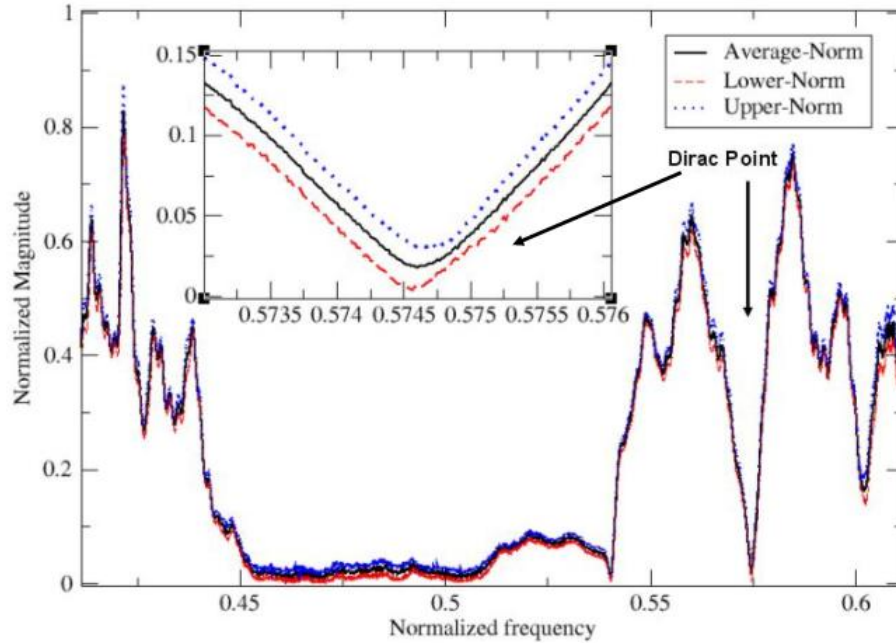


Figure 5.13: Measured transmission plot  $S_{12}$  for 10 ensembles of absorber configurations. The average and error limits are shown.

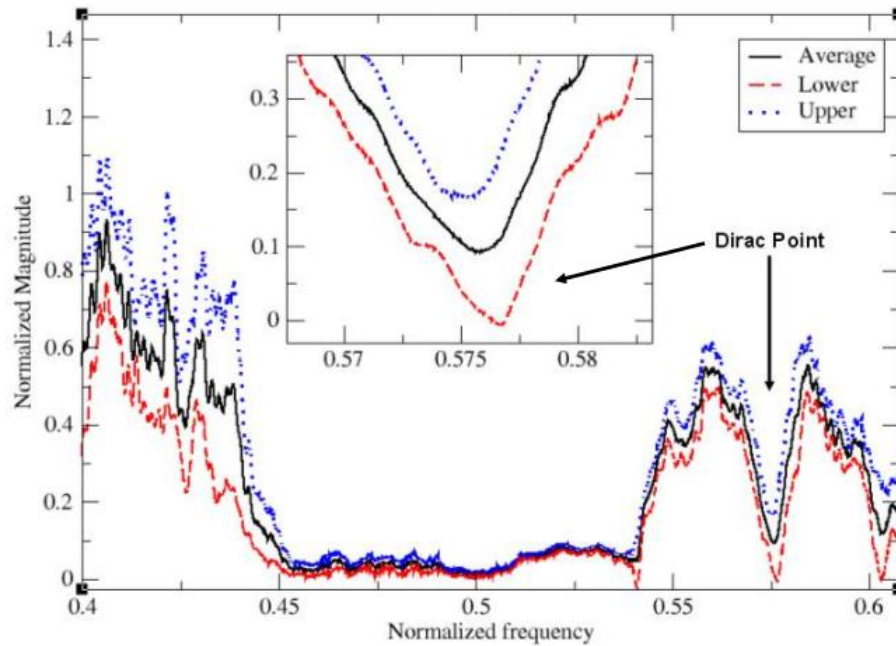


Figure 5.14: Measured transmission plot  $S_{12}$  for 10 ensembles of top plate configurations. The average and error limits are shown for a hexagonal lattice of sapphire spheres.

Also for the hexagonal lattice of sapphire spheres, the effect of variations in the incident and receiving angles of the waves at the input and output boundary of the lattice was investigated respectively. Similar to the case of the cylindrical rods, the transmitted power or the DOS at the Dirac point was found to increase as the incident and receiving angles deviates away from the  $\Gamma - K$  direction. This is shown in figures 5.15 and 5.16

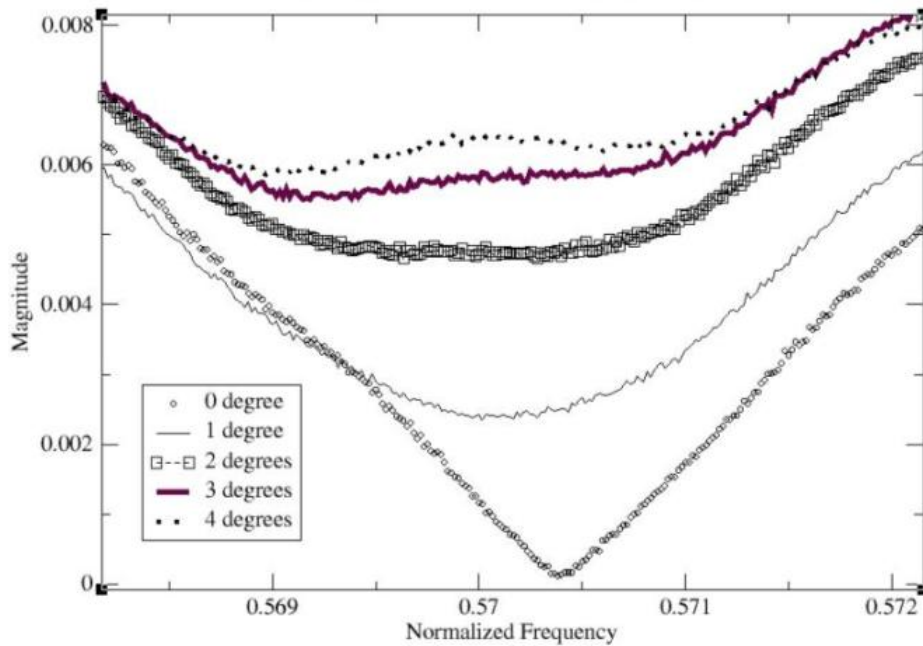


Figure 5.15: The effect of varying the measuring angle of the receiving antenna at the output boundary of a hexagonal lattice of sapphire spheres on the Dirac point. The angles is taken from the  $\Gamma - K$  direction (0 degree).

This work demonstrates, in a more pronounced way than in previous publications [48, 49], the analogy of graphene with a photonic crystal. The experimental setup used in this work is different to those of earlier [48, 49] experimental studies with particular attention paid to ensuring that the incident wave is actually a planewave and also that the EM waves seen by the receiving antenna are as close as

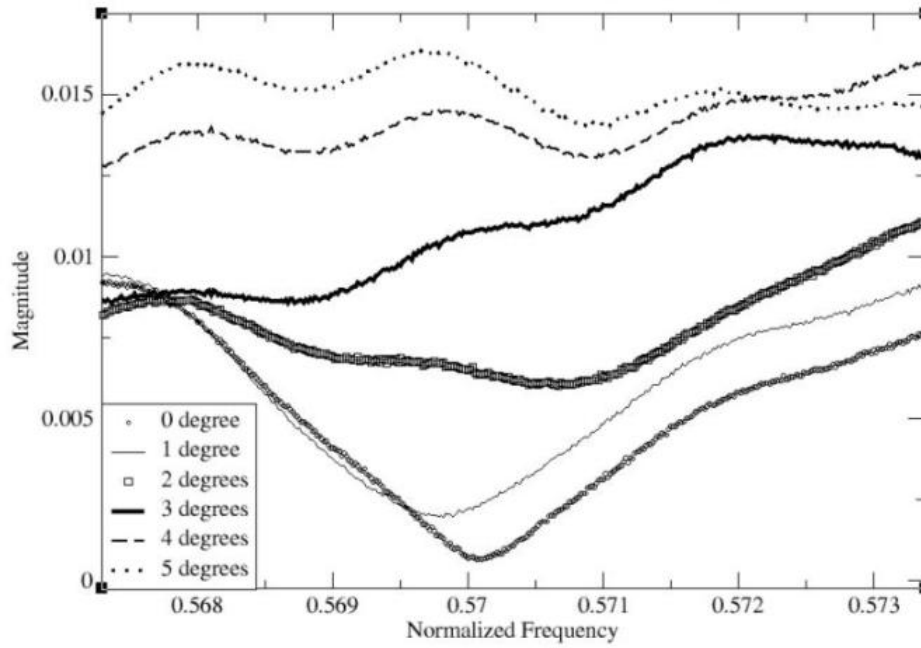


Figure 5.16: The effect of variation in the incident angle of the waves at the input boundary of a hexagonal lattice of sapphire spheres on the Dirac point. The angles is taken from the  $\Gamma - K$  direction (0 degree).

possible to the  $\Gamma - K$  direction. These are requirement theorized in [206] for the observation of the Dirac point. Also, the sensitivity of the Dirac point to incident and receiving angles away from the  $\Gamma - K$  direction was studied. As expected at the Dirac frequency, the DOS was lowest (approaching zero) in the  $\Gamma - K$  direction.

# Chapter 6

## Conclusion and looking forward

This thesis has documented how Photonic Band Gap (PBG) structures can be engineered to confine only a dipole mode while all other EM states are allowed to propagate away. This PBG structure was tuned and optimized for crabbing application at 11.9942 GHz. Also documented in this thesis is the experimental observation of the Dirac point in a 2D photonic crystal. The design of the PBG crab cavity was done numerically by using a combination of PWE, FDTD, FEM and PIC numerical methods. The PWE method was used to calculate to dispersion of several photonic crystal lattices. The eigenfrequency calculated were performed with the FDTD and the FEM methods. The FEM method was also used to calculate the scattering parameter  $S_{11}$  of the EM waves coupled into the PBG structure. A study to demonstrate the suppression of Wakefields in a PBG structure was performed with the PIC numerical method. The experimental study of the Dirac point in photonic analogue of graphene was carried out by measuring the transmission coefficient of the EM

wave propagating through a photonic crystal. Electromagnetic absorbers were used to isolate and allow only waves with wave vectors close to the  $\Gamma - K$  direction to enter into the photonic crystal. The receiving antenna in the experimental setup was also shielded by EM absorbers to ensure it sees only waves with a k-vector near K-points of symmetry in the Brillouin zone. Also the effect of variation in the experimental setup was studied by measuring the transmission plot  $S_{12}$  of 10 ensembles each for the absorber and the top plate configuration respectively. Furthermore, the effect of variations in the incident angle at the input boundary and the receiving angle at the output boundary of the PC was investigated by designing the experimental setup to allow the rotation of both the photonic crystal and the receiving antenna away from  $\Gamma - K$  direction.

In chapter 3, the work of Y. Kalra et al 2006 and R. Diana et al 2007 was extended by calculating the frequency dependent position of the global band gap with varying lattice parameters ( $r/a$  and permittivity) for dielectric photonic crystals as E. Smirnova et al 2003 did for metallic PBG structures. This study found that the size of the band gap increases with permittivity and decreases with increasing filling factor. As the filling factor of the lattice is increased, higher order band gaps are created and for a specific filling factor, the number of band gaps increases with increasing permittivity. Also in chapter 3, a study to investigate the effect of single and double point defect in a photonic crystal of dielectric rods in air found that both monopole-

like and dipole-like modes are confined in both cases. However, by varying the size of the innermost rods closest to the double point defect, the confined mode shifted up or down in frequency within the band gap. This allowed for the determination of lattice parameter (i.e. radius of innermost rods) where only the dipole is confined. Furthermore, the selective confinement of the dipole-like mode was demonstrated by increasing the number of scatterers around the defect from 4 to 10 rows. This caused the radiative quality factor of the dipole-like mode to increase by a factor of  $10^3$  while the radiative quality factor of the monopole-like mode also increased, but only by a factor of 10. This work has demonstrated a systematic approach to mode engineering within the band gap of a photonic lattice. We have designed a monomodal structure that confines only the  $TM_{011}$ -like dipole mode while allow all other modes to propagate away. A similar approach can be employed to design monomodal structures that confines only monopole, quadrupole or higher order modes.

In chapter 4, the infinite height photonic lattice designed in chapter 3 was shown to retain its selective confinement of the dipole-like mode even in the case of a finite height PBG structure. This was established by exciting a finite height PBG structure with a relativistic particle bunch and taking the fast Fourier transform of the time signal of the induced Wakefields. The contribution of the LOMs and the HOMs to the power spectrum of the Wakefields was found to drop quickly with time while the contribution from the dipole mode

drops at a much slower rate. In another study documented in chapter 4, the frequency sensitivity of the dipole mode confined by a PBG crab cavity to variations in the beam-tube radius (btr), beam-tube length (btl), and iris curvature (cc) was found to be -48 MHz/mm, 13.5 MHz/mm and -11.8 MHz/mm respectively. This shows that the PBG crab cavity design presented in chapter 4 is more robust than the conventional crab cavity presented in P. K. Ambattu et al 2005 as it offers a less tight fabrication tolerance. Also in chapter 4, the figures of merit  $\frac{R}{Q}$ ,  $\frac{E_{\perp}}{E_{peak}}$ , and  $\frac{H_{peak}}{E_{\perp}}$  were found to drop in value with an increase in the beam-tube radius. However, the  $\frac{H_{peak}}{E_{\perp}}$  value was found to oscillate as the beam-tube radius is increased. The oscillation is caused by the variation in the mesh density used for each case of beam tube radius. The mesh size changes as the lattice dimensions (innermost rod radius) was varied while keeping the frequency of the dipole mode at 11.9942 GHz. Overall, the parameters of merit of the single-cell PBG crab cavity designed in this work compares well with those presented for multi-celled travelling wave crab cavity in P. K. Ambattu et al 2005.

Using an antenna that is 7 mm deep inside the PBG crab cavity, electromagnetic energy was coupled into the structure with  $S_{11} = 0.05$  for the dipole mode. Also a waveguide coupling scheme was presented where EM power was transferred to the dipole mode with  $S_{11} = 0.0279$ . A final single cell design with lattice constant (a=11.89 mm), bulk lattice rod radius (r=1.189 mm), innermost rod radius

( $R = 1.471$  mm), beam-tube radius (btr=5 mm), beam-tube length (btl=10 mm), iris curvature (cc=1 mm) and cavity height of 12.5 mm was chosen and analyzed. The calculated parameters of merit of the PBG crab cavity design include  $\frac{R}{Q} = 13.1\Omega$ ,  $Q_0 = 18046$ ,  $\frac{E_{\perp}}{E_{peak}} = 0.149$ , and  $\frac{H_{peak}}{E_{\perp}} = 0.006A/V$ . For an input power of 1 Watt, the transverse voltage and deflecting gradient was calculated to be 485.6 V and 15 kV/m respectively. This PBG crab cavity design was considered for application in the CLIC facility that requires a maximum transverse kick voltage of 2.4 MV to rotate a 1.5 TeV beam by 20 mrad. However, the use of the PBG crab cavity (made of alumina rods in air) for crabbing application in the CLIC facility is limited by breakdown in the dielectric material. The field distribution of the dipole mode shows that the innermost rod closest to the double point defect is exposed to much higher electric field than the rods that make up the bulk lattice. In order to ensure that the electric field experienced by the innermost rods does not exceed the DC breakdown value (13.4 MV/m) for alumina, a multi-cell PBG crab cavity design was considered. In the first scenario considered, the multi-cell design assumes that each constituent cell has the same parameters of merit as the optimized single-cell PBG crab cavity. A 0.515 m long PBG structure with 41 cells will be required to deliver the 2.4 MV transverse kick needed by the CLIC facility. The second scenario considered the case of an infinitely periodic PBG crab cavity with  $\pi$  phase advance and cell-to-cell coupling. In this second case, a

0.202 m long PBG structure with 16 cells will be required to deliver the 2.4 MV transverse kick needed by the CLIC facility. The result of the second scenario is more believable as it accounts for the phase advance between the cavity cell and the inter-cavity coupling. When the EM wave coupling and the beam loading effect are considered, a calculated total input power of 8.46MW is required for the 16 cell PBG crab cavity to deliver a transverse kick of 2.4MV. This means that each cavity cell requires only 528 kW of power. Operational issues such as the damping of the parasitic modes on the boundary of the lattice, the cooling of the metallic plates, and the eventual fabrication of the PBG structure have been addressed in this chapter. The PBG crab cavity design employed a tapered block of silicon carbide (SiC) to dissipate the EM power of parasitic LOM and HOMs. The pulse heating on the iris of the metallic plates where the peak magnetic field is concentrated was calculated to cause a maximum increase in temperature of  $6^{\circ}C$ . The PBG crab cavity design adopted the water cooling approach to transfer heat energy away from the metallic plates. Finally, chapter 4 presents a fabrication approach where the dielectric rods are pressed into small holes in the metallic plates. The dimensions of individual component parts as well as the assemblage of the complete crabbing system are presented.

In chapter 5, the exhibition of the Dirac point in the dispersion plot of photonic crystals was experimentally investigated. This study was based on the theoretical approach presented in R. A. Sepkhanov

et al 2006 where the photonic crystal is considered as a system with the input and output EM wave signal related by a total systemic transfer matrix. As suggested by Sepkhanov et al, the experimental setup was designed to improve the matching of the wave vectors at the boundaries of the photonic crystal. This was done by shielding off EM waves with k-vector that are away from the  $\Gamma - K$  direction. The experiment was performed by sending a planewave into the photonic crystal and then measuring on a network analyzer, the scattering parameter  $S_{21}$  of the EM wave seen by the receiving antenna. Close to the Dirac point on the PWE numerically calculated dispersion plot, the experimentally measured transmission coefficient  $S_{21}$  drops linearly toward zero. This indicates a linear drop in the DOS as the Dirac point is approached. This phenomenon was found for both hexagonal lattices of sapphire rods and spheres. The observed Dirac point is more pronounced than those presented in Zandbergen and de Dood 2010 and S. Bittner et al 2010. Furthermore, the Dirac point was found to be sensitive to variations in both the incident and the receiving angle at which the EM waves enter and exit the photonic crystal respectively. The transmission coefficient at the Dirac point increased considerably for a small ( $1^\circ$ ) deviation in the incident and receiving angle away from the  $\Gamma - K$  direction of the photonic in real space. Overall, the findings of this study supports and reinforces the idea that quantum mechanical effects, which are usually found in natural crystals, can easily be investigated in a man-made pho-

tonic crystal and at a macroscopic length scale. Also in chapter 5, a theoretical method of retrieving the propagation constant of EM waves propagating through a PC lattice is presented. However, the difficulties associated with the calibration of the experimental setup inhibit the application of this transmission line theory based parameter retrieval method to obtaining experimentally the dispersion plot of a photonic crystal. The calibration method used is quite sensitive to tiny experimental errors and this causes the retrieval of the impedance  $z$  and the propagation constant to fail. This work can serve as a guide to future attempts at obtaining the dispersion of photonic crystal structures experimentally.

For future work on the PBG crab cavity, I recommend the fabrication and cold testing of the single-cell PBG crab cavity presented in this thesis. Also in the long term, I recommend the fabrication and hot testing of a multi-cell PBG crab cavity made from sapphire or other dielectric materials with higher breakdown values. Future studies planned for the photonic analogue of graphene include an investigation of edge effects for both zig-zag and armchair interfaces and a study of the Local Density Of States (LDOS) within the photonic lattice. Also, the effect of disorder on the transmission of EM waves at the Dirac point can be studied.

# Appendix A

## Hermitian operators and their properties

The operators in the wave equations (2.12) and (2.13), also presented in this appendix as equations (A.1) and (A.2), are linear hermitian operators [43].

$$\nabla \times \frac{1}{\mu} \nabla \times \vec{E}(\vec{x}, t) = \omega^2 \varepsilon \vec{E}(\vec{x}, t) \quad (\text{A.1})$$

$$\nabla \times \frac{1}{\varepsilon} \nabla \times \vec{H}(\vec{x}, t) = \omega^2 \mu \vec{H}(\vec{x}, t) \quad (\text{A.2})$$

An operator is hermitian if it satisfies the symmetry that allows the inner product of two vector fields  $\vec{A}$  and  $\vec{B}$  to meet the following condition:

$$[\vec{A}, \Psi \vec{B}] = [\Psi \vec{A}, \vec{B}] \quad (\text{A.3})$$

Where  $\Psi$  is the Hermitian operator. The result of the inner product is independent of the vector field initially operated upon by the

symmetric hermitian operator. Hermitian operators always have real eigenvalues and orthogonal eigenvectors. For clarity, the inner product is a way of multiplying two vectors to obtain a scalar. It is a generalization of the dot product and can be defined as follows:

$$[\vec{A}(x), \vec{B}(x)] = \iiint \vec{A}(x)^* \cdot \vec{B}(x) d^3x \quad (\text{A.4})$$

Where  $*$  denotes the complex conjugate of a vector. The hermitian nature of the eigenoperator in equation (A.1) can be proved as follows:

$$[\vec{A}, \Psi \vec{B}] = \iiint \vec{A}(\vec{x})^* \cdot \nabla \times \frac{1}{\mu} \nabla \times \vec{B}(\vec{x}) \quad d^3\vec{x} \quad (\text{A.5})$$

$$= \iiint (\nabla \times \vec{A}(\vec{x}))^* \cdot \frac{1}{\mu} \nabla \times \vec{B}(\vec{x}) \quad d^3\vec{x} \quad (\text{A.6})$$

$$= \iiint [\nabla \times (\frac{1}{\mu} \nabla \times \vec{A}(\vec{x}))]^* \cdot \vec{B}(\vec{x}) \quad d^3\vec{x} \quad (\text{A.7})$$

$$= [\Psi \vec{A}, \vec{B}] \quad (\text{A.8})$$

The surface terms of the integration by parts were neglected because the vector fields are periodic in the region of integration or decay to zero with large distance [43]. From the proof of equation (A.8), the eigenvectors of equation (A.1) are orthogonal and the eigenvalues are real and non-negative. Equation (A.1) can be re-written as follows:

$$\Psi \vec{E} = \omega^2 \epsilon \vec{E} \quad (\text{A.9})$$

Consider the inner product of two vector field  $\vec{E}_1$  and  $\vec{E}_2$  with frequencies  $\omega_1$  and  $\omega_2$  respectively.

$$[\vec{E}_1, \Psi \vec{E}_2] = [\Psi \vec{E}_1, \vec{E}_2] \quad (\text{A.10})$$

The conjugate symmetrical identity of the inner product can be written as:

$$[\vec{E}_1, \Psi \vec{E}_2] = [\Psi \vec{E}_1, \vec{E}_2]^* \quad (\text{A.11})$$

Therefore

$$[\Psi \vec{E}_1, \vec{E}_1] = (\omega_1^2 \varepsilon) [\vec{E}_1, \vec{E}_1] = (\omega_1^2 \varepsilon)^* [\vec{E}_1, \vec{E}_1] = [\Psi \vec{E}_1, \vec{E}_1]^* \quad (\text{A.12})$$

If  $\omega_1^2 = \omega_1^{2*}$ , then  $\omega_1^2$  is real. Also, the following equation shows orthogonality and degeneracy.

$$[\Psi \vec{E}_1, \vec{E}_2] = (\omega_1^2 \varepsilon) [\vec{E}_1, \vec{E}_2] = (\omega_2^2 \varepsilon) [\vec{E}_1, \vec{E}_2] = [\vec{E}_1, \Psi \vec{E}_2] \quad (\text{A.13})$$

$$(\omega_1^2 - \omega_2^2) [\vec{E}_1, \vec{E}_2] = 0 \quad (\text{A.14})$$

In order to satisfy equation (A.14), a case when  $\omega_1 \neq \omega_2$  will require  $[\vec{E}_1, \vec{E}_2] = 0$ . In this case, the vector fields  $\vec{E}_1$  and  $\vec{E}_2$  are said to be orthogonal. On the other hand, when  $\omega_1 = \omega_2$ , the vector fields are said to be degenerate.

# Appendix B

## Wakefields and the Panofsky-Wenzel theorem

### B.1 Introduction

The understanding of how particle beams interact with the surroundings (beam tube and RF cavity) and the effect of the associated electromagnetic fields are important for the optimization of the accelerator performance in terms of stored current [217]. This appendix gives a basic introduction to the subject of Wakefield and the Panofsky-Wenzel theorem. A more detailed discussion can be found in [217, 218]. The electromagnetic field distribution of a ultra-relativistic ( $\frac{v}{c} = \beta \approx 1$ ) point charge in free space is isotropic and squeezed in the longitudinal direction. In this case, there is zero power transfer in the transverse direction but there exist a poynting flux that is attached to the point charge and flow along a parallel path. A test charge travelling at a distance behind an excitation charge does not experience any wakefield in free space [220]. The EM

field associated with a ultra-relativistic point charge travelling in a hollow cylindrical beam tube which has perfectly conducting walls is similar to those obtained in free space [220] and a trailing test charge does not experience any wakefield. In this case, an image charge is induced on the wall of the beam tube and they have trajectories that are parallel to that of the point charge. However, when the beam tube is lossy and/or has discontinuities (e.g. RF cavities), the image charges begins to lag behind the point charge. The field excited by these image charges are called Wakefield and can adversely affect the trajectory of charged particles within the same bunch (short range Wake) and those from later bunches (long range Wake).

## B.2 Longitudinal wake function and loss factor

In this section, the expressions for the wake function and loss factor were initially published in Palumbo et al [217]. Let's consider an excitation point charge travelling through a RF cavity in the direction the Z-axis (at position  $z_1$ ) with a constant velocity ( $v = \beta c$ ) and a transverse offset  $r_1$  away from the axis. As illustrated in figure C.1, the excitation charge is followed at a distance  $s$  by a test charge in the longitudinal and transverse positions  $z$  and  $r$  respectively. The Lorentz force imparted on  $q$  by the EM fields excited by  $q_1$  is given as:

$$F(r, z, r_1, z_1; t) = q[E(r, z, r_1, z_1; t) + v \times B(r, z, r_1, z_1; t)] \quad (\text{B.1})$$

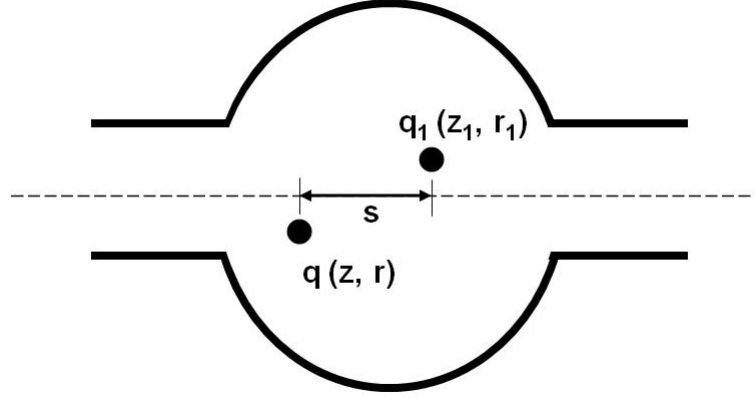


Figure B.1: The excitation  $q_1$  and test  $q$  charges travelling in a spherical RF cavity.

The work done by the longitudinal component of the electromagnetic force  $F_z = qE_z$  can be used to calculate the energy lost by  $q_1$  as follows:

$$U_{11}(r_1) = - \int_{-\infty}^{\infty} F(r_1, z_1, r_1, z_1; t = \frac{z_1}{v}) \cdot dz \quad (\text{B.2})$$

The energy change of the test charge of the test charge as a result of the field excited by  $q_1$  is given as:

$$U_{21}(r, r_1, \tau) = - \int_{-\infty}^{\infty} F(r, z, r_1, z_1; t = \frac{z_1}{v} + \tau) \cdot dz \quad (\text{B.3})$$

$\tau$  is the time delay between the excitation and the test charges. Unlike the case in equations B.2 and B.3 where the integral is over an infinite length, physical accelerating structures and crab cavities

are finite in length. Therefore, the integrals of equations B.2 and B.3 can be truncated to give a good approximation of the energy as long as the EM fields are confined to a given region and evanescent everywhere else. The longitudinal wake function  $w_z(r, r_1, \tau)$  can be expressed as the energy lost by the test charge  $q$  per unit of both charges  $q$  and  $q_1$  [220, 221, 222].

$$w_z(r, r_1, \tau) = \frac{U_{21}(r, r_1, \tau)}{q_1 q} \quad [V/C] \quad (\text{B.4})$$

Often the practical quantity of interest (especially in periodic structure) is the wake per unit length which is measured in unit of V/C/m and given as:

$$\frac{d}{dz} w_z(r, r_1, \tau) = -\frac{1}{q_1 q} F_z(r, z, r_1, z_1; t); \quad z = z_1 - v\tau \quad [V/C/m] \quad (\text{B.5})$$

The loss factor  $k$  is the energy lost by  $q_1$  per unit charge squared and is given as:

$$k(r_1) = \frac{U_{11}(r_1)}{q_1^2} \quad [V/C] \quad (\text{B.6})$$

Equations B.4, B.5, and B.6 have considered the wake excited by point charge. The point charge wake is a green's function and its convolution over the charge distribution  $i_b$  of a bunch gives the wake function of the bunch as:

$$W_z(r, \tau) = \frac{U(r, \tau)}{q_1 q} = \frac{1}{q_1} \int_{-\infty}^{\infty} i_b(\tau') w_z(r, \tau - \tau') d\tau' \quad (\text{B.7})$$

The convolution integral is obtained by applying the superposition principle where the wake functions of infinite number of infinitesimal slices are added up.  $\tau'$  is the time delay between each slice and the test charge. Also the loss factor of the charge distribution is given as :

$$K(r) = \frac{U(r)}{q_1^2} = \frac{1}{q_1} \int_{-\infty}^{\infty} i_b(\tau) W_z(r, \tau) d\tau \quad (\text{B.8})$$

### B.3 Transverse wake function and loss factor

The transverse momentum kick experience by the test charge  $q$  can be calculated from the transverse component of the Lorentz force as follows:

$$M_{21}(r, r_1; \tau) = \int_{-\infty}^{\infty} F_{\perp}(r, z, r_1, z_1; t = \frac{z_1}{v} + \tau) \cdot dz \quad (\text{B.9})$$

The unit of  $M_{21}$  is in Nm and it depends on the transverse position of the charges and the geometry of the beam tube or cavity. The transverse wake function is the transverse kick imparted on charge  $q$  per unit charge of both  $q$  and  $q_1$ .

$$w_{\perp}(r, r_1, \tau) = \frac{M_{21}(r, r_1, \tau)}{q_1 q} \quad [V/C] \quad (\text{B.10})$$

In the case of ultra relativistic charges, the dipole component of the transverse kick is the dominant term and depends on the transverse displacement of the excitation charge  $q_1$ . The wake per unit of the transverse displacement is given as:

$$w'_{\perp}(r, r_1, \tau) = \frac{w_{\perp}(r, r_1, \tau)}{r_1} \quad [V/C/m] \quad (\text{B.11})$$

The dipole transverse loss factor can be defined as the amplitude of the transverse momentum kick experienced by the charge  $q_1$  by its own wake per unit charge.

$$k_{\perp}(r_1) = \frac{M_{11}(r_1)}{q_1^2} \quad [V/C] \quad (\text{B.12})$$

The loss factor per unit displacement is given as:

$$k'_{\perp}(r_1) = \frac{M_{11}(r_1)}{q_1^2 r_1} \quad [V/C] \quad (\text{B.13})$$

In a similar way to the longitudinal wake of a bunch, the transverse wake function of the bunch is given as:

$$W_{\perp}(r; \tau) = \frac{1}{q_1} \int_{-\infty}^{\infty} i_b(\tau') w_{\perp}(r; \tau - \tau') d\tau' \quad (\text{B.14})$$

The loss factor of the bunch in V/C is given as:

$$K_{\perp}(r) = \frac{1}{q_1} \int_{-\infty}^{\infty} i_b(\tau) W_{\perp}(r, \tau) d\tau \quad (\text{B.15})$$

As in the case of the point charges, the transverse wake function and the loss factor per unit displacement is given as:

$$W'_{\perp}(r; \tau) = \frac{W_{\perp}(r; \tau)}{r} \quad [V/C/m] \quad (\text{B.16})$$

$$K'_{\perp}(r) = \frac{K_{\perp}(r)}{r} \quad [V/C/m] \quad (\text{B.17})$$

## B.4 The Panofsky-Wenzel theorem

In this section, a relationship between the longitudinal and transverse wake function is presented. The detailed derivations presented in [170] concludes that the longitudinal derivatives of the transverse wake functions is equal to the transverse gradient of the longitudinal wake function. This is the Panofsky-Wenzel theorem and it is given as:

$$\frac{\partial \vec{W}_{\perp}}{\partial s} = \vec{\nabla}_{\perp} W_z \quad (\text{B.18})$$

## Appendix C

# Experimental measurement of the dispersion of a PC lattice

In many publications the dispersion of PC lattices are calculated either analytically [211] or numerically [43, 72]. The results of this dispersion calculation are usually verified experimentally by comparing them to the amplitude of the transmission and reflection scattering parameters obtained from Vector Network Analyzers (VNA). While the experimental scattering parameters indicate the density of states at any particular frequency, they do not suggest the direction of the wave vector of an individual EM state propagating through the PC lattice. To my best knowledge, the dispersion of photonic crystals has not been retrieved directly from experimentally obtained scattering parameters. The aim of this section is to obtain the photonic band diagram of a PC lattice experimentally by employing the parameter retrieval approach presented in [212] for calculating the effective refractive index  $n$ , the impedance  $z$ , the permeability  $\mu$  and permittivity  $\varepsilon$ . The aim of this work is to compare the experimen-

tally obtained dispersion to the numerical dispersion calculated with the PWE approach. The difficulties that inhibit the realization of the above stated aims are also discussed in the section.

## C.1 Theoretical retrieval of the propagation constant

In section 5.1, the transmission of EM waves through a PC lattice was analyzed by considering it as a system with input and output signals. Here in this section, the propagation of EM waves through a PC lattice will be analyzed by considering the PC lattice as a load on a transmission line as shown in figure C.1.

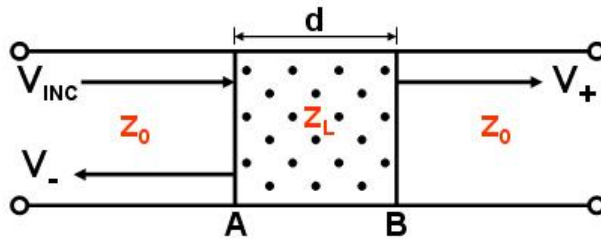


Figure C.1: A transmission line with a load having an impedance  $z_L$ . The characteristic impedance of the transmission line is  $z_0$ .  $V_{INC}$ ,  $V_-$ , and  $V_+$  are incident, reflected and transmitted EM fields with respect to the load respectively.

A transmission line is any medium through which an electromagnetic (EM) field is allowed to propagate. The fields can be considered as a voltage  $V$  that causes a current  $I$  to flow through the transmission line. When a load (in this case a PC lattice) is placed along a transmission line, the current  $I$  sees a load impedance  $z_L$  which is different from the characteristic impedance  $z_0$  of the transmission line. At the interface between the transmission line and the load,

part of the incident voltage  $V_{inc}$  is reflected back as  $V_-$  while the rest is transmitted as  $V_+$  through the interface. The reflection coefficient  $\Gamma$  which is the ratio of  $V_-$  to  $V_{inc}$  at the interface  $A$  in figure C.1 is related to the impedances on the transmission line as [213] :-

$$\Gamma = \frac{V_-}{V_{inc}} = \frac{z_L - z_0}{z_L + z_0} \quad (C.1)$$

Also for a finite  $d$ , the transmission coefficient  $T$  which is the ratio of  $V^+$  to  $V_{inc}$  between the interfaces  $A$  and  $B$  in figure C.1 is given as [213]:-

$$T = \frac{V_+}{V_{inc}} = e^{i\gamma d} \quad (C.2)$$

$\gamma = \alpha + i\beta$  is the complex propagation constant that indicates the variation in the amplitude of the incident wave as it travels in a given direction.  $\alpha$  and  $\beta$  are the attenuation constant and the phase constant respectively. In [212, 213], a relationship between the scattering parameters  $S_{11}$  and  $S_{21}$  and the transmission and reflection coefficient  $\Gamma$  and  $T$  was derived by considering the transfer function at interfaces  $A$  and  $B$  in figure C.1. These relationships are given as:-

$$S_{11} = \frac{\Gamma(1 - T^2)}{1 - \Gamma^2 T^2} = \frac{\frac{z_L - 1}{z_L + 1} (1 - e^{i2\gamma d})}{1 - \left(\frac{z_L - 1}{z_L + 1}\right)^2 e^{i2\gamma d}} \quad (C.3)$$

$$S_{21} = \frac{(1 - \Gamma^2)T}{1 - \Gamma^2 T^2} = \frac{\left[1 - \left(\frac{z_L - 1}{z_L + 1}\right)^2\right] e^{i\gamma d}}{1 - \left(\frac{z_L - 1}{z_L + 1}\right)^2 e^{i2\gamma d}} \quad (\text{C.4})$$

As shown in [214, 215], equation C.3 and C.4 can be inverted to obtain  $z_L$  and  $\gamma$  as follows:-

$$Z_L = \pm \sqrt{\frac{(1 + S_{11})^2 - S_{21}^2}{(1 - S_{11})^2 - S_{21}^2}} \quad (\text{C.5})$$

$$e^{i\gamma d} = \frac{S_{21}}{1 - S_{11} \left(\frac{z_L - 1}{z_L + 1}\right)} \quad (\text{C.6})$$

$$\gamma = \frac{1}{d} \ln \left[ \frac{S_{21}}{1 - S_{11} \left(\frac{z_L - 1}{z_L + 1}\right)} \right] \quad (\text{C.7})$$

$$\gamma(\omega) = \alpha(\omega) + i\beta(\omega) \quad (\text{C.8})$$

Once the propagation constant  $\gamma$  is determined from equation C.7, the attenuation constant  $\alpha$  of the PC lattice and the phase constant  $\beta = \frac{2\pi}{\lambda} = k$  can be determined from the real and imaginary part of the complex propagation constant [216].  $k$  is the wave number of the EM waves propagating through the medium. When the medium being investigated is not homogenous (i.e. photonic crystals), it is important to determine the boundaries of the medium and to ensure that the experimental scattering parameter is noise free [212]. The parameter retrieval method fails when the two conditions mentioned

above are not satisfied. The reason for these conditions is because of the dependence of  $\Gamma$  and  $T$  on the position of the boundaries and the thickness of the medium respectively. In [212], an optimized method of effective boundary determination was presented and the boundaries of many periodic media were found to coincide with the boundary of the first and the last unit cells at the beginning and the end of the periodic media. However, the optimization method presented in [212] depends on the accurate retrieval of the impedance of the effective medium at different thickness. This approach requires the accurate measurement of the amplitude and the phase of the scattering parameter with minimal noise. In order to obtain accurate measurement of the scattering parameters, the experimental setup needs to be properly calibrated to take into account all the losses (in the EM wave absorbers and the metallic plates) in the setup so that  $S_{11} = 0$  and  $S_{21} = 1$  when the PC lattice is not present in the experimental setup. The calibration is important because it ensures that the retrieved attenuation  $\alpha$  and the wave vector  $k$  from the experimental data are as a result of the photonic crystal. The calibration procedure is outlined in appendix D.

## C.2 The calibration result

The calibration result for the magnitude and the phase of the scattering parameters are presented in figures C.2 and C.3 where the magnitude of the  $S_{11}$  and  $S_{21}$  are close to 0 and 1 respectively. However,

the spikes in the  $S_{11}$  and  $S_{21}$  measurement plots are points where the calibration has failed. Some of the spikes are about hundred times the expected value of  $S_{21} = 1$ .

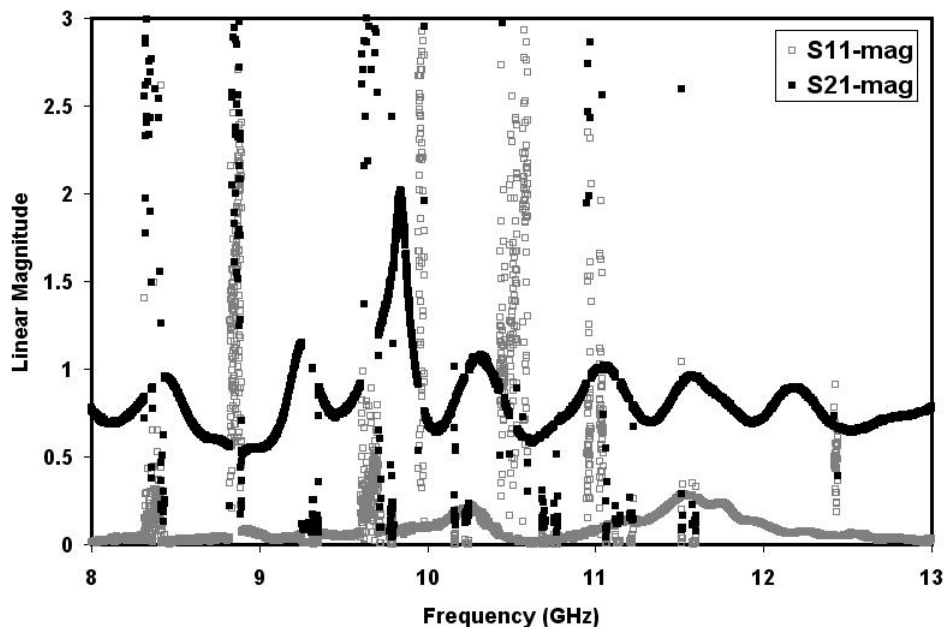


Figure C.2: The magnitude of the scattering parameter  $S_{11}$  and  $S_{21}$  measured after the calibration of the experimental setup.

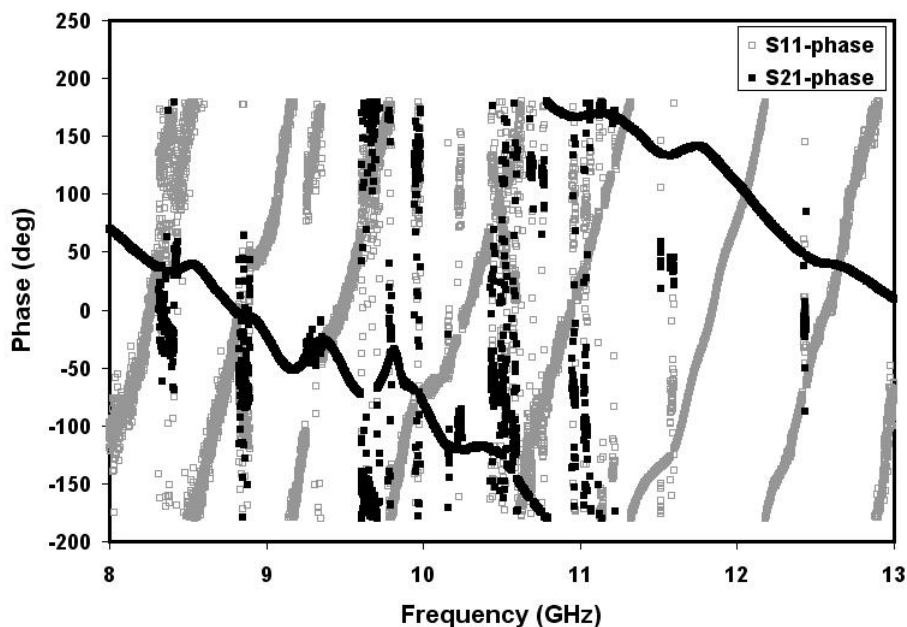


Figure C.3: The phase (in degrees) of the scattering parameter  $S_{11}$  and  $S_{21}$  measured after the calibration of the experimental setup.

There are two main problems with the calibration result presented

in figure C.2. The first problem is the discrepancies between the measured  $S_{11}$  and  $S_{21}$  and the expected values of  $S_{11} = 0$  and  $S_{21} = 1$ . For most of the frequencies considered in figure C.2, the  $S_{21}$  values oscillate about 0.8 while the  $S_{11}$  values are about 0.08. This type of error is expected although it is desirable to minimize these discrepancies in the  $S_{11}$  and  $S_{21}$  values. These amplitude related errors are caused by the losses in the experimental setup which are not properly normalized out by the calibration process. During the *line* measurement in the calibration procedure, the impedance of the EM wave absorber may be matched to the characteristic impedance of the transmission line and therefore the load reflection coefficient  $\Gamma \neq 0$ . Also during the *reflection* measurement in the calibration procedure, the load impedance of the metal block is not zero (i.e  $z_L \neq 0$ ) hence the reflection coefficient  $\Gamma \neq -1$  as expected in the case of a short circuit. These impedance mismatches are possible points of amplitude related errors in the calibration.

The second case of discrepancies are the spikes found at some frequencies in the  $S_{11}$  and  $S_{21}$  plots. This spikes occurs when the  $\Gamma^2 T^2$  term in the determination of equation C.3 and C.4 tends towards unity. This causes the denominators in the expression for  $S_{11}$  and  $S_{21}$  to approach zero hence causing  $S_{11}$  and  $S_{21}$  hence causing the  $S_{11}$  and  $S_{21}$  values to be much higher than unity. The amplitude of these spikes changes with small variation in the top metallic plate. This suggests that the calibration method used is quite sensitive to

tiny experimental errors in the positioning of the top plate during the *reflection, line* and *thru* measurement in the calibration process. As mentioned in [212], discrepancies in the  $S_{11}$  and  $S_{21}$  measurement will cause the retrieval of the impedance  $z$  and the propagation constant to fail. These discrepancies can be minimized in future work by ensuring that the experimental setup has very few moving parts which can contribute to the impedance mismatch at each stage in the calibration process.

In this section, a theoretical method of retrieving the propagation constant of EM waves propagating through a PC lattice was presented. However, the difficulties associated with the calibration of the experimental setup inhibit the application of this transmission line theory based parameter retrieval method to obtaining experimentally the dispersion plot of a photonic crystal. This work discusses these difficulties and can serve as a guide to future attempt at obtaining the dispersion of photonic crystal experimentally.

# Appendix D

## The calibration procedure

The experimental set up used in this study is similar to the one shown in figure 5.2 of chapter 5 where a plane wave, created by using EM waves absorbing side boundaries, is allowed to propagate through a periodic medium. In this case the dipole antennas are replaced with two X-band SMA to waveguide couplers that are connected to a Vector Network Analyzer (VNA) as illustrated in figure 5.18.

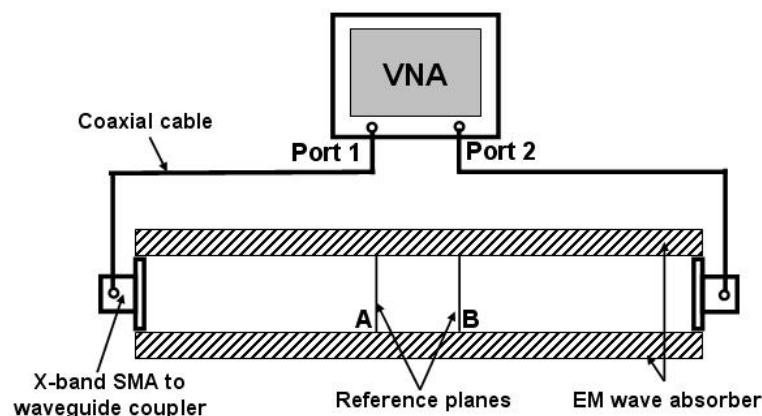


Figure D.1: An illustration of the experimental setup to be calibrated. Not shown in this illustration are 2 aluminium plates placed on the top and at the bottom of the space between the EM wave absorbers.

The calibration tools used include a block of metal that is exactly the height of the EM wave absorbers (10mm) which was used to

create a short circuit and a block of EM waves absorber that covers the space between the reference points  $A$  and  $B$  shown in figure 5.18. The EM absorber was used as a matched load with no reflection ( $\Gamma = 0$ ). Once the experimental setup is connected as shown in figure 5.18 with the top and bottom aluminum plates in place, the calibration process proceeded as follows:-

- On the VNA, the frequency range (8GHz - 13GHz) of interest was selected.
- A calibration kit was created, named and saved on the VNA. The calibration kit stores the frequency range for the *short* ( $\Gamma = 1$ ), *matched load* ( $\Gamma = 0$ ) and *thru* ( $T = 1$ ) measurements as well as the time delay  $t_1$  in picoseconds for the *thru* measurement between the reference points A and B in figure 5.18. The time delay was calculated by normalizing phase delay  $\theta = \beta_0 L$  and then relate it to the period  $T_c$  of the center frequency ( $f = 10.5GHz, \lambda = 0.0286m$ ). For a distance of  $L = 0.07m$  between the reference points A and B, the time delay  $t_1$  as follows:-

$$\beta_0 = \frac{2\pi}{\lambda} = \frac{2\pi}{0.0286} = 219.9rad/m \quad (D.1)$$

$$\theta = \beta_0 L = 219.9 \times 0.07 = 15.39rad \quad (D.2)$$

$$T_c = \frac{1}{f} = \frac{1}{10.5 \times 10^9} = 95.24ps \quad (D.3)$$

$$\frac{\theta}{2\pi} = \frac{t_1}{T_c} \quad (\text{D.4})$$

$$t_1 = \frac{\theta T_c}{2\pi} = \frac{15.39 \times 95.24 \times 10^{12}}{2\pi} = 233.28 \text{ps} \quad (\text{D.5})$$

- Launch the calibration wizard on the VNA and specify the class of calibration to be TRL between port 1 and 2. Select the reflection standard and the system impedance. The calibration wizard will give the option to perform the *reflection* ( $\Gamma = 1$ ) and *line* ( $\Gamma = 0$ ) measurements from port 1, a *thru* ( $z_L = 0$ ) between ports 1 and 2 and then the *reflection* measurement from port 2 as illustrated in figure 5.19.

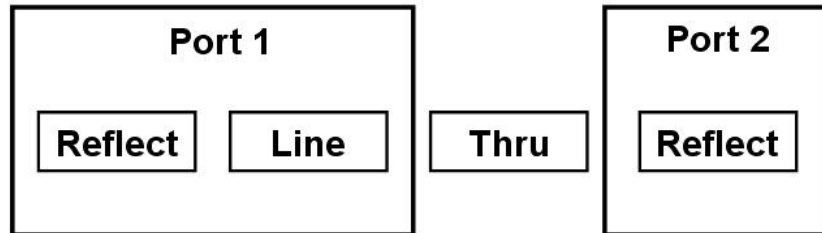


Figure D.2: An illustration of the calibration wizard interface during the calibration process. The *Reflection*, *Line* and *Thru* options are for the short, matched and open measurements required for the calibration.

- For the *reflection* measurement from port 1, the block of metal was placed on the reference plane  $A$  closest to port 1 (i.e. short circuit) and the rest of the experimental setup was kept exactly the same. *reflection* on port 1 was selected on the calibration wizard interface.
- For the *line* measurement from port 1, the block of EM wave

absorber was placed between the two reference planes A and B. The rest of the setup was kept the same and the *line* option on port 1 was selected on the calibration wizard interface.

- The *thru* measurement between ports 1 and 2 was performed by leaving the experimental setup empty without the metal block, the EM absorbers or the PC lattice. The rest of the setup was kept the same and the *thru* option was selected on the calibration wizard interface.
- The *reflection* measurement was also performed for port 2 by placing the block of metal was placed on the reference plane *B*
- The calibration setup was named and saved
- The magnitude of the scattering parameter  $S_{11}$  and  $S_{21}$  are checked to see if they are 0 and 1 respectively for the frequency range of interest.

# Bibliography

- [1] Hull, A. W. The effect of a uniform magnetic field on the motion of electrons between coaxial cylinders. *Physical Review* 18(1), 1921, pp.31–57.
- [2] Hull, A. W. The magnetron. *Journal of the American Institute of Electrical Engineers* 40(9), September 1921, pp.715–723.
- [3] Zhou, W. et al. Low-power phototransceiver arrays with vertically integrated resonant-cavity LEDs. *IEEE Photon. Technol. Lett* 13(11), November 2001, pp.1218–1220.
- [4] Evaldsson, P. A. et al. An optoelectronic resonant cavity technology based on inversion channel devices. *Optical and Quantum Electronics* 24, 1992, pp.133–146.
- [5] Varian, R. H. and Varian, S. F. A High Frequency Oscillator and Amplifier. *J. Appl. Phys.* 10, 1939, pp.321.
- [6] Arsenjewa-Heil, A. and Heil, O. New method of producing short, undamped waves of great intensity (translated title). *Zeitschrift fur Physik*, 95(11-12), Germany, 12 July 1935, pp.752-762.

- [7] Livingston, M. S. and Blewett, J. *Particle Accelerators*. New York: McGraw-Hill, 1962.
- [8] International Atomic Energy Agency. *Particle Accelerators*. Available at: <http://www-naweb.iaea.org/napc/physics/ACTIVITIES/pa.htm> (Accessed: January 22 2007).
- [9] Amaldi, U. The importance of particle accelerators. *Proceedings of EPAC 2000, Vienna, Austria*, Available at: <http://accelconf.web.cern.ch/AccelConf/e00/PAPERS/MOXE01.pdf> (Accessed: January 22 2007).
- [10] Gross, K. D. and Pavlovic, M. eds. Proposal for a Dedicated Ion Beam Facility for Cancer Therapy. *Univ. Heidelberg-DKFZ-GSI, GSI, Darmstadt*, 1998.
- [11] Bryant, P. J. et al, Proton-Ion Medical Machine Study, Part I and II, *CERN/PS 1999-010 (DI) and CERN/PS 2000-007 (DR)*.
- [12] Karceski, J. Accelerator apps: sterilizing medical supplies. *symmetry*, 7(3), June 2010, pp.42. Available at: [www.symmetrymagazine.org/archive/apps](http://www.symmetrymagazine.org/archive/apps)
- [13] Knight, C. and Chui, G. Accelerator apps: Mining. *symmetry*, 7(1), February 2010, pp.42. Available at: [www.symmetrymagazine.org/archive/apps](http://www.symmetrymagazine.org/archive/apps)

- [14] Mason, T.E. et al. The Spallation Neutron Source: A Powerful Tool for Materials Research. *Proceedings of the XXth International Linac Conference (LINAC 2000)*, Monterey, Canada, August, 2000, pp. 1043. arXiv:physics/0007068v1 [physics.acc-ph].
- [15] Hofmann, S. Production and decay of  $^{269}\text{110}$ . *Zeitschrift für Physik A Hadrons and Nuclei*, 350(4), December 1995, pp.277-280.
- [16] Clements, E. Accelerator apps: cargo scanning. *symmetry*, 7(4), August 2010, pp.42. Available at: [www.symmetrymagazine.org/archive/apps](http://www.symmetrymagazine.org/archive/apps)
- [17] Schwarzschild, B. M. ATA: 10-kA Pulses of 50 MeV Electrons, *Physics Today*, February 1982, pp. 20.
- [18] Gsponer, A. and Hurni, J-P. The physics of antimatter induced fusion and thermonuclear explosions. *Proceedings of the th International Conference on Emerging Nuclear Energy Systems, Madrid*, 1986. Also available at: World Scientific, Singapore, 1987, pp. 166169.
- [19] Accelerator-driven Systems (ADS) and Fast Reactors (FR) in Advanced Nuclear Fuel Cycles A Comparative Study. *OECD Nuclear Energy Agency*, 2002. Available on: <http://www.nea.fr/html/ndd/reports/2002/nea3109.html>

- [20] Stacey, W. M. et al. A Subcritical, Gas-Cooled Fast Transmutation Reactor with a Fusion Neutron Source. *Nuclear Technology*, 150(2), May 2005, pages 162188.
- [21] Clements, E. Accelerator applications: shrink wrap. *symmetry*, 6(5), October 2009, pp.32. Available at: [www.symmetrymagazine.org/archive/apps](http://www.symmetrymagazine.org/archive/apps)
- [22] Kuchment, O. Accelerator apps: heat-shrink tubing. *symmetry*, 7(2), April 2010, pp.32. Available at: [www.symmetrymagazine.org/archive/apps](http://www.symmetrymagazine.org/archive/apps)
- [23] Duval, A. in *Pisanello*, Actes du Colloque du Juin, 1996. Cordelier, D. and Py, B. eds. Muse du Louvre, La Documentation Franaise, 1998.
- [24] *Missing Higgs*. CERN, 2011. Available at: <http://public.web.cern.ch/public/en/Science/Higgs-en.html>. Accessed on: 12-09-2011.
- [25] *The Large Hadron Collider*. CERN, 2011. Available at: <http://press.web.cern.ch/public/en/LHC/LHC-en.html>. Accessed on: 12-09-2011.
- [26] Griffiths, D. J. *Introduction to electrodynamics*. 3rd ed. Upper Saddle River, [NJ.]: Prentice-Hall, 1999, pp. 2.
- [27] Nakamura, K. et al. (Particle Data Group), *J. Phys. G.* 37, 075021, (2010)

- [28] Muratori, B. *Luminosity in the presence of offsets and a crossing angle*, AB-Note-2003-026, CERN, 2003.
- [29] Palmer, R. B. *Energy scaling, crab crossing and the pair problem*. Technical Report SLAC-PUB-4707, Stanford, CA, 1988.
- [30] Oide, K. and Yokoya, K. Beam-beam collision scheme for storage-ring colliders. *Phys. Rev. A* 40(1), 1989, pp.315-316.
- [31] Abe, T. et al. *Compensation of the crossing angle with crab cavities at KEKB*. Conf. Proc. PAC-2007, Albuquerque, New Mexico, USA, 2007, pp.27-31.
- [32] Burt, G. *X-band crab cavities for the CLIC beam delivery system*. Proceedings of 44th ICFA Advanced Beam Dynamics Workshop: X-Band RF Structure and Beam Dynamics, Warrington, United Kingdom, December 2008.
- [33] Ambattu, P. K. et al. *Wakefield damping for the CLIC crab cavity*. EuCARD Conference Paper(EuCARD-CON-2009-017), 2009.
- [34] Khan, V. et al. Wakefield Suppression in the CLIC Main Linac. *EPAC-2008, Italy* WEPP089, 2008.
- [35] Jones, R. M. et al. An Investigation of Optimised Frequency Distributions for Damping Wakefields in X-Band Linacs for the NLC. *Technical Report SLAC-PUB-8609, Stanford, CA*, September 2000.

- [36] Smirnova, E. I. et al. Fabrication and cold test of photonic band gap resonators and accelerator structures. *Phys. Rev. ST Accel. Beams* 8(9), 091302, August 2005.
- [37] Di Gennaro, E. et al. Mode confinement in photonic quasicrystal point-defect cavities for particle accelerators. *Appl. Phys. Lett.*, 93(16), 164102, 2008.
- [38] Di Gennaro, E. et al. Hybrid photonic-bandgap accelerating cavities. *New Journal of Physics* 11, 113022, 2009.
- [39] Werner, G. R. Bauer, C. A. and Cary, J. R. Wakefields in photonic crystal cavities. *Phys. Rev. ST Accel. Beams* 12, 071301, 2009.
- [40] Jing, C. et al. Observation of wakefields in a beam-driven photonic band gap accelerating structure. *Phys. Rev. ST Accel. Beams* 12, 121302, 2009.
- [41] Smirnov, A. and Yu, D. Rod-Loaded and PBG Multi-Beam Klystron Cavities. *Proceedings of Particle Accelerator Conference (PAC 05), Knoxville, Tennessee, TPPT050*, May 2005, pp. 3094 - 3096.
- [42] Jang, K. H. et al. High order mode oscillation in a terahertz photonic-band-gap multibeam reflex klystron. *Appl. Phys. Lett.* 93, 211104, 2008.
- [43] Joannopoulos, J. D. et al. *Photonic Crystals: Molding the Flow of Light*. Princeton University Press, Princeton, 2008.

- [44] Streetman, B. G. and Sanjay, B. *Solid State electronic Devices*. 5th ed. New Jersey: Prentice Hall, 2000, p.524.
- [45] Sepkhanov, R. *Light Scattering by Photonic Crystals with a Dirac Spectrum*. PhD Thesis, 2009.
- [46] Zeng, C. et al. Tunneling Spectroscopy of Metal-Oxide-Graphene Structure. *Appl. Phys. Lett.* 97, 032104, 2010.
- [47] Ochiai, T. and Onoda, M. Photonic analog of graphene model and its extension: Dirac cone, symmetry, and edge states. *Phys. Rev. B* 80(15), 155103, 2009.
- [48] Zandbergen, S. R. and de Dood, M. J. A. Experimental Observation of Strong Edge Effects on the Pseudodiffusive Transport of Light in Photonic Graphene. *Phys. Rev. Lett.* 104(4), 043903, 2010.
- [49] Bittner, S. et al. Observation of a Dirac point in microwave experiments with a photonic crystal modeling graphene. *Phys. Rev. B* 82(1), 014301, 2010.
- [50] Decker, F. J. *Transverse effects of longitudinal wakefields at high dispersion*. Technical Report SLAC-PUB-6179, CONF-930511-473, Stanford, CA, 1993.
- [51] Decker, F. J. *Transverse wakefields at high dispersion*. Conf. Proc. EPAC92, Berlin, Germany, 1992, pp.759-761.

- [52] Altenmueller, O.A., Larsen, R.R. and Loew, G.A. *Investigations of travelling-wave separators for the Stanford two-mile linear accelerator* Technical Report SLAC-PUB-017, Stanford Linear Accelerator Center, Stanford, CA, 1963.
- [53] Loew, G.A. and Altenmueller, O.H. *Design and application of RF separator structures at SLAC* Technical Report SLAC-PUB-135, Stanford Linear Accelerator Center, Stanford, CA, 1965.
- [54] Fuerst, J.D. et al. *An RF separated kaon beam from the main injector: superconducting aspects* Technical Report FERMILAB-TM-2060, Fermi National Accelerator Laboratory, 1998.
- [55] Sun, Y. -E. et al. *Design Study of a Transverse to Longitudinal Emittance Exchange Proof of principle Experiment* Conf. Proc. PAC-2007, Albuquerque, New Mexico, USA, 2007, pp.3441-3443.
- [56] Shi, J. et al. A 3-cell deflecting RF cavity for emittance exchange experiment at ANL. *Nucl. Instr. and Meth. A* 598(2), 2009, pp.388-393.
- [57] Cornacchia, M. and Emma, P. Transverse to longitudinal emittance exchange. *Phys.Rev.ST Accel.Beams* 5(8), 084001, 2002.
- [58] Kim, K.J. and Sessler, A. *Transverse-longitudinal phase-space manipulations and correlations*. AIP Conf. Proc. 821, 2006, pp.115-138.

- [59] P.Emma, et al. Transverse-to-longitudinal emittance exchange to improve performance of high-gain free-electron lasers. *Phys.Rev.ST Accel.Beams* 9(10), 100702, 2006.
- [60] Nozawa, S. et al. Developing 100 ps-resolved X-ray structural analysis capabilities on beamline NW14A at the Photon Factory Advanced Ring. *J. Synchrotron Rad.* 14, 2007, pp.313-319.
- [61] Harkay, K. et al. *Generation of Short X-Ray Pulses Using Crab Cavities at the Advanced Photon Source*. Conf. Proc. PAC-2005, Knoxville, Tennessee, USA, 2005, pp.668-670.
- [62] Bentson, L., Emma, P.and Krejcik, P. *A New bunch compressor chicane for the SLAC linac to produce 30 fsec, 30 kA, 30-GeV electron bunches*. EPAC-2002, Paris, France, 2002, pp.683-685.
- [63] Akre, R. et al. *Bunch length measurements using a transverse RF deflecting structure in the SLAC linac*. EPAC-2002, Paris, France, 2002, pp.1882-1884.
- [64] Akre, R. et al. *A Transverse RF deflecting structure for bunch length and phase space diagnostics*. PAC-2001, Chicago, IL, USA, 2001, pp.2353-2355.
- [65] England, R. J. et al. *Commissioning of the UCLA Neptune X-Band Deflecting Cavity and Applications to Current Profile Measurement of Ramped Electron Bunches*. Conf. Proc. PAC-2007, Albuquerque, New Mexico, USA, 2007, pp.4135-4137.

- [66] Seryi, A. et al. *Design of the beam delivery system for the international linear collider*. Conf. Proc. PAC-2007, Albuquerque, New Mexico, USA, 2007, pp.1985-1988.
- [67] Zimmermann, F. *LHC upgrade scenarios*. Conf. Proc. PAC-2007, Albuquerque, New Mexico, USA, 2007, pp.714-718.
- [68] Burt, G. et al. *Crab Cavities for Linear Collider*. Conf. Proc. LINAC08, Victoria, BC, Canada, THP023, 2008, pp.830-832.
- [69] Ambattu, P. K. et al. *Initial study on the shape optimisation of the CLIC crab cavities*. Conf. Proc. LINAC08, Victoria, BC, Canada, 2008, pp.833-835.
- [70] Floquet, G. Sur les quations differentielles linaires coefficients priodiques. *Ann. cole Norm. Sup.* 12, 1883, pp.47-88.
- [71] Bloch, F. ber die Quantenmechanik der Elektronen in Kristallgittern. *Z. Physik* 52, 1928, pp.555-600.
- [72] Smirnova, E. I. et al. Simulation of Photonic Band Gaps in Metal Rod Lattices for Microwave Applications. *Appl. Phys.* 91(3), 2002, pp.960-968.
- [73] Smirnova, E. I. et al. Demonstration of a 17-GHz, High-Gradient Accelerator with a Photonic-Band-Gap Structure. *Phys. Rev. Lett.* 95(7), 074801, 2005.

- [74] Lord Rayleigh. On the Influence of Obstacles arranged in Rectangular Order upon the Properties of a Medium. *Phil. Mag.* 34, 1892, p.481.
- [75] Yablonovitch, E. Inhibited Spontaneous Emission in Solid-State Physics and Electronics. *Phys. Rev. Lett.* 58(20), 1987, pp.2059-2062.
- [76] John, S. Strong Localization of Photons in Certain Disordered Dielectric Superlattices. *Phys. Rev. Lett.* 58(23), 1987, pp.2486-2489.
- [77] Inoue, K. (Kuon) and Ohtaka, K. (Kazuo) *Photonic Crystals: Physics, Fabrication, and Applications*. Springer, 2004.
- [78] Anderson, C. M. and Giapis, K. P. Larger Two-Dimensional Photonic Band Gaps. *Phys. Rev. Lett.* 77(14), 1996, pp.2949-2952.
- [79] T. Ito and Sakoda, K. Photonic bands of metallic systems. II. Features of surface plasmon polaritons. *Phys. Rev. B* 64(4), 045117, 2001.
- [80] Chang, Chien C. et al. Effect of the inclusion of small metallic components in a two-dimensional dielectric photonic crystal with large full band gap. *Phys. Rev. B* 70(7), 075108, 2004.
- [81] Smith, D. R. et al. Experimental and theoretical results for a two-dimensional metal photonic band-gap cavity. *Appl. Phys. Lett.* 65(5),1994.

- [82] Nicorovici, N. A., McPhedran, R. C. and Botten, L. C. Photonic Band Gaps for Arrays of Perfectly Conducting Cylinders. *Phys. Rev. E* 52, 1995, pp.1135-1145.
- [83] Diana, R. et al. A Model to Optimize a Microwave PBG Accelerator Based on Generic Unit Cell2. *J. European Optical Society - Rapid Publications* 2, 07006, 2007.
- [84] Matthews, A. et al. Band-gap properties of two-dimensional low-index photonic crystals. *Appl. Phys. B* 81 , 2005, pp.189-193.
- [85] Sigalas, M. M. et al. Metallic photonic band-gap materials. *Phys. Rev. B* 52(16), 1995, pp.11744-11751.
- [86] De Lustrac, A. et al. Experimental demonstration of electrically controllable photonic crystals at centimeter wavelengths. *Appl. Phys. Lett.* 75(11), 1999, p.1625.
- [87] Suzuki, T. and Yu, P.K.L. Method of projection operators for photonic band structures with perfectly conducting elements. *Phys. Rev. B* 57, 1998, pp.2229-2241.
- [88] Pendry, J. B. Calculating Photonic Band-Structure. *J. Phys. Cond. Mat.* 8, 1996, p.1085.
- [89] Qiu, M. and He, S. A nonorthogonal FDTD method for computing the band structure of a two-dimensional photonic crystal with dielectric and metallic inclusions. *J. Appl. Phys.* 87(12), 2000, pp.8268.

- [90] Taflove, A. and Hagness, S. C. *Computational Electrodynamics: The Finite-Difference Time-Domain Method* 3rd ed. Norwood, MA: Artech House, 2005.
- [91] Pelosi, G., Coccioli, R. and Selleri, S. (Eds.), *Quick Finite Elements for Electromagnetic Waves* Artech House.
- [92] Wallace, P. R. Erratum: The Band Theory of Graphite. *Phys. Rev.* 71, 1947, p.622.
- [93] McClure, J. W. Diamagnetism of Graphite. *Phys. Rev.* 104(3), 1956, pp.666-671.
- [94] Semenoff, G. W. Condensed-Matter Simulation of a Three-Dimensional Anomaly. *Phys. Rev. Lett.* 53(26), 1984, pp.2449-2452.
- [95] DiVincenzo, D. P. and Mele, E. J. Self-consistent effective-mass theory for intralayer screening in graphite intercalation compounds. *Phys. Rev. B* 29(4), 1984, pp.1685-1694.
- [96] Haldane, F. D. M. Quantum Hall effect without Landau levels: a condensed-matter realization of the parity anomaly. *Phys. Rev. Lett.* 61, 1988, pp.2015-2018.
- [97] Neto, A. H. Castro et al. The electronic properties of graphene. *Rev. Mod. Phys.* 81(1), 2009, pp.109-162.
- [98] Novoselov, K. S. et al. Electric Field Effect in Atomically Thin Carbon Films. *Science* 306(5696), 2004, pp.666-669.

- [99] Meyer, J. C. et al. The structure of suspended graphene sheets. *Nature* 446, 2007, pp.60-63.
- [100] Peierls, R. E. Bemerkung ueber Umwandlungstemperaturen. *Helv. Phys. Acta* 7, 1934, pp.81-83.
- [101] Peierls, R. E. Quelques propriets typiques des corps solides. *Ann. Inst. Henri Poincare* 5, 1935, pp.177-222.
- [102] Landau, L. D. Zur Theorie der Phasenumwandlungen II. *Phys. Z. Sowjetunion* 11, 1937, pp.26-35.
- [103] Landau, L. D. and Lifshitz, E. M. *Statistical Physics Part I* Sections 137 and 138. Oxford: Pergamon, 1980.
- [104] Mermin, N. D. and Wagner, H. Absence of Ferromagnetism or Antiferromagnetism in One- or Two-Dimensional Isotropic Heisenberg Models. *Phys. Rev. Lett.* 17, 1966, pp.1133-1136.
- [105] Hohenberg, P. C. Existence of Long-Range Order in One and Two Dimensions. *Phys. Rev.* 158(2), 1967, pp.383-386.
- [106] Mermin, N. D. Crystalline Order in Two Dimensions. *Phys. Rev.* 176(1), 1968, pp.250-254.
- [107] Novoselov, K. S. et al. Two-dimensional gas of massless Dirac fermions in graphene. *Nature* London 438, 2005, pp.197-200.
- [108] Novoselov, K. S. et al. Unconventional Quantum Hall Effect and Berrys Phase of  $2p$  in Bilayer Graphene. *Nat. Phys.* 2, 2006, pp.177-180.

- [109] Zhang, Y. et al. Hall effect and Berry's phase in graphene. *Nature* London 438(7065), 2005, p.201.
- [110] Novoselov, K. S. et al. Room-Temperature Quantum Hall Effect in Graphene. *Science* 315(5817), 2007, p.1379.
- [111] Ludwig, A. W. W. et al. Integer quantum Hall transition: An alternative approach and exact results. *Phys. Rev. B* 50(11), 1994, pp.7526-7552.
- [112] Ryu, S. et al. Landauer conductance and twisted boundary conditions for Dirac fermions. *Phys. Rev. B* 75, 205344, 2007.
- [113] Shon, N. H. and T. Ando, J. Quantum Transport in Two-Dimensional Graphite System. *Phys. Soc. Jpn.* 67(7), 1998, p.2421.
- [114] Peres, N. M. R., Castro Neto, A. H. and Guinea, F. Dirac fermion confinement in graphene. *Phys. Rev. B* 73(24), 2006.
- [115] Tworzydło, J. et al. Sub-Poissonian Shot Noise in Graphene. *Phys. Rev. Lett.* 96, 246802, 2006.
- [116] McCann, E. et al. Weak-Localization Magnetoresistance and Valley Symmetry in Graphene. *Phys. Rev. Lett.* 97, 146805, 2006.
- [117] Kechedzhi, K. et al. Influence of trigonal warping on interference effects in bilayer graphene. *Phys. Rev. Lett.* 98, 176806, 2007.

- [118] Katsnelson, M. I., Novoselov, K. S. and Geim, A. K. Chiral tunnelling and the Klein paradox in graphene. *Nature Phys.* 2, 2006, pp.620-625.
- [119] B. Fauser, J. Tolksdorf, and Zeidler, E. *Quantum Gravity*. Basel: Birkhuser, 2007.
- [120] Akhmerov, A. R. and Beenakker, C. W. J. Boundary conditions for Dirac fermions on a terminated honeycomb lattice. *Phys. Rev. B* 77(8), 085423, 2008.
- [121] Schomerus, H. Effective contact model for transport through weakly-doped graphene. *Phys. Rev. B* 76(4), 045433, 2007.
- [122] Nair, R. R. et al. Fine Structure Constant Defines Visual Transparency of Graphene. *Science* 320(5881), 2008, p.1308.
- [123] Patchkovskii, S. et al. Graphene nanostructures as tunable storage media for molecular hydrogen. *Proc. Natl. Acad. Sci.* 102(30), 2005, pp.10439-10444.
- [124] Cheianov, V. V. and Falko, V. I. Selective transmission of Dirac electrons and ballistic magnetoresistance of n-p junctions in graphene. *Phys. Rev. B* 74, 041403, 2006.
- [125] Cheianov, V. V., Falko, V. and Altshuler, B. L. The Focusing of Electron Flow and a Veselago Lens in Graphene p-n Junctions. *Science* 315(5816), 2007, pp.1252-1255.

- [126] Fogler, M. M. et al. Effect of disorder on a graphene p-n junction. *Phys. Rev. B* 77(7), 075420, 2008.
- [127] *BandSolve photonics software from RSoft Design Group, Ossining, NY.* Available at: [www.rsoftdesign.com](http://www.rsoftdesign.com)
- [128] Taflove, A. and Brodwin, M. E. Numerical solution of steady-state electromagnetic scattering problems using the time-dependent Maxwells equations. *IEEE Trans. Microwave Theory Tech.* 23(8), 1975, pp.623-630.
- [129] Jian, Jianming *The Finite Element Method in Electromagnetism.* Wiley-IEEE Press, 2002.
- [130] MATLAB: The Language of Technical Computing. *The MathWorks Inc, Natick, MA, USA.*, Version 7.1, September 2005, pp.1-38. Available at: <http://www.serc.iisc.ernet.in/ComputingFacilities/software/math.pdf>, (Accessed: 3 Febuary 2011).
- [131] Horn, R. A. and Johnson, C. A. *Matrix Analysis.* Cambridge University Press, 1985, pp.176180.
- [132] Sakoda, K. et al. Photonic bands of metallic systems. I. Principle of calculation and accuracy. *Phys. Rev. B* 64, 045116, 2001.
- [133] Morton, K.W. and Mayers, D.F. *Numerical Solution of Partial Differential Equations, An Introduction.* Cambridge University Press, 2005.

- [134] K. Yee, Numerical solution of initial boundary value problems involving Maxwell's equations in isotropic media. *IEEE Transactions on Antennas and Propagation* 14(3), 1966, pp.302-307.
- [135] Farjadpour, A. et al. Improving accuracy by subpixel smoothing in the finite-difference time domain. *Opt. Lett.* 31(20), 2006, pp.2972-2974.
- [136] *Meep manual*. Available at: [http://ab-initio.mit.edu/wiki/index.php/Meep\\_manual](http://ab-initio.mit.edu/wiki/index.php/Meep_manual) (Accessed: 4 June 2008).
- [137] Berenger, J. P. A perfectly matched layer for the absorption of electromagnetic waves. *J. Comput. Phys.* 114(2), 1994, pp.185-200.
- [138] Sacks, Z. S. et al. A perfectly matched anisotropic absorber for use as an absorbing boundary condition. *IEEE Trans. Antennas and Propagation* 43(12), 1995, pp.1460-1463.
- [139] *Harminv*. Available at: <http://ab-initio.mit.edu/wiki/index.php/Harminv> (Accessed: 4 June 2008).
- [140] Mandelshtam, V. A. and Taylor, H. S. Harmonic inversion of time signals. *J. Chem. Phys.* 107 (17), 1997, pp.6756-6769.
- [141] Coccioli, R. et al. Finite Element Methods in Microwaves: A Selected Bibliography. *IEEE Antennas Propag. Mag.* 38(6), 1996, pp.34-48.

- [142] Ferrari, L. R. The Finite-Element Method, Part 2: P. P. Silvester, an Innovator in Electromagnetic Numerical Modeling. *IEEE Antennas Propag. Mag.* 49(3), 2007, pp.216-234.
- [143] Reddy, C. J. et al. Finite Element Method for Eigenvalue Problems in Electromagnetics *NASA Technical Paper* 3485, 1994.
- [144] Silvester, P. P. and Ferrari, R. L. *Finite Elements for Electrical Engineers*. 2nd ed. Cambridge Univ. Press, 1990.
- [145] Bossavit, Alain. Simplicial Finite Elements for Scattering Problems in Electromagnetism. *Comput. Methods Appl. Mech. and Eng.* 76, 1989, pp.299-316.
- [146] Lee, J.-F., Sun, D. K., and Cendes, Z. J. Full-Wave Analysis of Dielectric Waveguides Using Tangential Vector Finite Elements. *IEEE Trans. Microw. Theory. and Techni.* 39(8), 1991, pp.1262-1271.
- [147] Silvester, P. Construction of Triangular Finite Element Universal Matrices. *Int. J. Numer. Methods Eng.* 12(2), 1978, pp.237-244.
- [148] Rahman, B. M. A. and Davies, J. B. Penalty Function Improvement of Waveguide Solution by Finite Elements. *IEEE Trans. Microw. Theory and Techni.* 32(8), 1984, pp.922-928.
- [149] Koshiba, Masanori, Hayata, Kazuya and Suzuki, Michio Improved Finite-Element Formulation in Terms of the Magnetic

- Field Vector for Dielectric Waveguides. *IEEE Trans. Microw. Theory and Techni.* 33(3), 1985, pp.227-233.
- [150] Zimmerman, W. B. J. *Multiphysics Modeling With Finite Element Methods* World Scientific, 2006.
- [151] Harlow, F. H., "A Machine Calculation Method for Hydrodynamic Problems," Los Alamos Scientific Laboratory report LAMS-1956 (November 1955).
- [152] Dawson, J. M. *Rev. Mod. Phys.* , 55(2), April 1983.
- [153] Birdsall, C. K. and Langdon, A. B. *Plasma Physics Via Computer Simulation*, McGraw-Hill, 1985.
- [154] Hockney, R. W. and Eastwood, J. W. *Computer Simulation Using Particles*, IOP Publishing Ltd 1988.
- [155] Nieter, C. and Cary, J. R. VORPAL: a versatile plasma simulation code. *Journal of Computational Physics* 196(2), 2004, pp.448-473.
- [156] Harrington, R. F. *Time-Harmonic Electromagnetic Fields* McGraw-Hill Electrical And Electronic Engineering Series, Wiley-IEEE Press, 1961.
- [157] Matthews, C. J. and Seviour, R. *J. Appl. Phys.B* 94, 2009, pp.381-388.

- [158] Radisic, V., Qian, Y. and Itoh, T. Broad-band power amplifier using dielectric photonic bandgap structure. *IEEE Microwave Guided Wave Lett.* 8(1), 1998, pp.13-14.
- [159] Horii, Y. and Tsutsumi, M. Harmonic control by photonic bandgap on microstrip patch antenna. *IEEE Microwave Guided Wave Lett.* 9(1), 1999, pp.13-15.
- [160] Sor, J., Qian, Y. and Itoh, T. Miniature Low-Loss CPW Periodic Structures for Filter Applications. *IEEE Trans. Microwave Theory Tech.* 49, 2001, pp.2336-2341.
- [161] Bane, K. and Seryi, A. *Wakefield Effects in the Beam Delivery System of the ILC*. Conf. Proc. of PAC-2007, Albuquerque, New Mexico, USA, 2007, pp.3088-3090.
- [162] Burt, G. et al. *Progress towards crab cavity solutions for the ILC*. FERMILAB-CONF-06-541, EUROTEV-REPORT-2006-058, COCKCROFT-06-31, 2006.
- [163] Vuckovic, J. et al. Design of photonic crystal microcavities for cavity QED. *Phys. Rev. E* 65, 016608-1, 2001.
- [164] Park, H. G. et al. Characteristics of modified single-defect two-dimensional photonic crystal lasers. *IEEE J. Quantum Electron.* 38, 2002, pp.1353-1365.
- [165] Zheng, W. H. et al. Dipole mode photonic crystal point defect laser on InGaAsP/InP. *Journal of Crystal Growth* 292(2), 2006, pp.341-344.

- [166] Kalra, Y. and Sinha, R. K. Photonic band gap engineering in 2D photonic crystals. *Pramana - J. Phys.* 67(6), 2006, pp.1155-1164.
- [167] Yablonovitch, E. et al. Donor and acceptor modes in photonic band structure. *Phys. Rev. Lett.* 67(24), 1991, pp.3380-3383.
- [168] Gomez Rivas, J. et al. et al. Experimental determination of the effective refractive index in strongly scattering media. *Opt. Commun.* 220, 2003, pp.17-21.
- [169] Lin, S. Y. et al. Direct measurement of the quality factor in a two-dimensional photonic-crystal microcavity. *Opt. Lett.* 26(23), 2001, pp.1903-1905.
- [170] Panofsky, W.K.H. and Wenzel, W.A. Some considerations concerning the transverse deflection of charged particles in radio-frequency fields *Rev. Sci. Instrum.* 27(11), 1956, p.967.
- [171] Browman, M.J. (Los Alamos) *Using the Panofsky-Wenzel theorem in the analysis of radio-frequency deflectors.* Conf. Proc. IEEE Particle Accelerator Conference (PAC93), Washington, DC, 1993, pp.800-802.
- [172] Fedotov, A. V. Gluckstern, R. L. and Venturini, M. *High frequency behavior of transverse impedance for a cavity in a beam pipe.* Conf. Proc. IEEE Particle Accelerator Conference (PAC99), New York, 1999.

- [173] Bane, K. *Short-range dipole wakefields in accelerating structures for the NLC*. SLAC-PUB-9663, LCC-0116, March, 2007.
- [174] Bane, K. L. F. Mosnier, A. Novokhatsky, A. and Yokoya, K. *Proceedings of the 1998 International Computational Accelerator Physics Conference (ICAP98), Monterey, CA* (Stanford Linear Accelerator Center, Menlo Park, CA, 1998).
- [175] Yokoya, K. KEK-Report 90-21, KEK (1990).
- [176] Yokoya, K. *Short range wake formulas for infinite periodic pill-box*. 1998. unpublished.
- [177] Gluckstern, R. L. *Physical Review D* 39, 2780, 1989.
- [178] Yokoya, K. and Bane, K. *Conf. Proc. IEEE Particle Accelerator Conference (PAC99), New York, 1999*. (Piscataway, NJ, 1999), p. 1725.
- [179] Carter, R. G. *Electromagnetic waves : microwave components and devices*. R.G. Carter. 1st ed. London ; New York : Chapman and Hall, 1990.
- [180] Marsh, R. A. X-band photonic band-gap accelerator structure breakdown experiment. *Phys. Rev. ST Accel. Beams* 14, 021301, 2011.
- [181] Dimitrov, D. V. et al. Dielectric breakdown of MgO magnetic tunnel junctions. *Appl. Phys. Lett.* 94(12), 123110, 2009.

- [182] Auerkari, P. *Mechanical and physical properties of Engineering Alumina ceramics*, Technical Research Centre of Finland, VTT Tiedotteita-Meddelanden-Research Notes 1792, Espoo, 1996.
- [183] Dolgashev, V. A. et al. *High Power Tests of Normal Conducting Single Cell Structures*, SLAC-PUB-12956, PAC07, Albuquerque, New Mexico, 25-29 June 2007, pp. 2430-2432.
- [184] Pritzkau, D. P. *RF pulsed heating*. SLAC-R-577, 2001.
- [185] Koseki, T. *Reduced length designs of 500 MHz damped cavity using SiC microwave absorber*. Proceedings of EPAC04, Lucerne, Switzerland, 2004.
- [186] Wilson, P. B. Stanford Linear Accelerator Center Report No. *SLAC-PUB-7449*, 1997, (unpublished).
- [187] Pritzkau, D. P. Siemann, R. H. *Experimental study of rf pulsed heating on oxygen free electronic copper*. Phys. Rev. ST Accel. Beams 5, 112002, 2002.
- [188] Ginzburg, N. S. et al *Experiment on pulse heating and surface degradation of a copper cavity powered by powerful 30 GHz free electron maser*. Phys. Rev. ST Accel. Beams 14, 041002, 2011.
- [189] Li, Z. et.al. Stanford Linear Accelerator Center Report No. *SLAC-PUB-8647*, 2000, (unpublished).
- [190] Liu, J. F. *RF surface resistance of copper-on-beryllium at cryogenic temperatures measured by a 22GHz demountable cavity*.

Proceedings of PAC2003, Portland, Oregon, LA-UR-03-3153,  
May, 2003.

- [191] Prestona, S. D. Brethertona, I. Forty, C. B. A. *The thermo-physical and mechanical properties of the copper heat sink material intended for use in ITER*. Fusion Engineering and Design, Volumes 66-68, September 2003, Pages 441-446.
- [192] Braginsky, V. B. Ilchenko, V. S. and Bagdassarov, K. S. *Experimental observation of fundamental microwave absorption in high-quality dielectric crystals*. Phys. Lett. A, vol. 120, 1987, p. 300.
- [193] Kosaka, H. et al. Superprism phenomena in photonic crystals. *Phys. Rev. B* 58(16), 1998, pp.10096-10099.
- [194] Notomi, M. Theory of light propagation in strongly modulated photonic crystals: Refraction like behaviour in the vicinity of the photonic band gap. *Phys. Rev. B* 62, 2000, pp 10696-10705.
- [195] Luo, C. et al. All-angle negative refraction without negative effective index. *Phys. Rev. B* 65, 2002, pp.201104-201108.
- [196] Zhang, X. Tunable non-near-field focus and imaging of an unpolarized electromagnetic wave. *Phys. Rev. B* 71(23), 2005, p.235103.
- [197] Chabanov, A. A., Stoytchev, M. and Genack, A. Z. Statistical signatures of photon localization. *Nature (London)* 404, 2000, pp.850-853.

- [198] Laurent, D. et al. Localized Modes in a Finite-Size Open Disordered Microwave Cavity. *Phys. Rev. Lett.* 99(25), 2007, p.253902.
- [199] Zhang, X. *New transport regime and Zitterbewegung effect in two-dimensional photonic crystal.* Conf. Proc. META08, 2008, pp.29-32.
- [200] Kuhl, U. and Stckmann, H. J. Microwave realization of the Hofstadter butterfly. *Phys. Rev. Lett.* 80(15), 1998, pp.3232-3235.
- [201] Raghu, S. and Haldane, F. D. M. Analogs of quantum Hall effect edge states in photonic crystals. *Condensed Matter.* arXiv:cond-mat/0602501v3, 2006.
- [202] Soukoulis, C. M. *Photonic Band Gaps and Localization (NATO ASI Series B: Physics)* Vol. 308, Ed. New York: Plenum Press, 1993.
- [203] Lourtioz, J. M. et al. *Photonic Crystals Towards Nanoscale Photonic Devices* 2nd ed. Berlin: Springer-Verlag, 2008.
- [204] R. A. Sepkhanov, Nilsson, J. and Beenakker, C. W. J. *Phys. Rev. B* 78(4), 045122, 2008.
- [205] Castro Neto, A. H. et al. The electronic properties of graphene. *Rev. Mod. Phys.* 81(1),2009, pp.109-162.

- [206] Sepkhanov, R. A., Bazaliy, Y. B. and Beenakker, C. W. J. Extremal transmission at the Dirac point of a photonic band structure. *Physical Review A* 75(6), 063813, 2007.
- [207] Kim, E. A. and Neto, A. H. Castro Graphene as an electronic membrane. *Europhysics Letters* 84(5), 57007, 2008.
- [208] Haldane, F. D. M. and Raghu, S. Possible Realization of Directional Optical Waveguides in Photonic Crystals with Broken Time-Reversal Symmetry. *Phys. Rev. Lett.* 100(1), 013904, 2008.
- [209] Plihal, M. and Maradudin, A. A. Photonic band structure of two-dimensional systems: The triangular lattice. *Phys. Phys. Rev. B* 44(16), 1991, pp.8565-8571.
- [210] Van Houten, H. and Beenakker, C. W. J. Quantum Point Contacts and Coherent Electron Focusing in van Haeringen, W. and Lenstra, D. eds. *Analogies in Optics and Micro Electronics* Kluwer: Springer, 1990.
- [211] Samokhvalova, K., Chen, C. and Qian, B. Analytical and numerical calculations of the dispersion characteristics of two-dimensional dielectric photonic band gap structures. *J. Appl. Phys.* 99, 063104, 2006.
- [212] Chen, X. Robust method to retrieve the constitutive effective parameters of metamaterials. *Phys. Rev. E* 70, 016608, 2004.

- [213] Nicolson, A. M. and Ross, G. F. Measurement of the Intrinsic Properties of Materials by Time-Domain Techniques. *IEEE Trans. Instrum. Meas.* IM-19(4), 1970, pp. 377-382.
- [214] Smith, D. R. et. al. *Phys. Rev. B* 65, 195104, 2002.
- [215] Markos, P. and Soukoulis, C. M. *Opt. Express* 11, 649, 2003.
- [216] Janezic, M. D. and Jargon, J. A. *Complex Permittivity Determination from Propagation Constant Measurement*. IEEE MICROWAVE AND GUIDED WAVE LETTERS, 9(2), 1999.
- [217] Palumbo, L. Vaccaro, V. G. and Zobov, M. in Proceedings of the CERN Accelerator School: Advanced Accelerator Physics Course, Rhodes, 1993, edited by S. Turner (CERN Yellow Report No. 95-06) (European Laboratory for Particle Physics, Geneva, Switzerland, 1995), pp. 331390.
- [218] Chao, A. W. *Physics of Collective Beam Instabilities in High Energy Accelerators* (Wiley-Interscience, New York, 1993).
- [219] Wilson, P. B. Introduction to wakefields and wake potentials *SLAC PUB 4547* 1989.
- [220] Wilson, P. B. High energy electron linac: Application to storage ring RF system and linear colliders. *SLAC PUB 2884* 1982.
- [221] Chao, A. W. Coherent instabilities of a relativistic bunched beam. *SLAC PUB-2946* 1982.

[222] Bane, K. Weiland, T. Wilson P. Wakefields and wakefield acceleration. *SLAC PUB 3528* 1984.